Fall 2014

Prediction Of The Stress At The Inlet Of The Nip Region In A Roll Compactor

Timothy Patterson
Purdue University

Graduate School Form 30
(Revised 08/14)

PURDUE UNIVERSITY
GRADUATE SCHOOL
Thesis/Dissertation Acceptance

This is to certify that the thesis/dissertation prepared

By Timothy Patterson

Entitled

PREDICTION OF THE STRESS AT THE INLET OF TEH NIP REGION IN A ROLL COMPACTOR

For the degree of Master of Science in Mechanical Engineering

Is approved by the final examining committee:

Carl Wassgren

James Litster

Klein Ileleji

To the best of my knowledge and as understood by the student in the Thesis/Dissertation Agreement, Publication Delay, and Certification/Disclaimer (Graduate School Form 32), this thesis/dissertation adheres to the provisions of Purdue University's "Policy on Integrity in Research" and the use of copyrighted material.

Carl Wassgren

Approved by Major Professor(s): _____

_____

Approved by: Ganesh Subbarayan 10/08/2014

Head of the Department Graduate Program Date

PREDICTION OF THE STRESS AT THE INLET OF THE NIP REGION IN A ROLL COMPACTOR

A Thesis

Submitted to the Faculty

of

Purdue University

by

Timothy J. Patterson

In Partial Fulfillment of the

Requirements for the Degree

of

Master of Science in Mechanical Engineering

December 2014

Purdue University

West Lafayette, Indiana

For my family.

ACKNOWLEDGEMENTS

I would like to thank those who have helped me along my journey in completion of this thesis. First, I would like to thank Prof. Carl Wassgren, who gave me guidance and support in my growth as a researcher. Special thanks to Prof. James Litster and Prof. Klein Ileleji for their service on my examination committee. Thank you to the ERC – CSOPS, and those mentors and members of project B4. In addition, I would like to thank my fellow graduate students and Dr. Muliadi for their feedback, discussions, and expertise which helped me grow as a researcher. Specifically, to Shrikant Swaminathan and the AFL for their help and manufacturing of several parts needed for the experimental setup.

I also want to thank my family and friends for always making me laugh. Thank you to my parents for their support. I thank my dad for teaching me I can. I thank my mom for her laugh. I especially want to thank Ashley for putting up with the distance, always making the most of what time we have together, and letting me know dreams come true.

TABLE OF CONTENTS

Page

Page

LIST OF TABLES

LIST OF FIGURES

Figure Page

Figure Page

Figure Page

Figure Page

Figure Page

Figure Page

Appendix Figure

NOMENCLATURE

A	screw channel cross-sectional area
D	diameter
$\overline{D}$	average feeder diameter
D_b	feeder barrel diameter
D_{sc}	screw core diameter
F_p	force acting perpendicular to the screw flights
F_{ll}	force acting parallel to the screw flights
F_b	frictional force on a solid plug due to the barrel
F_{sc}	frictional force on a solid plug due to the screw core
F_{lf_μ}	frictional force on a solid plug due to the leading screw flight
F_{tf_μ}	frictional force on a solid plug due to the trailing screw flight
F_{ds}	force on a solid plug due to the downstream material
F_{us}	force on a solid plug due to the up-stream material
F_{lf}	normal force on a solid plug due to the leading screw flight
F_{tf}	normal force on a solid plug due to the trailing screw flight
F^*	unknown conveying force at the leading screw flight

e screw flight thickness perpendicular to the screw flight

H screw channel height (distance from the screw core to the screw flight tip)

k ratio of principal stresses (stress ratio)

k_r stress ratio which relates the stresses at the screw core and barrel surfaces to the down channel stress in a feed screw

k_t stress ratio which relates the stresses at the screw flights to the down channel stress in a feed screw

L axial distance along feeder from the inlet

Lp screw pitch length

$\frac{L_P}{1000}$ step size

L_f total feeder length

$\dot{M}$ mass flow rate

p number of screw flights

R radius

R_{sc} screw core radius

R_b feeder barrel radius

T feeder torque due to one screw channel

T_{total} total feeder torque

V_a axial velocity of the material in a feed screw

V_b barrel velocity

V_{bm} velocity of the barrel relative to the material

V_s screw velocity

V_z down channel velocity of the material in a feed screw

W screw channel width perpendicular to the screw flights

$\bar{W}$ average screw channel width perpendicular to the screw flights

W_b screw channel width perpendicular to the screw flights at the barrel surface

W_{sc} screw channel width perpendicular to the screw flights at the screw core surface

dZ down channel length of a material element

$\overline{dZ}$ average down channel length of a material element

dZ_b down channel length of a material element at the barrel surface

dZ_{sc} down channel length of a material element at the screw core surface

$\frac{dL}{Sin(\bar{\emptyset})}$ average down channel length of a material element in terms of the axial distance

$\frac{dL}{Sin(\emptyset_b)}$ down channel length of a material element at the barrel surface in terms of the axial distance

$\frac{dL}{Sin(\emptyset_{sc})}$ down channel length of a material element at the screw core surface in terms of the axial distance

μ_b powder-barrel friction coefficient

μ_s powder-screw friction coefficient

$\emptyset$ screw flight helical angle

$\bar{\emptyset}$ average screw flight helical angle

$\emptyset_b$ screw flight helical angle at the barrel surface

$\emptyset_{sc}$ screw flight helical angle at the screw core

α conveying angle of the material in a feed screw

ρ	density
ρ_{pb}	material poured bulk density
σ	feeder stress
σ_f	feeder outlet stress
σ_i	feeder stress at the i^{th} leading screw flight
σ_r	stress acting at the barrel and screw core surfaces
σ_t	stress acting at the leading and trailing screw flights
σ_0	feeder inlet stress
σ_1	major principal stress
σ_2	minor principal stress

ABSTRACT

Patterson, Timothy J. M.S.M.E., Purdue University, December 2014. Prediction of the Stress at the Inlet of the Nip Region in a Roll Compactor. Major Professor: Carl Wassgren, School of Mechanical Engineering.

The stress at the inlet nip region of a roll compactor (i.e., feeder outlet stress) is a necessary input parameter for existing powder roll compaction models; however the nip region inlet stress is poorly understood and difficult to directly measure. The inability to specify the nip region inlet stress on a roll compactor limits comparisons between powder roll compaction models and experimental results. Therefore, this thesis investigates the application of a solid plug model to a powder feed screw of a roll compactor in order to predict the stress at the inlet nip region.

The feeder outlet stress predictions of the Solid Plug models developed by Tadmor et al. (1972), Campbell et al. (1995), and Hyun et al. (1997a) were compared to experimental results. Each of the Solid Plug models under-predicted the experimentally measured feeder outlet stress by orders of magnitude. Potential reasons why the Solid Plug models poorly predicted the experimental results are the accuracy of the friction coefficient measurements and the assumed values for the stress ratios. The friction coefficients could not be completely defined because the surface finish of the feed screw and barrel were unknown, and the stress ratios were assumed to equal one based on the kinetic theory of granular material (Lun, 1991).

The sensitivity of the Solid Plug models to the following input parameters: friction coefficients, stress ratio, and stress-density relationship are investigated. Adjusting the friction coefficients or stress ratios, such that the stress-density relationship predicts a density greater than the lower density limit, is shown to cause the Solid Plug models' feeder outlet stress predictions to rapidly increase and become more sensitive to the mass flow rate. In most cases, varying the friction coefficients or stress ratios by 10% caused the feeder outlet stress predictions to vary by a factor from two to ten.

The Solid Plug models' poor predictions of the experimental results are also likely due to assuming constant material parameters such as the friction coefficients and stress ratios. The sensitivity of the Solid Plug models to the material input parameters and the effects of the stress-density relationship show that small changes in the material parameters due to the variation in stress along the length of the feed screw could have a significant impact on the Solid Plug models' feeder outlet stress predictions.

The friction coefficients and stress ratios necessary for the Solid Plug models to accurately predict the experimental results were determined. The fitted parameters varied significantly from the initial values input because the initial feeder outlet stress predictions were orders of magnitude below the experimental results. Due to the sensitivity of the Solid Plug models to several input parameters and the poor comparisons between the Solid Plug models' feeder outlet stress predictions and experimental results, the Solid Plug models, as presented in the literature, do not lend themselves to predicting the nip region inlet stress applied to the powder roll compaction models.

In addition to applying the Solid Plug models to a powder feed screw, the Solid Plug models' derivations were extended to determine a relationship between the feeder

torque and the feeder outlet stress. The derivations predict qualitatively the linear relationship between the feeder torque and feeder outlet stress observed experimentally, but quantitative predictions are orders of magnitude different. Although the Solid Plug models' predictions of feeder outlet stress are not applicable to powder roll compaction models, experimentally measuring the feeder torque-outlet stress relationship and measuring the feeder torque on a roll compactor would allow for the feeder outlet stress to be predicted. Determination of the feeder outlet stress allows for real time processing and complete comparisons between the powder roll compaction models and experimental results.

CHAPTER 1. INTRODUCTION

Powder roll compaction is a dry granulation process applied in the pharmaceutical industry to manufacture solid dosage form drugs. Dry granulation helps improve flowability, produce uniform blends, control dusting, and increase material bulk density. The dry granulation process usually begins with material being conveyed, by a feed screw, between two counter rotating rolls producing a densified strip or ribbon of material (Figure 1.1). This step of the dry granulation process encompasses the roll compaction portion. The ribbon is then milled into granules, and lastly these granules are compacted into a tablet.

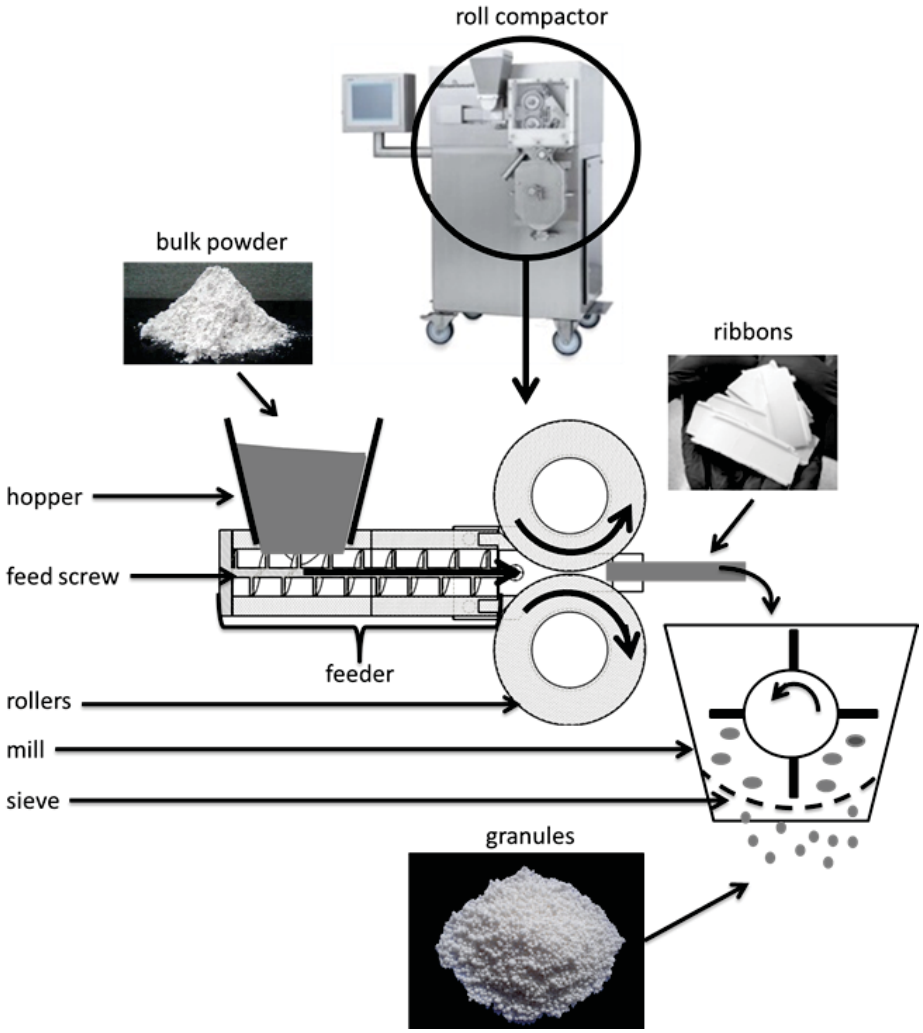

Figure 1.1. Schematic of the roller compaction process used in the pharmaceutical industry.

The granule characteristics, and consequently tablet compaction properties, are largely set by the upstream roll compaction parameters. For this reason, in order to improve the dry granulation process, predictions of roll compaction parameters have been the focus of 1-D analytical (Johanson, 1965; and Katashinskii, 1983a) and higher order finite element method (FEM) (Dec et al., 2003; Zavaliangos et al., 2003; Cunningham, 2005; Michrafy et al., 2011; Muliadi et al., 2012; and Muliadi et al., 2013) powder roll compaction models. The roll compaction parameters predicted by these models are the

roll force, the roll torque, the nip angle (the angle at which material no longer slips along the rolls), and the ribbon density. The necessary input parameters into these powder roll compaction models are the material internal friction angle, the material-wall friction angle, the roll compactor geometry, the roll speed, the material compression behavior, and the inlet boundary (nip region) conditions to the rolls. The inlet boundary conditions to the rolls, which include the stress and material density at the nip region of the rolls, are difficult to measure experimentally on a roller compactor because the nip region is completely enclosed by the roll compactor geometry. To measure the roll inlet conditions in the stream wise direction, a sensor would need to be placed within the nip region of the roll compactor; however, the limited space in the nip region makes this task difficult. Due to the inability to specify the roll inlet conditions, the comparisons between the powder roll compaction models and experimental results have been limited.

The focus of this thesis is therefore predicting the stress at the inlet nip region of a roll compactor so that direct comparisons between the powder roll compaction models and experimental results are possible. In order to predict the stress at the inlet nip region of a roll compactor, the Solid Plug model, developed for plastic screw extrusion processes, is applied to a powder feed screw of a roll compactor. The Solid Plug model predicts the stress along the length of the feed screw based on the feeder geometry, friction coefficients, stress ratio (ratio of principal stresses), feeder inlet stress, mass flow rate, feed screw speed, and material density. The Solid Plug model's predictions of the feeder outlet stress are compared to experimental measurements, and the Solid Plug model's sensitivity to the friction coefficients, stress-density relationship, and stress ratio are discussed. The applicability of the Solid Plug model to the powder roll compaction

models depends on the Solid Plug model's ability to predict the feeder outlet stress and the model's sensitivity to the input parameters.

Additionally, the Solid Plug model derivation will be extended to find a relationship between the feeder torque and the feeder outlet stress. Modeling the feeder torque-outlet stress relationship is desired because the feeder torque is an output given by certain roll compactors, for example the roll compactors manufactured by Gerteis (http://www.gerteis.com). Thus determining the feeder torque-outlet stress relationship would allow for the feeder outlet stress to be easily predicted.

CHAPTER 2. BACKGROUND

2.1 Roller Compaction Models

One-dimensional analytical models (Johanson, 1965; Katashinskii et al., 1983a; Katashinskii et al., 1983b; Katashinskii, 1986), 2-D and 3-D computational finite element models (Dec et al., 2003; Michrafy et al., 2004; Cunningham, 2005; Muliadi et al., 2012; Muliadi et al., 2013), and statistical scale up models (Zinchuk et al., 2004; Reynolds et al., 2010; Nesarikar et al., 2012a; Nesarikar et al., 2012b) which describe the roller compaction process can be found in the literature. The goal of the analytical and computational models is to predict the following process parameters: roll force, roll torque, maximum roll force, ribbon relative density, and nip angle (the angle at which the material no longer slips along the rolls). On a roll compactor either the roll gap or roll force can be controlled, in which case the prediction of the roll force and torque or the roll gap and roll torque, respectively, present the design space for the roll compactor application. The ability to predict ribbon relative density allows for process parameters to be adjusted such that a targeted ribbon density can be attained. Research has shown that ribbon density directly affects granule size and mechanical properties (Davies et al., 1996; Rowe et al., 1996; Hancock et al., 2003; Zinchuk et al., 2004). Modeling of the roller compaction process eliminates the initial trial and error method, which is expensive, wastes material, and takes time. Although roller compaction is conceptually simple,

quantitative understanding of the process has shown to be challenging due to the complexity of particulate material behavior.

The inputs into roller compaction models are the material internal friction coefficient, material-wall friction coefficient, system geometry, roll speed, material compression behavior, and the inlet boundary conditions to the rolls. The current work focuses on understanding the inlet boundary conditions to the rolls, which are also the feeder outlet boundary conditions. The inlet boundary conditions to the rolls are made up of the roll inlet stress (before the nip angle) and the material density. The material density can be determined from the inlet stress using a stress-density relationship. The remainder of this section examines the existing roller compaction models and the role of the inlet boundary conditions.

In the literature, the 1-D analytical Slab Method (Katashinskii et al., 1983a; Katashinskii et al., 1983b; Katashinskii, 1986) applies force and mass balances to trapezoidal material elements downstream of the nip region. The stress and density differential equations describing the powders stress/strain behavior, which result from force and mass balances, provide equations for the roll pressure distribution and ribbon density. Unlike the 1-D Johanson model (Johanson,1965), which is discussed next, the Slab Method requires the measurement of the nip angle. The nip angle can be experimentally measured using instrumented rolls (Bindhumadhavan et al., 2005), and is defined to be the angle between the two tangent lines drawn through the roll pressure profile. The need for measuring the nip angle in the Slab Method is one reason the Johanson model is applied more frequently in practice. Another reason the Johanson model is more frequently applied is because of the lack of experimental validation of the

Slab Method. The experimental validation of the Slab Method provided by Katashinskii et al. (1986) applied an assumed roll inlet condition, whereas Dec (1991) used the roll inlet condition as a fitting parameter. In the work of both Katashinskii et al. (1986) and Dec (1991), the Slab Method agreed qualitatively, but disagreed quantitatively with experimental results. The pressure distribution along the rolls predicted by the Slab Method was orders of magnitude different from those measured experimentally. Katashinskii et al. (1986) also found there to be no relation in the model between roll inlet stress and the final ribbon density, which did not match experiments. The important messages here are that the Slab Method gives incorrect results and the roll inlet conditions are not known a priori.

Before discussing the predictions of the 1-D Johanson model (Johanson, 1965) found in the literature, how the stress at the inlet of the nip region in a roll compactor (σ_0) affects the Johanson model is discussed. The geometry applied in the Johanson model is shown in Figure 2.1. The Johanson model splits the roll compactor geometry into two regions, which are divided at the nip angle (α). For roll angles (θ) greater than the nip angle the material is assumed to slip along the rolls, and for roll angles less than the nip angle a no-slip state is assumed along the rolls (Figure 2.1). The determination of the nip angle is therefore very important and its derivation is outlined below.

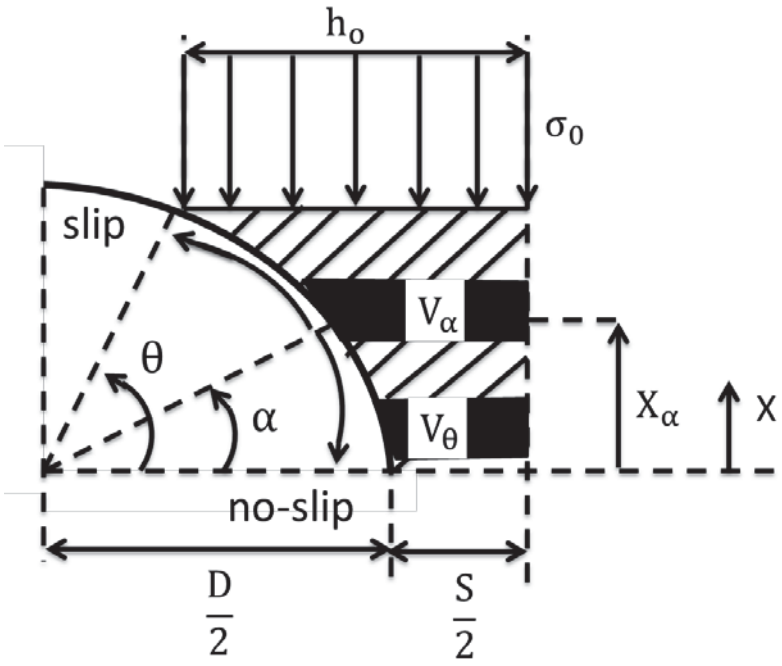

Figure 2.1. Roll compactor geometry applied in the derivation of the 1-D Johanson model.

The Johanson model assumes that the material in the slip region follows the Jenike-Shield yield criterion (Jenike et al., 1959). This assumption allows for the stress gradient normal to the rolls, $d\sigma/dx$, to be defined in terms of the roll-material friction coefficient (ϕ), material internal friction coefficient (δ), and roll compactor geometry,

$$\left(\frac{d\sigma}{dx}\right)_{slip} = \frac{4\sigma\left[\left(\frac{\pi}{2}\right) - \theta - v\right]\tan(\delta)}{\left(1 + \frac{S}{D} - \cos(\theta)\right)\left[\cot(A-\mu) - \cot(A+\mu)\right]}, \tag{2.1}$$

where S is the roll gap, D is the roll diameter, and A, μ, and ν are defined as,

$$A = \frac{1}{2}\left(\theta + v + \frac{\pi}{2}\right), \tag{2.2}$$

$$\mu = \frac{\pi}{4} - \frac{\delta}{2}, \tag{2.3}$$

and,

$$v = \frac{1}{2}\left[\pi - \sin^{-1}\left(\frac{\sin(\phi)}{\sin(\delta)}\right) - \phi\right]. \tag{2.4}$$

When the material does not slip along the rolls, Johanson argues that the Jenike-Shield yield criterion no longer holds. Instead, the streamwise stress gradient in the no-slip region is derived from a conservation of mass argument. Applying conservation of mass to the two material elements shown in Figure 2.1 requires that the densities (ρ) and volumes (V) satisfy the following relationship,

$$\frac{V_\alpha}{V_\theta} = \frac{\rho_\theta}{\rho_\alpha}. \tag{2.5}$$

The relationship between the material volumes and densities (Equation (2.5)) is then substituted into an experimentally determined stress-density relationship,

$$\frac{\sigma_\alpha}{\sigma_\theta} = \left(\frac{\rho_\alpha}{\rho_\theta}\right)^K, \tag{2.6}$$

in order to relate the roll normal stress and material volume,

$$\frac{\sigma_\theta}{\sigma_\alpha} = \left(\frac{V_\alpha}{V_\theta}\right)^K, \tag{2.7}$$

where σ_θ is the roll normal stress at a roll angle less than the nip angle, σ_α is the roll normal stress at the nip angle, and K is an experimentally determined constant. The parameter K is related to the materials compressibility, with larger K values corresponding to less compressible materials. The volumes of the material elements shown in Figure 2.1 defined in terms of the roll gap, roll diameter, and roll angle are given by,

$$V_\theta = \left(1 + \frac{S}{D} - \cos(\theta)\right)\cos(\theta), \tag{2.8}$$

and,

$$V_\alpha = \left(1 + \frac{S}{D} - \cos(\alpha)\right)\cos(\alpha). \tag{2.9}$$

Substituting Equations (2.8) and (2.9) into Equation (2.7) gives,

$$\frac{\sigma_\theta}{\sigma_\alpha} = \left(\frac{\left(1 + \frac{S}{D} - \cos(\alpha)\right)\cos(\alpha)}{\left(1 + \frac{S}{D} - \cos(\theta)\right)\cos(\theta)}\right)^K. \tag{2.10}$$

Noting that x equals,

$$x = \frac{D}{2}\sin(\theta), \tag{2.11}$$

the stress gradient in the no-slip region is given by,

$$\frac{d\sigma}{dx}_{no-slip} = \frac{K\sigma_\theta\left(2\cos(\theta) - 1 - \frac{S}{D}\right)\tan(\theta)}{\frac{D}{2}\left[\left(1 + \frac{S}{D} - \cos(\theta)\right)\cos(\theta)\right]} \tag{2.12}$$

Assuming that the stress gradient along the rolls is continuous, Equations (2.1) and (2.12) can be equated when setting the roll angel equal to the nip angle ($\theta = \alpha$),

$$\frac{4\sigma\left[(\pi/2) - \alpha - v\right]\tan(\delta)}{\left(1 + \frac{S}{D} - \cos(\alpha)\right)\left[\cot(A - \mu) - \cot(A + \mu)\right]} = \frac{K\left(2\cos(\alpha) - 1 - \frac{S}{D}\right)\tan(\alpha)}{\cos(\alpha)}. \tag{2.13}$$

The nip angle can then be determined from Equation (2.13).

The remainder of the Johanson model discussion will focus on how the stress at the inlet of the nip region in a roll compactor (σ_0) affects the Johanson model. First the

relationship between the roll inlet stress and the stress distribution along the rolls will be determined. For a roll angle greater than the nip angle ($\theta > \alpha$), the stress distribution along the rolls can be determined given the Jenike-Shield yield criterion, assumed slip condition along the rolls, and roll inlet stress. The stress acting on the rolls horizontally is assumed to be the major principal stress (σ_1), making the roll inlet stress the minor principal stress ($\sigma_2 = \sigma_0$), because they act perpendicular to each other. The following relationship between the major and minor principal stresses can be derived from Figure 2.2,

$$\sin(\delta) = \frac{\sigma_1 - \sigma_2}{\sigma_1 + \sigma_2}. \tag{2.14}$$

The mean roll normal stress (σ) at the inlet to the rolls is then given by,

$$\sigma = \frac{\sigma_0}{1 - \sin(\delta)}. \tag{2.15}$$

For roll angles greater than the nip angle Equation (2.15) shows that the roll normal stress is proportional to the roll inlet stress and independent of the roll angle.

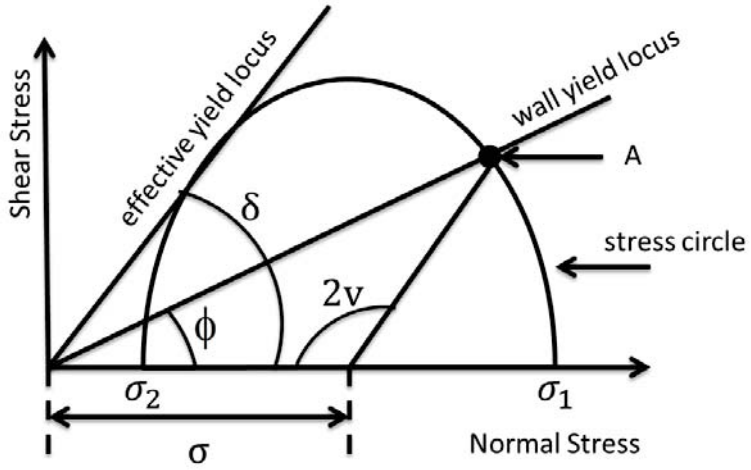

Figure 2.2. Mohr's circle diagram showing the major (σ_1) and minor (σ_2) principal stresses.

When the roll angle is less than the nip angle ($\theta < \alpha$), the roll normal stress is given by Equation (2.10). Again, Equation (2.10) was derived using a conservation of mass argument. Assuming that the stress is continuous along the rolls, the stress at the nip angle can then be described by Equation (2.15). Substituting Equation (2.15) into Equation (2.10) provides a relationship between the roll normal stress on the rolls after the nip angle and the roll inlet stress,

$$\sigma_\theta = \frac{\sigma_0}{1-\sin(\delta)}\left(\frac{\left(1+\frac{S}{D}-\cos(\alpha)\right)\cos(\alpha)}{\left(1+\frac{S}{D}-\cos(\theta)\right)\cos(\theta)}\right)^K . \tag{2.16}$$

The roll normal stress before and after the nip angle are given by Equations (2.15) and (2.16), respectively. Both Equation (2.15) and (2.16) show that the roll normal stress is proportional to the roll inlet stress.

Once the stress distribution along the rolls is determined, the roll force and roll torque can be derived. The following equations for the total roll force and roll torque integrate the roll stress distribution over the entire roll surface,

$$\text{Roll Force} = \sigma_m WD \int_{\theta=0}^{\theta=\alpha} \left[\frac{\frac{(1+S)}{D}}{\frac{1}{D}+\left(1+\frac{S}{D}-\cos(\theta)\right)\cos(\theta)}\right]^K \cos(\theta)\,d\theta , \tag{2.17}$$

and,

$$\text{Roll Torque} = \sigma_m WD^2 \int_{\theta=0}^{\theta=\alpha} \left[\frac{\frac{(1+S)}{D}}{\frac{1}{D}+\left(1+\frac{S}{D}-\cos(\theta)\right)\cos(\theta)}\right]^K \sin(2\theta)\,d\theta \tag{2.18}$$

The upper bound on the integrals is set as the nip angle, because the stress along the rolls for roll angles greater than the nip angle has been shown to be negligible. Both the roll force and the roll torque are given in terms of the roll compactor geometry, material compressibility, and the maximum stress along the rolls (σ_m). The maximum stress along the rolls is determined by setting the roll angle in Equation (2.16) equal to zero; this is the point where the roll gap is minimized. Like the stress distribution, the roll force and roll torque are proportional to the roll inlet stress. Lastly, the ribbon density can be determined from the stress-density relationship. Rearranging Equation (2.6) gives the following relationship between the roll inlet stress and the ribbon density,

$$\rho_m = \rho_0 \left(\frac{\sigma_0}{\sigma_m} \right)^K . \tag{2.19}$$

The comparisons between the 1-D Johanson model and experimental measurements found in the literature will now be discussed, while focusing on the effects of the roll inlet boundary conditions. The work of Bindhumadhavan et al. (2005) illustrates the importance of the roll inlet stress. Bindhumadhavan et al. (2005) used the roll inlet stress as a fitting parameter, as was done by Dec (1991), to match the Johanson model roll pressure profile predictions to the experimental results. Although Bindhumadhavan et al. (2005) did show that the Johanson model was able to predict the nip angle, which is independent of the roll inlet stress, to within 15%, using the roll inlet stress as a fitting parameter did not allow for predictions of the other parameters to be validated.

The sensitivity of the Johanson model to the inlet boundary conditions seen by Bindhumadhavan et al. (2005) are also shown in the experimental work of Yusof et al.

(2005), where a 10% increase in the material density at the inlet to the rolls caused the predicted roll force to increase by a factor of three. A 10% increase in material density was reasonable due to the scatter in the measured material density. In the case of Yusof et al. (2005), the roll compactor was gravity fed and the roll inlet stress was assumed equal to the hydrostatic stress of the material upstream of the rolls. Assuming that the roll inlet stress equaled the material hydrostatic stress allowed the Johanson model to give reasonable predictions of the roll force and roll torque, although the predictions were sensitive to the roll inlet boundary parameters.

Finite element models (Dec et al., 2003; Michrafy et al., 2004; Cunningham, 2005; Muliadi et al., 2012; Muliadi et al., 2013) of the roller compaction process primarily focus on comparing predictions with the 1-D Johanson model. The material in the FEM models is treated as a continuum, but is divided into elements by applying a meshing scheme. The material elements deform based on the stresses applied and according to the stress/strain relationship of the material, which is given by constitutive relationships. Often the constitutive relationship applied to the FEM powder roll compaction models is the Drucker-Prager Cap (DPC) model (Sinka et al. 2003). The main advantages of the finite element models are their ability to predict multidimensional velocity and density distributions in the material, and that they require fewer assumptions than the Johanson model. For example, the regions where the slip/no-slip boundary conditions apply on the rolls do not have to be defined in the FEM models. The disadvantages of FEM models are that they take a long time to run, are more computationally expensive than the Johanson model, require a user with an FEM skill base, and need several material input parameters from time consuming material characterization experiments. Since the FEM

models only model the nip region of the roll compactor, they still require that the roll inlet boundary conditions be defined. The results of the FEM models are discussed in the following paragraphs. Again, the discussion focuses on the effects of the roll inlet boundary conditions.

While the findings of the FEM models focus on the density and velocity distributions of the material in the nip region of the roll compactor, the significance of the roll inlet stress to the FEM simulations was demonstrated by Dec et al. (2003) and Muliadi et al. (2012). Dec et al. (2003) observed that doubling the roll inlet stress nearly doubled the roll pressure profile predictions of their FEM model. The work of Muliadi et al. (2012) demonstrated that the ribbon relative density and the maximum roll normal stress predictions of both the FEM and Johanson models increased as the roll inlet stress increased; however, the FEM model (Muliadi et al., 2012) is shown to be much less sensitive to changes in the roll inlet stress than the Johanson model. Increasing the roll inlet stress by a factor of four is shown to only increase the maximum roll normal stress predictions of the FEM model by a few percent, whereas the Johanson model maximum roll normal stress predictions are shown to be proportional to the roll inlet stress (Muliadi et al., 2012).

Dec et al. (2003) stated that before comparing the FEM models to experiments, the roll inlet boundary conditions must be better understood. For this reason most FEM models are not compared to experimental results. The only comparison between a powder roll compaction FEM model and experimental measurements was done by Muliadi et al. (2013). The comparison between a 3-D FEM model and experimental work was made possible by altering a roll compactor. The feed screw of a roll compactor

was removed and a piston that could apply a specified inlet stress to the rolls was put in the feed screw's place. With the roll inlet boundary conditions specified the FEM model results were shown to predict the experimental results to within experimental uncertainties.

The only attempt to measure the inlet stress on a standard roll compactor was done by Cunningham (2005). Cunningham (2005) placed a load cell on the cheek plate of a roll compactor in order to measure the roll inlet stress, yet the streamwise inlet stress condition is expected to be different than that at the cheek plate. The stress is expected to be different in the streamwise direction because unlike fluids, the stresses in powders are dependent on the surface normal directions. The stress at the cheek plate, however, can be related to the stress in the streamwise direction by multiplying the stress at the cheek plate by the stress ratio. Assuming that the stress in the steamwise direction is the major principal stress, the stress ratio is given by the ratio of the stress at the cheek plate to the stress in the streamwise direction. The stress ratio will be discussed more in the following section. Other than this single attempt and the modifications to a roll compactor made by Muliadi et al. (2013), the inlet boundary conditions are either assumed or used as a fitting parameter for the models.

In the literature there is an obvious need for understanding the inlet boundary conditions of a roll compactor. It has been shown that the inlet boundary conditions affect the roll pressure profile, maximum roll normal stress, and ribbon densities. However, despite experimental work and FEM simulations showing the effects of the inlet boundary conditions, the Johanson model is still widely used because it is computationally cheap and easy to apply. These features of the Johanson model make it

ideal for first pass design and online control purposes. An understanding of the roll inlet conditions would then be a useful contribution.

2.2 Solid Plug Model

Feed screws, such as those used in roll compactors, are applied in many industries (food, pharmaceutical, bio-fuel, plastic extrusion, and coal mining) to continuously convey particulate material. Due to their many applications, feed screws are widely discussed in literature. The work in this thesis applies a 1-D feed screw model developed in the field of plastic extrusion to a feed screw in a powder roll compactor in order to predict the roll inlet boundary conditions. The necessity of understanding the roll inlet boundary conditions of a roll compactor were highlighted in the previous section.

The process of plastic extrusion conveys plastic pellets while melting them into a liquid. There are three distinct zones of a plastic extrusion feed screw: the solid conveying zone, the melting zone, and the melt conveying zone (Tadmor et al., 1972). Models have been developed for each zone; however, there is lack of understanding and research for the solid conveying zone. Tadmor et al. (1972) has shown the mass flow rate of the entire plastic extrusion feeder to be limited by the solid conveying zone; therefore, the solid conveying zone has gained interest in the literature of plastic extrusion feeders. The solid conveying zone is the portion of the feed screw where the plastic pellets are conveyed before any effects of melting occur. The entire feed screw in a roll compactor is classified as a solids conveying zone.

The 1-D analytical Solid Plug model developed for the solid conveying zone of a feed screw by Darnell et al. (1956) is the basis of all subsequent Solid Plug models

developed (Tadmor et al., 1972; Lovegrove et al., 1973a; Campbell et al., 1995; Hyun et al., 1997a). All Solid Plug models apply the following assumptions:

1. The material between the flights of the feed screw is treated as a continuum.
2. The material completely fills the screw channel making contact with all boundary surfaces.
3. The material only moves in the down channel direction, and as the material moves axially along the screw, the velocity in the down channel direction is constant.
4. The material density is constant along the length of the screw.

Additionally, in the Solid Plug model derivation the feed screw is held stationary and the barrel is rotated. The coordinate system applied in the Solid Plug model is attached to the material in the screw channel such that the barrel moves relative to the material.

Before discussing the findings in the literature regarding the Solid Plug model, the Solid Plug model derivation is outlined in the following paragraphs. A more complete derivation of the Solid Plug model is given in Chapter 4. The Solid Plug model derivation outlined follows that of Tadmor et al. (1972). The only difference between the Solid Plug model developed by Darnell et al. (1956) and Tadmor et al. (1972) is that Darnell et al. (1956) assumed the friction coefficients of the feed screw and barrel to be equal. As the Solid Plug model derivation is presented, alterations to the Solid Plug model developed by Tadmor et al. (1972) by different individuals will be highlighted. The terminology of the feeder geometry used in the derivation below is presented in Figure 2.3. Note that the material in all figures is being conveyed to the right.

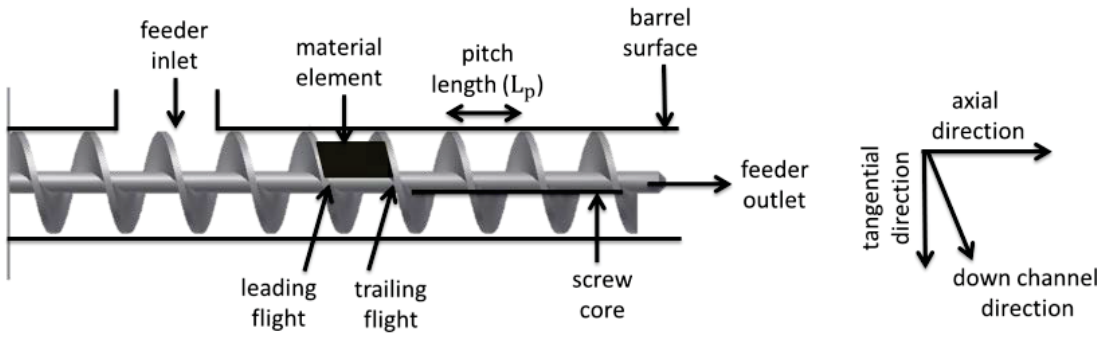

Figure 2.3. Schematic of a feeder defining the feed screw terminology.

The Solid Plug model first determines the forces acting on a differential material element in a screw channel due to the boundary surfaces, which are the: barrel (dF_b), screw core (dF_{sc}), leading screw flight (dF_{lf}, dF_{lf_μ}), trailing screw flight (dF_{tf}, dF_{tf_μ}), material upstream of the material element (dF_{us}), and material downstream of the material element (dF_{ds}), where μ denotes the frictional force on the respective surface (Figure 2.4). An unknown force is also applied at the leading screw flight (dF^*) to balance the forces.

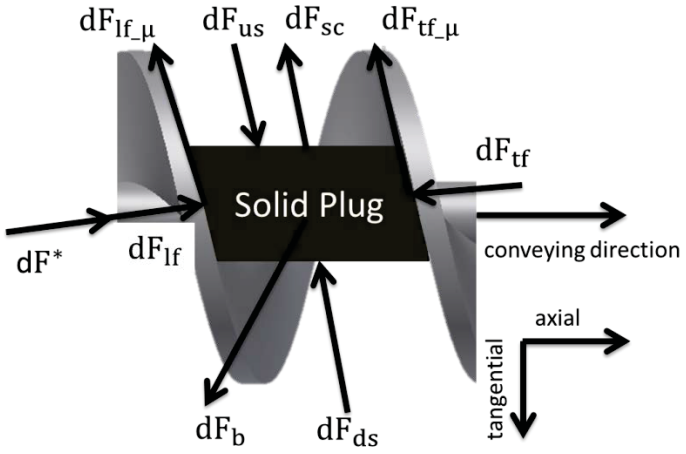

Figure 2.4. Forces acting upon a material element within a screw channel (Tadmore et al., 1972).

The Solid Plug models developed by Campbell et al. (1995) and Hyun et al. (1997a) differ from that developed by Tadmor et al. (1972) in their application of the unknown force at the leading screw flight. The derivation of the Campbell model assumes that the unknown force at the leading screw flight is equal to the force due to the barrel ($dF^* = dF_b$) (Figure 2.5), the reason for this assumption is discussed in the paragraphs below. The Hyun model applies the unknown force at an angle (φ) to the leading screw flight (Figure 2.6), however no reason is specified why this is done.

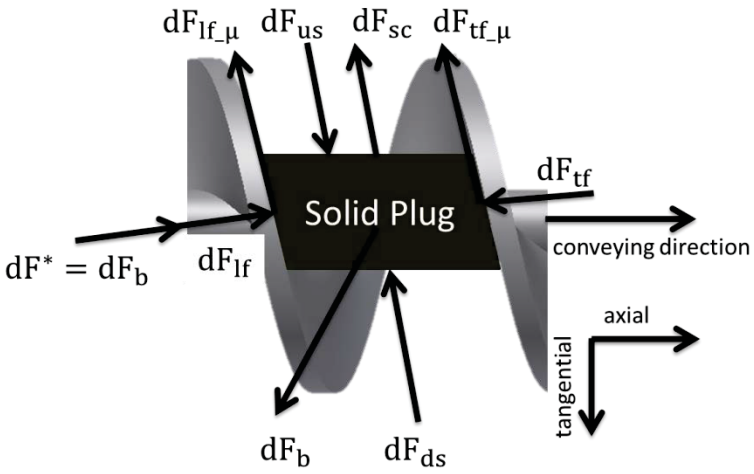

Figure 2.5. Forces acting upon a material element within a screw channel (Campbell et al., 1995).

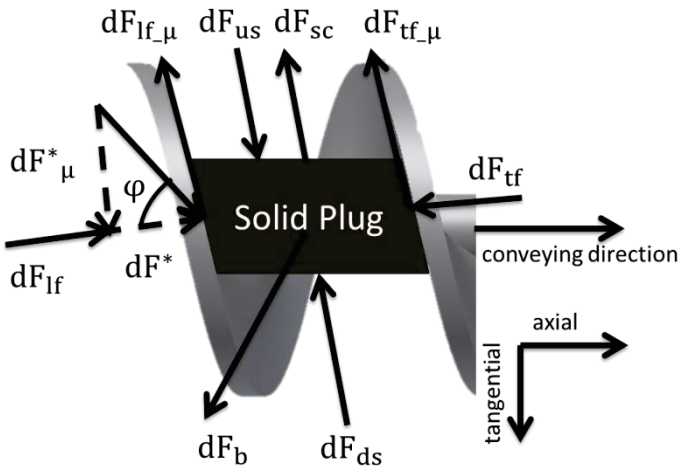

Figure 2.6. Forces acting upon a material element within a screw channel (Hyun et al., 1997a).

After determining the forces which act on the material element, all of the Solid Plug models, except for the model developed by Campbell et al. (1995), break down the forces into their axial and tangential components so that a force balance in the axial direction and a torque balance in the tangential direction can be applied. Shown in Equations (2.20) and (2.21) are the force and torque balances, respectively, given by the Tadmor model,

$$- dF_{b\_a} - dF_{sc\_a} - dF_{lf\_\mu a} - dF_{tf\_\mu a} - dF_{ds\_a} + dF_{us\_a} + dF_{lf\_a} - dF_{tf\_a} + dF_a^* = 0, \tag{2.20}$$

and,

$$-\frac{D_b}{2}dF_{b\_t} + \frac{D_{sc}}{2}dF_{sc\_t} + \frac{\overline{D}}{2}dF_{lf\_\mu t} + \frac{\overline{D}}{2}dF_{tf\_\mu t} + \frac{\overline{D}}{2}dF_{ds\_t} - \frac{\overline{D}}{2}dF_{us\_t} + \frac{\overline{D}}{2}dF_{lf\_t} - \frac{\overline{D}}{2}dF_{tf\_t} + \frac{\overline{D}}{2}dF_t^* = 0, \tag{2.21}$$

where the subscripts a and t stand for the axial and tangential components of the forces, and D_b, D_{sc}, and $\overline{D}$ are the barrel, screw core, and average diameters.

The Campbell model does not apply a torque balance because the Campbell model treats the material in the feed screw as a fluid, whereas the other models treat the

material as a solid, and a torque balance cannot be applied to a fluid. Since a torque balance cannot be applied to a fluid, the Campbell model only applies a force balance. With only one equation there cannot be any free variables, and for this reason the Campbell model assumes the unknown force at the leading screw flight is equal to the force due to the barrel.

Once the force and torque balance equations are determined, they are simultaneously solved to eliminate the unknown force at the leading screw flight. After eliminating the unknown force, there is only one equation which depends on the forces acting at the barrel, screw core, leading screw flight, trailing screw flight, material boundaries, and the feeder geometry. These forces are then defined in terms of the stresses at the respective surfaces and the areas over which they act. The Solid Plug models differ again in their definitions of the stresses acting at the barrel, screw core, and screw flight surfaces. In all Solid Plug models the stresses due to the material upstream and downstream of the differential material element are, however, equal to the stress in the down channel direction (σ).

The stresses in a liquid are independent of the material surface normal direction, therefore the stresses at the boundary surfaces in the Campbell model are equivalent. The Tadmor model reaches the same conclusion by assuming that the stresses in the material are isotropic. The Hyun model, however, assumes that the stresses in the material are anisotropic, meaning that the stresses in the material are direction dependent; though Hyun et al. (1997a) also assumes that the stress acting at the boundaries can be related to the stress in the down channel direction by a single stress ratio (k). The stress ratio will

be discussed in greater depth in the following two paragraphs and then the Solid Plug model derivation will be concluded.

The stress ratio applied in the Solid Plug model developed by Hyun et al. (1997a) is defined as the ratio of principal stresses in the material ($k = \sigma_2/\sigma_1$), similar to "Janssens's constant" (Janssen, 1895). The major (σ_1) and minor (σ_2) principal stresses act on the material surfaces which are subjected to zero shear stress, shown in a Mohr's circle diagram in Figure 2.2. In the Hyun model the major principal stress is assumed to act in the down channel direction, while the minor principal stress acts at the barrel, screw core, and screw flight boundaries. The stress ratio applied in the work of Hyun et al. (1997a) is experimentally measured using a punch and die experimental setup, where the radial stress is taken as the minor principal stress and the axial stress is taken as the major principal stress (Figure 2.7).

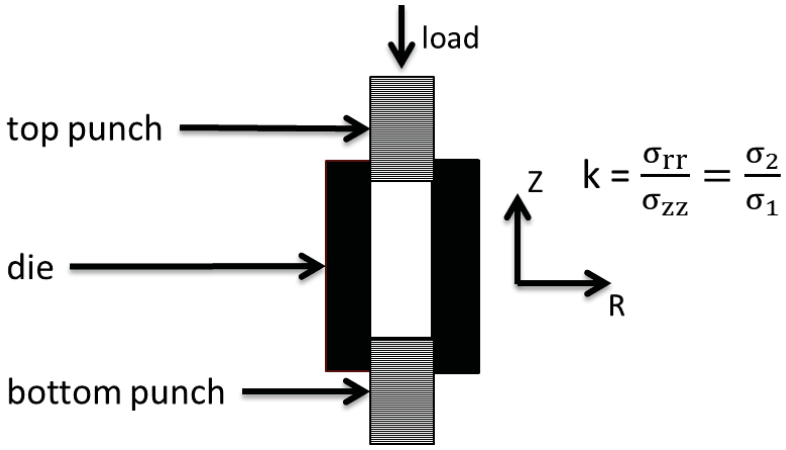

Figure 2.71. Schematic of a punch and die experimental setup.

The stress ratio applied at the boundaries is important because it affects the magnitude of the forces acting on the material in the feed screw and the magnitudes of the forces affect the feeder outlet stress predictions of the Solid Plug model. The

sensitivity of the Solid Plug models to the stress ratio is discussed in Chapter 8, because of its uncertainty. The stress ratio measured by Hyun et al. (1997a) and those given in the literature for static material are all less than one, whereas for material that is being sheared, which is representative of material in a feed screw, the kinetic theory of granular materials (Lun, 1991) predicts a stress ratio of one. The stresses measured at the boundaries in a discrete element model (Moysey et al. 2004) of a feed screw give results different than those assumed by Hyun et al. (1997a) and predicted by the kinetic theory of granular materials (Lun, 1991). The stresses at each boundary are shown to be different in the discrete element model. The stress ratios measured in the discrete element model (Moysey et al. 2004) are discussed in the next section and the stress ratio predicted by the kinetic theory of granular materials is discussed in Chapter 5 when determining which stress ratio to apply to the Solid Plug model.

Getting back to the Solid Plug model derivation, once the forces acting on the material are defined in terms of stresses at the boundaries and areas over which they act, the following differential equation results,

$$\frac{d\sigma}{dL} = \frac{(KB_1 - A_1)}{(KB_2 + A_2)}\sigma, \tag{2.22}$$

where $A_1, A_2, B_1, B_2,$ and K depend on the feeder geometry, friction coefficients, and the conveying angle, which depends on the mass flow rate, and material density. The conveying angle will be discussed in Chapter 4. Again, Equation (2.22) is the result of the Solid Plug model developed by Tadmor et al. (1972). The results of the Solid Plug models developed by Campbell et al. (1995) and Hyun et al. (1997a) are shown in Chapter 4 along with the full derivation of the Tadmor model. Note, however, that

applying the unknown force at the leading screw flight perpendicular to the screw flight in the Hyun model ($\varphi = 0$) and assuming a stress ratio of one (k = 1), the Hyun model is exactly the Tadmor model. Solving Equation (2.22) allows for the feeder outlet stress to be calculated.

In the plastic extrusion literature, Equation (2.22) is solved for the mass flow rate because the mass flow rate is a critical parameter in plastic screw extrusion processes. How Equation (2.22) can be solved for the mass flow rate will become apparent in Chapter 4 when the Solid Plug model is fully derived and the parameters $A_1, A_2, B_1, B_2,$ and K are defined. The mass flow rate determines how long the materials are subjected to the applied temperatures which melt the pellets. Too high or too low of a mass flow rate either produces un-melted pellets or degraded material. In the current work, however, the Solid Plug model will be applied to predict the feeder outlet stress, a necessary boundary condition for powder roll compaction models.

While the Solid Plug models discussed to this point have neglected body forces, Lovegrove et al. (1973a, 1973b, 1974) accounted for the gravitational and centrifugal body forces. The body forces were accounted for by Lovegrove et al. (1973a, 1973b) so that the Solid Plug model predicted what was observed experimentally. Lovegrove et al. (1974) experimentally observed that the mass flow rate of a feed screw did not depend on the hopper fill level, experimentally testing this with a hopper completely full, half full, and nearly empty. The Solid Plug models however, which take the feeder inlet stress to be the Janssen hopper stress (Janssen, 1895) at the hopper outlet, predict a decrease in mass flow rate due to a decrease in the hopper fill level, because the hopper fill level affects the feeder inlet stress. Accounting for the gravitational and centrifugal body

forces causes a stress generation in the feed screw even if the feeder inlet stress is zero, allowing for the Solid Plug model to predict a mass flow rate when the hopper is empty. Adding the body forces to the Solid Plug model gives the following equation,

$$\frac{d\sigma}{dL} = \frac{(KB_1 - A_1)}{(KB_2 + A_2)}\sigma + \underbrace{C_1\gamma}_{\text{gravitational body force}} + \underbrace{C_2\gamma\left(\frac{D\omega^2}{g}\right)}_{\text{centrifugal body force}}, \tag{2.23}$$

where C_1 and C_2 depend on the feeder geometry and friction coefficients, γ is the materials specific weight, and ω is the radial velocity. Lovegrove et al. (1973b) state that the centrifugal force can be neglected at screw speeds lower than 100 rpm. Typical roller compactor feed screws are run below 100 rpm and so the centrifugal force is reasonably neglected. Despite Lovegrove's work, the literature for Solid Plug models does not incorporate these body forces because they are negligibly small and only play a role if the feeder inlet stress is zero. In the literature it is assumed that the feeder inlet stress is not zero, therefore the first term in Equation (2.23) dominates the Solid Plug model predictions.

One last comment on the development of Solid Plug models: while most of the Solid Plug models applied in the literature assume constant material properties and feeder geometry along the axial length of the feed screw, the work of Broyer et al. (1972) and Hyun et al. (1997a) allowed for parameters to vary along the length of the feed screw. Broyer et al. (1972) accounted for non-isothermal and non-constant geometry effects, while the work of Hyun et al. (1997a) allowed the friction coefficients and material density to be stress and temperature dependent (Hyun et al., 1990; Spalding et al., 1993; Hyun et al., 1997a; Hyun et al., 1997b; Spalding et al., 1997). Applying the non-constant

parameters forced the Solid Plug models to be solved stepwise along the length of a feed screw.

The non-isothermal effects are important in plastic extrusion because they allow the point at which the pellets melt to be calculated. Knowing where the pellets melt gives the length of the solid conveying zone. Additionally, a non-constant geometry is applied because plastic extrusion feed screws often have tapered screws. Although non-isothermal effects are not expected to be important in a roll compaction feeder and most roll compaction feed screws have constant geometry, one can allow properties such as density to vary along the feeder length.

Now that the Solid Plug models presented in the literature have been discussed, the findings of the Solid Plug models in the literature will discussed in the following paragraphs. Due to the difficulty of measuring the feeder outlet stress, similar to the roll compactor inlet boundary condition, there are few experimental comparisons in the literature. The literature focuses mostly on analytical predictions of the Solid Plug model and investigates the effects of the outlet stress, friction coefficients, screw flight angles, and screw channel depth.

First the few experiments performed to validate the following Solid Plug model assumptions:

1. The material between the flights of the feed screw is treated as a continuum (i.e., a solid plug).
2. The material completely fills the screw channel making contact with all boundary surfaces.

3. The material only moves in the down channel direction, and as the material moves axially along the screw, the velocity in the down channel direction is constant.

will be discussed. The difficulty in verifying these assumptions comes from a lack of understanding the feeder dynamics. In order to view the feeder dynamics during experiments, Darnell et al. (1956) and Zhu et al. (1991) used barrels that had viewing windows. While these windows allowed for viewing, the friction differences between the barrel and windows could skew the observations and results.

Darnell observed bridging of particles across screw channels which caused damming of the conveyed material. Breaking of the dam would then cause a surge of material. Material was also observed to move along the screw flights, as well as slide and tumble from side to side. The assumption of plug flow was identified as an average representation of what occurred in the feeder. The experimental observations of particle movement in the screw channel made by Darnell et al. (1956) coincided with those of Zhu et al. (1991). Zhu et al. (1991) witnessed plug flow occurring closer to the end of the solid conveying zone where materials were more compressed. The location where the solid plug formed moved closer to the feeder inlet as the applied outlet stress increased. As the particle size and hardness increased, the less the particle flow in the feeder resembled plug flow. Larger particles also resulted in smaller screw channel fill levels. The application of the Solid Plug model to pharmaceutical powders seems reasonable still since the particle sizes are smaller and more compressible than the plastic particles used in the experiments performed by Darnell et al. (1956) and Zhu et al. (1991). The

pharmaceutical powders which are used in dry granulation processes are used because they are compressible.

Darnell et al. (1956) analytically investigated the Solid Plug model for various outlet stress conditions, showing that the Solid Plug model predicts a greater mass flow rate with lower applied outlet stress. Darnell et al. (1956) also showed that when the barrel and screw friction coefficients were assumed equivalent and the outlet stress was greater than the inlet stress, the Solid Plug model predicted no mass flow rate. Although the Solid Plug model was not directly compared with experiments, these predictions agree with experimental observations where the outlet stress acts as a retarding force on the conveyed material.

Darnell et al. (1956) also performed experiments to observe the effects of the barrel and screw friction coefficients, for open outlet conditions, on mass flow rate. The experiments were performed with three screws and three barrels. The three screws had the same roughness but different geometry, whereas each of the three barrels had a different roughness but identical geometry. The three barrels were described as having a mirror-like finish, a machined surface similar to the screws used in the experiments, and the last barrel was grooved and pitted. Although the roughness of the barrels was not measured, it was obvious that the roughest barrel was the grooved barrel and the smoothest barrel was the mirror-like finished barrel. Since the surface roughness of the barrels and screws were not measured, the Solid Plug model could only be compared qualitatively. The model matched the experiments in predicting that the mass flow rate would increase with higher barrel friction coefficients and lower screw friction coefficients. The screw friction acts as a retarding force on the conveyed material and the

barrel friction acts as a driving force. These same predictions were made by Decker et al. (1941); however, there was no model that could capture these predictions. It is clear from the work of Darnell et al. (1956) and Tadmor et al. (1972) that the friction and outlet stress directly affect the mass flow rate.

The work of Campbell et al. (1995) focuses solely on analytical predictions of the Solid Plug model. The Solid Plug model developed by Campbell et al. (1995), like the Darnell model, predicts increased mass flow rate for greater barrel friction coefficients and lower screw friction coefficients. The Campbell model does not, however, automatically predict a zero mass flow rate when the friction coefficients are equal or even when the screw friction is greater than the barrel friction. Like the Darnell model the Campbell model is used to aid feeder design by investigating effects of parameters such as the screw flight angle, channel depth, and channel width.

The few comparisons between the Solid Plug model predictions and experimental results will now be presented. The main contribution by Lovegrove et al. (1974) is the comparison between theory and experimental results for feeders with an applied outlet stress. The experimental setup of Lovegrove et al. (1974) allowed outlet stress to build up due to a load ring at the outlet of the feeder. This experimental setup was first used by Schenkel et al. (1961). The load ring setup only allows material to flow from the feeder when the load applied by the conveyed material is greater than the load applied by the load ring. The outlet stress was measured by a pressure transducer inserted into the barrel, not from the load ring due to the complexity of the setup.

Lovegrove et al. (1974) observed pulsing of the material from the feeder outlet, which meant that the load applied by the conveyed material also had a pulsing

characteristic. The pulsing of the load could be seen in the movement of the lever arm of the load ring. Lovegrove et al. (1974) attributed the pulsing load to gravitational effects, likely stemming from the flow of the material in the hopper. The experimental results were able to demonstrate the effects of outlet stress on mass flow rate. The Solid Plug model predictions differed from experimental results by a few percent to approximately 30% depending on the material, feeder geometry, and assumed friction coefficient. The materials used were PVC and polyethylene. The experimental errors for trials performed with the PVC were attributed to the cohesiveness of PVC, which caused the screw flights to not be completely full. Partially filled screw flights resulted in poor predictions from the Solid Plug model because the Solid Plug model assumes completely filled screw flights.

The Solid Plug model, however, captures the trend of the experimental data which supports the fundamental approach. Lovegrove et al. (1974) shows that small variations in density and friction coefficients allow for the Solid Plug model to match experimental results. Although these results look promising, the friction coefficients were assumed values and the material density was assumed to be constant, thus it is difficult to say exactly how well the model predicts the results. Additionally the stress ratios for both PVC ($k = 0.25$) and polyethylene ($k = 0.30$) were not directly measured but taken as constants. The stress ratio values taken by Lovegrove et al. (1947) for PVC and polyethylene were based on experimental measurements made by G.M. Gale (1971). The experimental measurements made by G.M. Gale (1971) were made available through communication between the two parties.

The most complete experimental and analytical work for the Solid Plug model is performed by Hyun et al. (1997a). All necessary parameters for the Solid Plug model were directly measured. The stress ratio was experimentally measured using a punch and die setup (Spalding et al., 1997), the effects of stress and temperature on bulk density were measured (Hyun et al., 1990), and the friction coefficients were directly measured (Spalding et al., 1993). All of this physical property data was then applied to the Solid Plug models presented by Darnell et al. (1956) and Campbell et al. (1995) to compare the models to experimental data. The experimental setup was originally devised by Gogos et al. (1994) and allowed for the streamwise outlet stress to be measured, whereas the stress measured by Lovegrove et al. (1974) was at the barrel wall. The trend between the Solid Plug models and experimental measurements was that the Darnell model under-predicted and the Campbell model over-predicted the mass flow rate. The Solid Plug model proposed by Darnell was off by more than 50% and the Campbell model varied from the experimental results by 25%. The application of the stress ratio increased the error of the Darnell model and decreased the error of the Campbell model as expected, since the stress ratio reduces the mass flow rate for a given outlet stress. Neither model predicted the experimental data well except for the open outlet condition where no outlet stress was applied.

After observing that neither Solid Plug model predicted the experimental outcomes, Hyun et al. (1997a) applied the adjustments to the Solid Plug model discussed in the beginning of this section. The model proposed by Hyun et al. (1997a) is shown to have much better agreement with the experimental results, fitting between the Darnell and Campbell model. All models applied the same material parameters. The Hyun

model is proposed to replace the standard Darnell model used in the field of plastic screw extrusion.

This section highlighted the Solid Plug models developed for the solid conveying zone of a feed screw in the field of plastic extrusion. The findings in the literature show that the assumption of plug flow is dependent on feed screw geometry and particle size, but plug flow was seen as an average representation of the material flow in a feed screw. There are few comparisons between the Solid Plug model and experimental results, the most complete comparison performed by Hyun et al. (1997a) showed varying accuracy for the different Solid Plug models. In this thesis the Solid Plug models will be applied to a powder feed screw of a roll compactor in order to attain an understanding of the roll inlet conditions.

2.3 Higher Order Feeder Models

To further understand and capture the dynamics of a feed screw, 2-D finite element method (FEM) (Fang et al., 1991) and 3-D discrete element method (DEM) (Moysey et al., 2004; Moysey et al., 2005; Hong et al., 2007; Moysey et al., 2008; Michelangelli et al., 2011) computational models were developed. The FEM model assumed, as does the Solid Plug model, the screw channels are completely filled by material. The FEM model essentially separates the plug into individual elements by applying a meshing scheme. The material elements in the FEM model behaved as a solid and allowed for the stresses in the material to be anisotropic. In addition, the material velocity in the FEM model is restricted to be in the down channel direction only; however, the down channel velocity was allowed to vary along the screw channel width

and depth. The FEM model should approach the Solid Plug model as the internal friction of the material elements tends toward infinity because there is no relative movement in the material in the Solid Plug model. The necessary a priori knowledge of feeder dynamics complicates the application of FEM models.

DEM models on the other hand require no such a priori understanding of the feeder dynamics because they model each individual particle. The ability of DEM simulations to model each particle eliminates the need for assumptions which simplify the feed screw conveying process. For example, in the DEM models (Moysey et al., 2004; Moysey et al., 2005; Hong et al., 2007; Moysey et al., 2008; Michelangelli et al., 2011) the screw channel fill level and the particle velocities do not have any restrictions. Additionally, the entire feeder geometry was simulated in the DEM models, whereas the FEM model (Fang et al., 1991) simplified the feeder geometry into a channel. The force models applied in DEM models, however, limit the amount of deformation of the particles. The limit on the amount of particle deformation limited the amount of feeder outlet stress which could be applied in the simulations (Moysey et al., 2004). DEM models also come at a cost of computational time.

The mass flow rate and feeder outlet stress predictions of the FEM (Fang et al., 1991) and DEM (Moysey et al., 2004; Michelangelli et al., 2011) models were compared with the predictions of Solid Plug models. The FEM model predictions were validated by experiments in which the mass flow rate and feeder outlet stress were measured. A pressure regulated die at the outlet of a feed screw allowed for adjustable outlet pressures. The pressure along the length of the barrel was also measured by a pressure transducer (Zhu et al., 1991). The DEM simulations, however, were only compared to experimental

mass flow rate measurements, not experimental feeder outlet stress measurements. The mass flow rate measurements and predictions were for a feeder with an open outlet condition. To compare outlet stress predictions of the DEM models and Solid Plug models, the outlet stress for the DEM models was varied by using the same method applied experimentally by Hyun et al. (1997a) and Gogos et al. (1994). Again the applied outlet stress was limited by the force model used. The results of the FEM and DEM models are discussed in the following paragraphs.

The FEM model (Fang et al. 1991) did a much better job at predicting the experimental mass flow rate and feeder outlet stress than the Solid Plug model developed by Darnell et al. (1956). The FEM model predicted the mass flow rate and feeder outlet stress to within 2% and 30% of the experimental results, whereas the Darnell model over-predicted the mass flow rate by 50% and the feeder outlet stress by orders of magnitude. The comparison between the Darnell model and experimental data made by Fang et al. (1991) shows a different trend than that showed by Hyun et al. (1997a). Fang et al. (1991) showed the Darnell model to over-predict experimental results, whereas Hyun et al. (1997a) showed the Darnell model to under-predict experimental results.

The mass flow rate predictions for a feeder with an open outlet condition made by the DEM models of Moysey et al. (2004) and Michelangelli et al. (2011), and the Solid Plug models developed by Tadmor et al. (1972) and Campbell et al. (1995) all predicted the experimental mass flow rate to within 10%. When applying a feeder outlet stress the DEM model developed by Moysey et al. (2004) predicted a greater mass flow rate for a given applied outlet stress than either Solid Plug model developed by Tadmor et al. (1972) or Campbell et al. (1995). The work of Hyun et al. (1997a) showed experimental results

falling between predictions of the Campbell and Tadmor models, while the DEM model predictions (Moysey et al., 2004) are larger than the Campbell and Tadmor models' predictions by approximately 20% and 70%, respectively. Unfortunately, the DEM model feeder outlet stress predictions are not validated with experimental results. The DEM model did predict the stress along the length of the feed screw to be exponential (Moysey et al., 2004) as the Solid Plug model predicts.

The DEM simulations also allowed for greater understanding of the feeder dynamics. These simulations (Moysey et al., 2004; Moysey et al., 2005; Hong et al., 2007; Moysey et al., 2008; Michelangelli et al., 2011) made it possible to measure particle velocities within a screw channel, observe the screw channel fill level, and determine the stresses acting on each of the boundary surfaces (barrel, screw core, and screw flights). The DEM models (Moysey et al., 2004; Moysey et al., 2005; Michelangelli et al., 2011) showed that the average velocities of the particles in the cross-channel and down channel directions were constant except for at the screw flights. The particles at the leading screw flight had the largest down channel velocity, while the particles at the trailing screw flight had a negative velocity. The error bars on the average particle velocities agree with the observations of Darnell et al. (1956) that the solid plug formation is an average representation of what occurs in the feeder. The constant material velocity assumption made by the Solid Plug models is therefore shown to be an average representation of the material everywhere in the screw channel except for at the screw flights.

The assumption of completely filled screw channels was shown to hold in the DEM simulations for screw speeds below 200 rpm (Moysey et al., 2004), for their screw

geometry, at which point the screw channel fill level decreased with increasing screw speeds. Typical roll compactor feed screws are run below 100 rpm, making the assumption of completely filled screw channels likely. Again, the screw channel fill level was also shown experimentally to depend on the particle size and feeder geometry (Darnell et al., 1956).

The DEM models also allowed for the stress at each of the boundaries to be measured (Moysey et al., 2004), giving further insight into the debate of whether or not the stress ratios (ratio of stress at the boundary to the down channel stress) applied in the Solid Plug models are accurate. The Solid Plug model of Hyun et al. (1997a) assumed that the stress at each boundary was equivalent. Moysey et al. (2004) calculated, from the DEM simulations, the stress at each of the boundaries. The stress at the screw root and trailing screw flight were 80% and 36%, respectively, of the stress in the down channel direction, while the stresses at the barrel and leading screw flight were almost equivalent to the down channel stress. Again, the sensitivity of the Solid Plug models to the stress ratio is discussed in Chapter 8, because of the uncertainty of the stress ratio shown in the combined works of Hyun et al (1997a), Lun (1991, kinetic theory of granular material), and Moysey et al. (2004).

Lastly, plug flow was observed to occur in the DEM simulations. Mosey et al. (2004) observed plug flow to occur immediately at the feed screw inlet for both open and restricted outlet conditions. This result differed from the DEM simulation and experimental observations made by Hong et al. (1997) and Zhu et al. (1991), who observed a solid plug to form further downstream.

From the observations made in the DEM simulations (Moysey et al., 2004; Moysey et al., 2005; Moysey et al., 2008; Michelangelli et al., 2011) the Solid Plug models' assumptions of constant material velocity, completely filled screw channels, and plug flow are plausible. However, the assumption of the stresses at the boundaries being equivalent, made in the Solid Plug models, are shown to be incorrect by the work of Moysey et al. (2008).

2.4 Feeder Torque Models

While the discussion of the models presented thus far has focused on the feeder outlet stress, the discussion in this section will focus on models, developed by Yu et al. (1997) and Dai et al. (2008, 2011), which predict the feeder torque. The models developed by Yu et al. (1997) and Dai et al. (2008) relate the feeder torque to the feeder inlet stress; whereas the current work seeks to relate the feeder torque to the feeder outlet stress. A feeder torque-outlet stress relationship is desired, because it will allow for the feeder outlet stress to be predicted by measuring the feeder torque, which is a parameter measured by some roll compactors (Gerteis, for example). The ability to predict the feeder outlet stress will allow for complete comparisons between powder roll compaction models and experimental results. Again, often in the literature the feeder outlet stress applied to powder roll compaction models is assumed or used as a fitting parameter (Katashinskii et al., 1983a; Dec et al., 2003; Bindhumadhavan et al., 2005; Muliadi et al., 2012;). A feeder torque-outlet stress relationship will also allow for real time process controls. Discussed below are the feeder torque models of Yu et al. (1997) and Dai et al. (2008).

Both of the feeder torque models (Yu et al., 1997; Dai et al., 2008) assume the material in the feed screw completely fills the screw flights, has reached a steady state, and can be treated as a continuum. Let it be pointed out that these assumptions are also made by the Solid Plug models. The feeder torque model developed by Dai et al. (2008) differs from that developed by Yu et al. (1997) by accounting for the material compressibility. The material compressibility is accounted for in the feeder torque model developed by Dai et al. (2008) by applying a compression factor (CF), which is related to the material compressibility and is chosen to minimize the average deviation between the predicted and experimental torques. The work of Dai et al. (2008) accounts for the material compressibility because in Dai et al's. work the feeder torque model is applied to feed screws that convey materials with varying degrees of compressibility. The feeder torque model derivation of Yu et al. (1997) is outlined in the following paragraphs. The point at which the compression factor is applied in the feeder torque model developed by Dai et al. (2008) is highlighted below as well.

The feeder torque model developed by Yu et al. (1997) assumes constant material parameters and feeder geometry along the length of the feed screw. The model first applies a force balance on a differential material element of length dx (Figure 2.8).

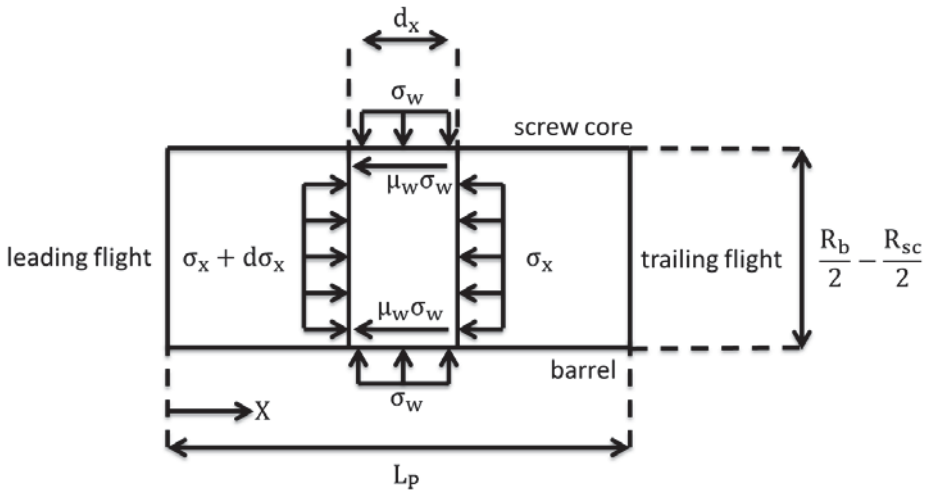

Figure 2.82. Free body diagram of a differential material element of length dx in a feed screw.

Assuming that the stress at the trailing flight is equal to the inlet stress,

$$\sigma_x = \sigma_0, \tag{2.24}$$

at x = L_P, where σ_0 is the feeder inlet stress, σ_x is the axial stress, and L_P is the pitch length, the axial stress can be related to the feeder inlet stress by,

$$\sigma_x = \sigma_0 \mathrm{Exp}\left(\frac{2\mu_w\lambda}{R_b - R_{sc}}(L_P - x)\right), \tag{2.25}$$

where λ is the ratio of the wall stress to axial stress (σ_w/σ_x), μ_w is the wall friction coefficient, R_b is the barrel radius, and R_{sc} is the screw core radius. It is at this point where the feeder torque model developed by Dai et al. (2008) applies the compression factor (CF). The relationship between the axial stress and feeder inlet stress given by Equation (2.25) is similar to the relationship given by Dai et al. (2008), the only difference is the relationship given by Dai et al. (2008) multiplies the right hand side of Equation (2.25) by the compression factor,

$$\sigma_x = CF^*\sigma_0 Exp\left(\frac{2\mu_w\lambda}{R_b\text{-}R_{sc}}(L_P - x)\right). \quad (2.26)$$

To derive the feeder torque models developed by Yu et al. (1997) or Dai et al. (2008), the remainder of the derivation can be carried out with the respective definitions of the axial stress (Equation (2.25) or Equation (2.26)). From this point forward the axial stress defined by Yu et al. (1997) (Equation (2.25)) is applied.

Next, the feeder torque model applies an axial force balance on the bulk material in the screw channel, setting the axial conveying force due to the leading screw flight (F_{lf_a}) equal to the axial retarding forces due to the barrel (F_{b_a}), screw core (F_{sc_a}), and trailing screw flight (F_{tf_a}),

$$F_{lf\_a} = F_{b\_a} + F_{sc\_a} + F_{tf\_a} \quad (2.27)$$

The axial forces at the barrel, screw core, and trailing screw flight surfaces are defined in terms of the stresses at the surfaces and the areas over which the stresses act,

$$F_{b\_a} = c_b\sigma_{wa}, \quad (2.28)$$

$$F_{sc\_a} = c_{sc}\sigma_{wa}, \quad (2.29)$$

and,

$$F_{tf\_a} = c_{tf}\sigma_x \quad (2.30)$$

The parameters c_b, c_{sc}, and c_{tf} depend on the feeder geometry and friction coefficients. To simplify calculations the forces at the barrel and screw core surfaces are defined in terms of the average wall stress (σ_{wa}),

$$\sigma_{wa} = \frac{\lambda}{L_P}\int_0^{L_P}\sigma_x dx \quad (2.31)$$

The average wall stress can be given in terms of the feeder inlet stress by substituting Equation (2.25) into Equation (2.31),

$$\sigma_{wa} = \frac{\lambda}{L_P}\int_0^{L_P} \sigma_0 \mathrm{Exp}\left(\frac{2\mu_w\lambda}{R_b\text{-}R_{sc}}(L_P - x)\right). \tag{2.32}$$

To determine the axial force at the leading screw flight in terms of the feeder inlet stress, first substitute Equations (2.28-2.30) into Equation (2.27) to get the axial force at the leading screw flight in terms of the feeder geometry, friction coefficients, average wall stress, and axial stress,

$$F_{lf\_a} = c_b\sigma_{wa} + c_{sc}\sigma_{wa} + c_{tf}\sigma_x \tag{2.33}$$

Next, the axial force at the leading screw flight can be further simplified by substituting Equations (2.25) and (2.31) into Equation (2.33),

$$F_{lf\_a} = \left(\tilde{c}_b + \tilde{c}_{sc} + \tilde{c}_{tf}\right)\sigma_0, \tag{2.34}$$

where $\tilde{c}_b$, $\tilde{c}_{sc}$, and $\tilde{c}_{tf}$ depend on the feeder geometry, friction coefficients, and the ratio σ_w/σ_x.

By breaking down the force at the leading screw flight into its axial and tangential components (Figure 2.9), the tangential force at the leading screw flight (F_{lf_t}) can be given in terms of the axial force,

$$F_{lf\_t} = F_{lf\_a} * \tan(\phi_r + \Psi_f), \tag{2.35}$$

where ϕ_r is the helical angle at radius r and ψ_f is the screw flight friction angle.

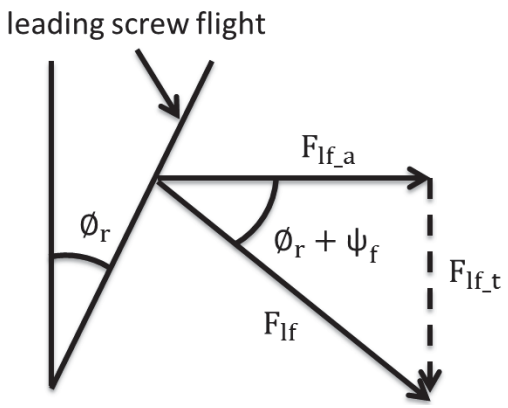

Figure 2.93. Diagram showing the relationship between the axial and tangential components of the force on the leading screw flight.

Substituting Equation (2.34) into Equation (2.35) gives the tangential force at the leading screw flight in terms of the feeder inlet stress,

$$F_{lf\_t} = (\tilde{c}_b + \tilde{c}_{sc} + \tilde{c}_{tf})\sigma_0 * \tan(\phi_r + \Psi_f)\,. \tag{2.36}$$

Lastly, integrating the tangential force over the entire leading screw flight to get the total tangential force at the leading screw flight acting on the bulk material, and determining the torque due to the tangential force gives,

$$T = \sigma_0 \int_0^{2\pi} \int_{R_{sc}}^{R_b} (\tilde{c}_b + \tilde{c}_{sc} + \tilde{c}_{tf}) * \tan(\phi_r + \Psi_f)\, r^2\, dr d\theta\,, \tag{2.37}$$

where T is the torque on the leading screw flight. The torque on the leading screw flight (Equation (2.37)) equals the torque due to a single screw channel. From Equation (2.37) the torque due to a single screw channel is shown to be proportional to the feeder inlet stress.

The total feeder torque then equals the summation of the torques due to each screw channel. The feeder torque models assume that $\sigma_x = \sigma_0$ at $x = L_P$ holds for every screw channel along the length of the feed screw. Assuming $\sigma_x = \sigma_0$ at $x = L_P$ for every

screw channel means that the stress at the leading screw flight is independent of the axial position along the feed screw of the leading screw flight, as long as the material properties and feeder geometry are assumed constant as well. With these assumptions the torque due to each screw channel is equivalent. The total feeder torque then equals the torque due to a single screw channel multiplied by the number of screw channels,

$$T_{total} = n * T, \tag{2.38}$$

where n is the total number of screw channels and T_{total} is the total feeder torque.

The theoretical work of both Yu et al. (1997) and Dai et al. (2008) predicted the feeder torque for different materials (Semolina, Cement, wood pellets, and polyethylene particles) and feeder geometries to within 10% of experimental results. These feeder torque models, however, are only applied to feeders with open outlet conditions, which allows for the assumption that the stress does not increase moving downstream (i.e., $\sigma_x = \sigma_0$ at $x = L_P$ holds for every screw channel along the length of the feed screw).

The current work seeks to relate the feeder torque to the feeder outlet stress in cases where the stress builds along the axial length of the feeder. When the stress increases along the length of the feeder, the axial force at each leading screw flight will vary, causing the torque due to each screw channel to be different. In Chapter 4 a relationship between the feeder torque and the feeder outlet stress is derived by combining the feeder torque model and Solid Plug model. Applying the Solid Plug model to the feeder torque model allows for the feeder stress to be dependent on the axial location. Again, both the feeder torque model and Solid Plug model assume the material in the feed screw completely fills the screw flights, has reached a steady state, and can be treated as a continuum. The feeder torque model and Solid Plug model are also similar in

that they both apply force balances to differential material elements, as evidenced by Equation (2.25) being similar to the output of the Solid Plug model.

2.5 Model Summaries

In this chapter, 1-D analytical and higher order powder roll compaction models found in literature were reviewed. All of the parameters predicted by the powder roll compaction models, except for the nip angle, were shown to depend on the stress at the inlet of the nip region in a roll compactor. While the powder roll compaction models were shown to predict the nip angle well, the powder roll compaction models' ability to predict the roll force, roll torque, maximum roll force, and ribbon density, however, was inconclusive because of the inability to specify the stress at the inlet of the nip region. Often in the literature, the stress at the inlet of the nip region is unknown and therefore assumed or applied as a fitting parameter. The inability to specify the stress at the inlet of the nip region in a roll compactor makes it difficult to evaluate the powder roll compaction models.

Also discussed in this chapter were feeder models. One of which was the 1-D analytical Solid Plug model. The Solid Plug model, which relates the feeder outlet stress to the mass flow rate, has been evaluated in the literature for plastic extrusion with varying degrees of success. The Solid Plug model's predictions have been shown to vary from experimental results by a few percent to orders of magnitude. While there are few experimental trials validating the Solid Plug models predictions, most of the literature work has focused on validating the Solid Plug model's assumptions. In the literature, the

following Solid Plug model assumptions have been shown, through experimental observations and DEM results, to be reasonable.

1. The material between the flights of the feed screw is treated as a continuum (i.e., a solid plug).
2. The material completely fills the screw channel making contact with all boundary surfaces.
3. The material only moves in the down channel direction, and as the material moves axially along the screw, the velocity in the down channel direction is constant.

The Solid Plug model also assumes the stresses at the barrel, screw core, and screw flights are equivalent. However, DEM results have shown the stresses measured at each of the boundaries to be different.

The last models discussed in this chapter were feeder torque models. By assuming that the stress along the length of a feed screw is constant, the feeder torque models are able to derive a relationship between the feeder inlet stress and feeder torque. In order for this assumption to hold, the theory is only applied to feed screws with no applied outlet stress (i.e., open outlet condition). The feeder torque models have been shown to predict experimental results to within 10% for various feeder geometries and conveying materials, however all for open outlet feeders.

CHAPTER 3. OBJECTIVES

With the aim of improving the powder roll compaction models by accounting for the deficiencies described in the previous section, the following objectives are the focus for this thesis:

1. Develop a feed screw model (reduced order) to predict the stress at the outlet of the powder feed screw of a roll compactor, which is the inlet stress to the rolls.
2. Develop and perform experiments to validate the feed screw open-exit mass flow rate and outlet stress predictions.
3. Determine a relationship between the feeder torque and feeder outlet stress.

CHAPTER 4. SOLID PLUG MODEL

A derivation of the Solid Plug model developed by Tadmor et al. (1972) is provided here along with the formulation differences of the Solid Plug models developed by Campbell et al. (1995) and Hyun et al. (1997a). The Solid Plug models developed by Tadmor et al. (1972), Campbell et al. (1995), and Hyun et al. (1997a) are discussed because they will be compared to the experimental results presented in Chapter 7. The reason for comparing these three Solid Plug models to the experimental results is that these models have been compared to the experimental results found in the literature (Fang et al., 1991; Hyun et al., 1997a). Therefore, allowing the trends found in the current work to be compared to the trends found in the literature. Lastly, the Solid Plug model derivation will be expanded, beyond what has been done in the literature, to relate the feeder outlet stress to the feeder torque. The Solid Plug models developed in the literature derive a relationship between the mass flow rate and feeder outlet stress, whereas in Section 4.2 the Solid Plug model is applied to the feeder torque model, developed by Yu et al. (1997), in order to derive a feeder torque-outlet stress relationship. Again, a feeder torque-outlet stress relationship is desired because the feeder torque is an output given by some roll compactors and can be more easily measured on a roll compactor than the feeder outlet stress. Thus, measuring the feeder torque and attaining

a feeder torque-outlet stress relationship will allow for predictions of the feeder outlet stress.

4.1 Solid Plug Model Derivation

The Solid Plug model developed by Tadmor et al. (1972) assumes the following:

- The material in the screw channel is a continuum.
- The material completely fills the screw channel and contacts all boundaries (screw flights, screw core, and barrel).
- The material only moves in the down channel direction, and as the material moves axially along the screw, the velocity in the down channel direction is constant.
- The material density is constant along the length of the screw.
- Gravitational and centrifugal forces are negligible.
- The frame of reference is with the solid plug so that the barrel appears to move and the screw remains stationary.

The notation applied throughout the Solid Plug model derivation below is presented in Figure 4.1.

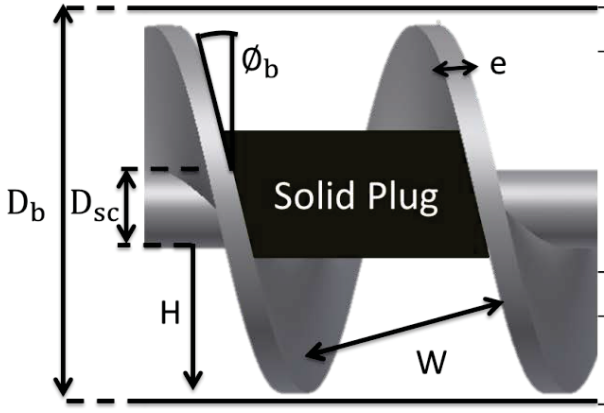

Notation	Parameter
D	diameter
e	screw flight thickness
H	channel height
W	channel width
ø	helical angle
Subscript	**Parameter**
b	barrel
sc	screw core

Figure 4.1. Geometry of a screw channel.

The normal and frictional forces acting upon a differential material element within a screw channel due to the following boundaries: screw core (dF_{sc}), leading screw flight (dF_{lf_μ}, dF_{lf}, dF^*), trailing screw flight (dF_{tf_μ}, dF_{tf}), barrel surface (dF_b), and surrounding material (dF_{ds}, dF_{us}) are shown in Figure 4.2. In order to apply the axial force and torque balances, the forces are now broken down into their axial and tangential components and defined in terms of the down channel stress and area over which the forces act.

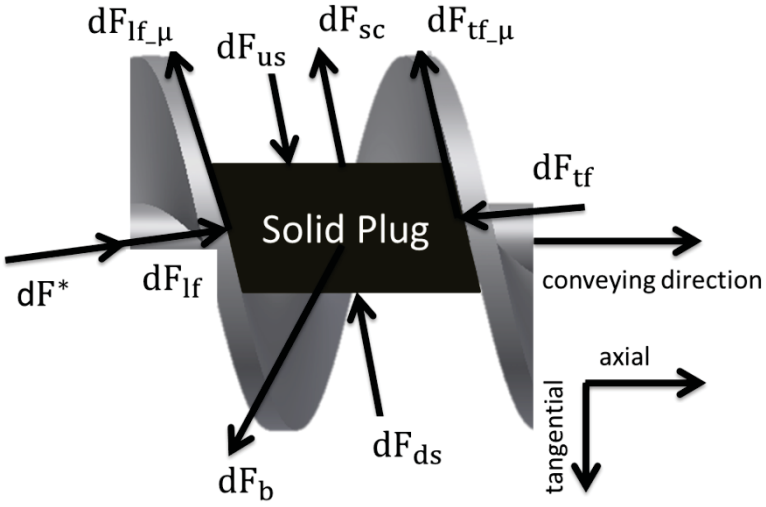

Figure 4.2. Forces acting upon a material element within a screw channel (Tadmore et al., 1972).

The derivation below applies two stress ratios k_t and k_r, which relate the stresses at the screw flights (σ_t) and the stresses at the barrel and screw core surfaces (σ_r), respectively, to the stress in the down channel direction (σ). By assuming that the stress in the down channel direction is the major principal stress, the stresses at the screw flights and at the barrel and screw core surfaces are minor principal stresses because they act orthogonal to the down channel stress, although technically the surfaces on which

principal stresses act have no shear stress (Figure 2.2). The minor principal stresses can be related to the major principal stress by (Figure 4.3),

$$\sigma_t = k_t \sigma , \tag{4.1}$$

and,

$$\sigma_r = k_r \sigma \tag{4.2}$$

The approach applied here to relate the principal stresses is similar to the approach of Janssen (Janssen, 1895).

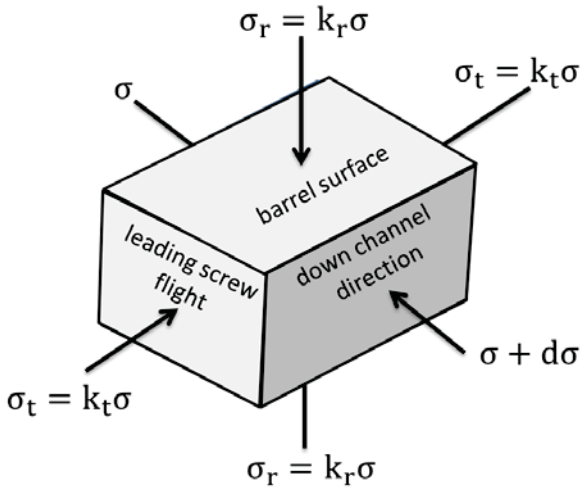

Figure 4.3. Diagram showing the relationships between the stresses acting on a material element in a screw channel.

The friction force between the material and barrel surface (dF_b) is the driving force which conveys the material downstream. The frictional force due to the barrel is,

$$dF_b = \frac{\mu_b W_b dL}{\sin(\phi_b)} k_r \sigma , \tag{4.3}$$

where μ_b is the barrel friction coefficient, W_b is the channel width at the barrel, $\frac{dL}{\sin(\phi_b)}$ is the differential down channel distance at the barrel surface, dL is the axial distance along

the feeder, and $\emptyset_b$ is the helical angle at the barrel surface. The axial and tangential components of dF_b are,

$$dF_{b\_a} = \frac{\mu_b W_b \sin(\alpha) dL}{\sin(\phi_b)} k_r \sigma, \tag{4.4}$$

and,

$$dF_{b\_t} = \frac{\mu_b W_b \cos(\alpha) dL}{\sin(\phi_b)} k_r \sigma, \tag{4.5}$$

respectively. The direction at which the force due to the barrel friction acts (Figure 4.4), known as the conveying angle (α), is discussed below.

The normal forces that the leading and trailing screw flights exert on the material element differ by the unknown normal force (dF^*) at the leading screw flight. The unknown force at the leading screw flight is applied to balance the forces on the material element. The normal forces dF_{lf} and dF_{tf} are equivalent and are given by,

$$dF_{lf} = dF_{tf} = \frac{HdL}{\sin(\bar{\phi})} k_t \sigma, \tag{4.6}$$

where H is the screw channel height, $\frac{dL}{\sin(\bar{\emptyset})}$ is the average differential down channel distance, and $\bar{\emptyset}$ is the average helical angle. To simplify the calculations the forces which act on the screw flights are assumed to act evenly over the screw channel depth. For this reason, the average helical angle is taken.

The frictional forces due to the leading and trailing screw flights are,

$$dF_{lf\_\mu} = \mu_s \left(dF_{lf} + dF^* \right), \tag{4.7}$$

and,

$$dF_{tf\_\mu} = \mu_s dF_{tf}, \tag{4.8}$$

respectively, where μ_s is the feed screw friction coefficient.

The last frictional force acting upon the material element is due to the screw core,

$$dF_{sc} = \frac{\mu_s W_{sc} dL}{\sin(\phi_{sc})} k_r \sigma, \tag{4.9}$$

where W_{sc} is the screw channel width at the screw core, $\frac{dL}{\sin(\emptyset_{sc})}$ is the differential down channel distance at the screw core surface, and $\emptyset_{sc}$ is the helical angle at the screw core.

Finally, the coupled forces dF_{ds} and dF_{us} are the forces on the differential material element due to the surrounding material downstream and upstream, respectively. These forces are,

$$dF_{ds} = H\bar{W}(\sigma + d\sigma), \tag{4.10}$$

and,

$$dF_{us} = H\bar{W}\sigma, \tag{4.11}$$

where the stress variation in the down channel direction across the material element is captured by the difference between the forces. To simplify the calculations of the forces due to the surrounding material, they are assumed to act evenly across the screw channel width; therefore the area over which the forces due to the surrounding material act are in terms of the average screw channel width ($\bar{W}$).

The axial and tangential components of forces acting parallel to the screw flights, (dF_{sc}, dF_{lf_μ}, dF_{tl_μ}, dF_{us}, and dF_{ds}), can be obtained by multiplying the forces by $\sin(\emptyset)$ or $\cos(\emptyset)$, respectively, (Figure 4.4) while the axial and tangential components of the forces acting perpendicular to the screw flights, (dF_{lf}, dF_{tf}, and dF^*), can be attained

by multiplying the forces by $\cos(\emptyset)$ or $\sin(\emptyset)$, respectively (Figure 4.4), where $\emptyset$ is the helical angle defined by the location at which the force acts (i.e., the screw core ($\emptyset_{sc}$), barrel ($\emptyset_b$), or averaged over the screw flight ($\overline{\emptyset}$)).

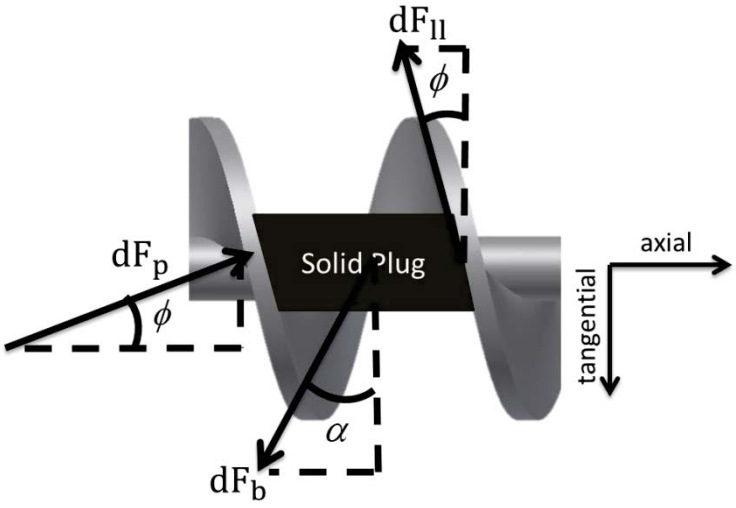

Figure 4.4. Schematic giving the relationship between forces acting on the material element in a feed screw channel and the angles at which they act. The parameter dF_{ll} represents the forces parallel to the screw flights, dF_p represents the forces perpendicular to the screw flight, and dF_b is the force due to the barrel.

The force balance is then completed by summing the forces in the axial direction,

$$\begin{aligned}&-dF_b\sin(\alpha)-dF_{sc}\sin(\phi_{sc})-dF_{lf\_\mu}\sin(\overline{\phi})-dF_{tf\_\mu}\sin(\overline{\phi})-dF_{ds}\sin(\overline{\phi})\\&+dF_{us}\sin(\overline{\phi})+dF_{lf}\cos(\overline{\phi})-dF_{tf}\cos(\overline{\phi})+dF^{*}\cos(\overline{\phi})=0\end{aligned}, \tag{4.12}$$

and the torque balance is similarly completed by multiplying each tangential force by the appropriate moment arm and then summing the torques,

$$\begin{aligned}&-\frac{D_b}{2}dF_b\cos(\alpha)+\frac{D_{sc}}{2}dF_{sc}\cos(\phi_{sc})+\frac{\overline{D}}{2}dF_{lf\_\mu}\cos(\overline{\phi})+\frac{\overline{D}}{2}dF_{tf\_\mu}\cos(\overline{\phi})+\frac{\overline{D}}{2}dF_{ds}\cos(\overline{\phi})\\&-\frac{\overline{D}}{2}dF_{us}\cos(\overline{\phi})+\frac{\overline{D}}{2}dF_{lf}\sin(\overline{\phi})-\frac{\overline{D}}{2}dF_{tf}\sin(\overline{\phi})+\frac{\overline{D}}{2}dF^{*}\sin(\overline{\phi})=0\end{aligned}, \tag{4.13}$$

where $D_{sc}/2$, $D_b/2$, and $\overline{D}/2$ are the moment arms for the forces acting at the screw core, barrel, and average channel height, respectively. The forces that act over the screw

channel height, (dF_{lf_μ}, dF_{lf}, dF^*, dF_{tf}, and dF_{tf_μ}), are assumed to act uniformly; therefore, the equivalent point loads act at the average channel height ($\bar{D}/2$).

Noting that the forces due to the leading and trailing screw flights are equivalent, ($dF_{lf} = dF_{tf}$), and that the forces due to the surrounding material only differ by $d\sigma$, ($dF_{ds} - dF_{us} = d\sigma$), Equations (4.12) and (4.13) can be simplified to,

$$\begin{aligned} &-dF_b\sin(\alpha) - dF_{sc}\sin(\phi_{sc}) - dF_{lf\_\mu}\sin(\bar{\phi}) \\ &-dF_{tf\_\mu}\sin(\bar{\phi}) - d\sigma H\bar{W}\sin(\bar{\phi}) + dF^*\cos(\bar{\phi}) = 0 \end{aligned}, \tag{4.14}$$

and,

$$\begin{aligned} &-\frac{D_b}{2}dF_b\cos(\alpha) + \frac{D_{sc}}{2}dF_{sc}\cos(\phi_{sc}) + \frac{\bar{D}}{2}dF_{lf\_\mu}\cos(\bar{\phi}) \\ &+\frac{\bar{D}}{2}dF_{tf\_\mu}\cos(\bar{\phi}) + \frac{\bar{D}}{2}d\sigma H\bar{W}\cos(\bar{\phi}) + \frac{\bar{D}}{2}dF^*\sin(\bar{\phi}) = 0 \end{aligned}. \tag{4.15}$$

Substituting Equations (4.7) and (4.8) into both Equations (4.14) and (4.15),

$$\begin{aligned} &-dF_b\sin(\alpha) - dF_{sc}\sin(\phi_{sc}) - \mu_s\left(dF_{lf} + dF^*\right)\sin(\bar{\phi}) \\ &-\mu_s dF_{tf}\sin(\bar{\phi}) - d\sigma H\bar{W}\sin(\bar{\phi}) + dF^*\cos(\bar{\phi}) = 0 \end{aligned}, \tag{4.16}$$

and,

$$\begin{aligned} &-\frac{D_b}{2}dF_b\cos(\alpha) + \frac{D_{sc}}{2}dF_{sc}\cos(\phi_{sc}) + \frac{\bar{D}}{2}\mu_s\left(dF_{lf} + dF^*\right)\cos(\bar{\phi}) \\ &+\frac{\bar{D}}{2}\mu_s dF_{tf}\cos(\bar{\phi}) + \frac{\bar{D}}{2}d\sigma H\bar{W}\cos(\bar{\phi}) + \frac{\bar{D}}{2}dF^*\sin(\bar{\phi}) = 0 \end{aligned}. \tag{4.17}$$

Given Equations (4.16) and (4.17), one can then solve for the unknown force at the leading screw flight, again noting that the forces at leading and trailing screw flights are equivalent,

$$dF^* = \frac{1}{\cos(\bar{\phi}) - \mu_s\sin(\bar{\phi})}\left[-dF_b\sin(\alpha) - dF_{sc}\sin(\phi_{sc}) - 2\mu_s dF_{lf}\sin(\bar{\phi}) - d\sigma H\bar{W}\sin(\bar{\phi})\right], \tag{4.18}$$

and,

$$dF^{*} = \frac{1}{\sin\left(\bar{\phi}\right)+\mu_s\cos\left(\bar{\phi}\right)}\left[\frac{D_b}{\bar{D}}dF_b\cos\left(\alpha\right)-\frac{D_{sc}}{\bar{D}}dF_{sc}\cos\left(\phi_{sc}\right)-2\mu_s dF_{lf}\cos\left(\bar{\phi}\right)-d\sigma H\bar{W}\cos\left(\bar{\phi}\right)\right] \quad (4.19)$$

Finally substituting Equations (4.3 – 4.11) into Equations (4.18) and (4.19), then setting Equation (4.18) equal to (4.19) results in the following differential equation,

$$d\sigma = \frac{(KB_1 - A_1)}{(KB_2 + A_2)}\sigma dL, \quad (4.20)$$

where $K, A_1, A_2, B_1,$ and B_2 are defined as,

$$K = \frac{1-\mu_s\tan\left(\bar{\phi}\right)}{\tan\left(\bar{\phi}\right)+\mu_s}, \quad (4.21)$$

$$A_1 = \frac{\mu_b W_b \sin\left(\alpha\right)}{\sin\left(\phi_b\right)}k_r + \mu_s W_{sc} k_r + 2\mu_s H k_t, \quad (4.22)$$

$$A_2 = H\bar{W}\sin\left(\bar{\phi}\right), \quad (4.23)$$

$$B_1 = \frac{D_b\mu_b W_b\cos\left(\alpha\right)}{\bar{D}\sin\left(\phi_b\right)}k_r - \frac{D_{sc}\mu_s W_{sc}\cot\left(\phi_{sc}\right)}{\bar{D}}k_r - 2\mu_{sc}H\cot\left(\bar{\phi}\right)k_t, \quad (4.24)$$

and,

$$B_2 = H\bar{W}\cos\left(\bar{\phi}\right) \quad (4.25)$$

Assuming that the feeder geometry, friction coefficients, material density, and feeder inlet stress (σ_0) are constants, and that the material is isotropic ($k_t = k_r = 1$), as Tadmor et al. (1972) does, Equation (4.20) is then solved to derive the final result of the Solid Plug model,

$$\sigma = \sigma_o \mathrm{Exp}\left[\frac{(KB_1 - A_1)}{(KB_2 + A_2)}L\right], \quad (4.26)$$

where L is the axial downstream distance along the feeder axis, and σ is the stress. From the Solid Plug model (Equation (4.26)), the feeder stress depends on the feeder geometry, material-barrel friction coefficient, material-feed screw friction coefficient, conveying angle, and feeder inlet stress.

Conveying Angle

The conveying angle is the angle at which the barrel frictional force (the conveying force) acts, the angle at which the barrel moves relative to the material, and the angle that relates the material velocity in the screw channel direction to the material velocity in the axial direction. The conveying angle, which was shown to be a necessary input for the Solid Plug model (Equation (4.20)), is difficult to measure experimentally. However, the conveying angle can be related to the mass flow rate by the following equation (Tadmor et al., 1972),

$$\dot{M} = \rho(\sigma)\pi D_b V_s \left(\frac{\tan(\alpha)\tan(\phi_b)}{\tan(\alpha)+\tan(\phi_b)} \right) \left(\pi H(H+D_{sc}) - \frac{peH}{\sin(\bar{\phi})} \right) \tag{4.27}$$

Simply put, the mass flow rate (Equation (4.27)) is the product of the material density, which is a function of the local stress, screw channel cross-sectional area, and axial velocity of the material. The full derivation of Equation (4.27) is provided in Appendix A. In order to implement the Solid Plug model, the above equation is solved for the conveying angle, which is then input into Equation (4.20). The Solid Plug model then depends on the feeder geometry, material-barrel friction coefficient, material-feed screw friction coefficient, feeder inlet stress, mass flow rate, feed screw speed, and material density.

Additionally, the stress-density relationship that will be discussed in Chapter 9 is applied to Equation (4.27). The application of the stress-density relationship to the Solid Plug model discussed here is also shown in a flow chart in Figure 4.5. The stress-density relationship is applied by first inputting the feeder inlet stress into the stress-density relationship to determine the inlet density. Next, the inlet density is input into Equation (4.27) along with the other parameters to determine the conveying angle. The conveying angle is then input into the Solid Plug model (Equation (4.20)), which is applied some distance downstream to determine the feeder stress downstream. Lastly, the calculated downstream feeder stress is input back into the stress-density relationship to determine the density downstream. This process continues until the feeder outlet is reached (Figure 4.5). Assuming then that the feeder geometry, material-barrel friction coefficient, material-feed screw friction coefficient, feeder inlet stress, and feed screw speed are constant, the feeder outlet stress is then a function of the mass flow rate, and material density.

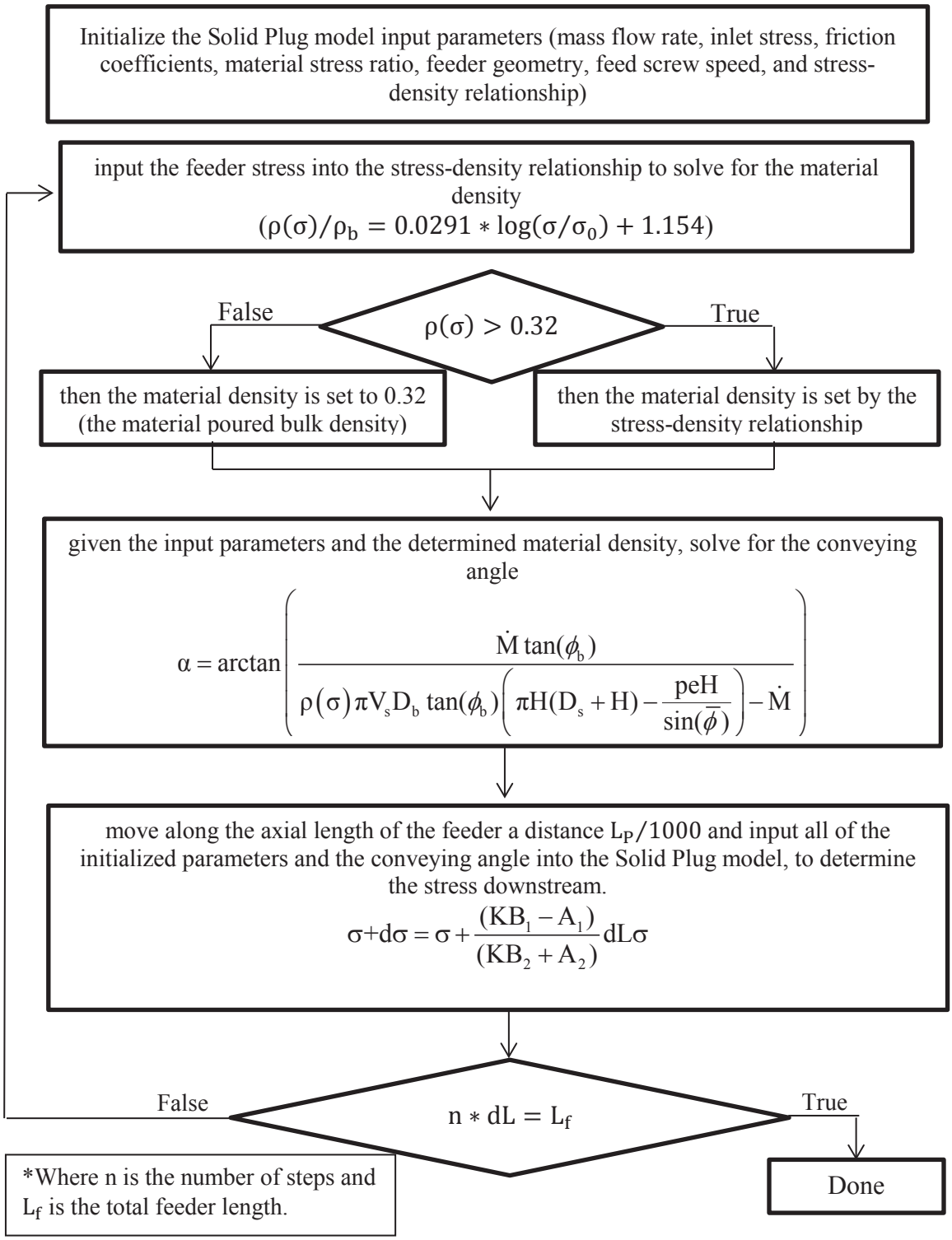

Figure 4.5. Algorithm used to implement the stress-density relationship into the Solid Plug model.

4.1.1 Variations between Solid Plug Models

The differences between the Solid Plug models developed by Tadmor et al. (1972), Campbell et al. (1995), and Hyun et al. (1997a) were previously discussed in Chapter 2. In this section the differences in their final derivations are shown (Table 4.1). Again, the primary differences between the three Solid Plug models are that: (1) the Tadmor and Hyun models treat the material in the feed screw as a solid, whereas the Campbell model treats the material as a fluid, (2) each model has varying assumptions and applications of the unknown force at the leading screw flight, and (3) Hyun et al. (1997a) assumes the stresses in the material are anisotropic and applies a stress ratio ($k = k_t = k_r \neq 1$), while Tadmor et al. (1972) and Campbell et al. (1995) assume the stresses in the material to be isotropic ($k_t = k_r = 1$). Although the Tadmor and Hyun models differ, the derivation steps are exactly the same; in fact, the Tadmor and Hyun models are identical if in the Hyun model the unknown force at the leading screw flight is applied perpendicular to the screw flight and the stress ratio is set equal to one. Applying the unknown force at an angle (Hyun model) results in an additional friction force at the leading screw flight ($dF_\mu{}^*$) which changes the parameter K between the Tadmor and Hyun models in Table 4.1.

Table 4.1. Variations between the Solid Plug models developed by Tadmor et al. (1972), Campbell et al. (1995), and Hyun et al. (1997a).

Tadmor et al. (1972)

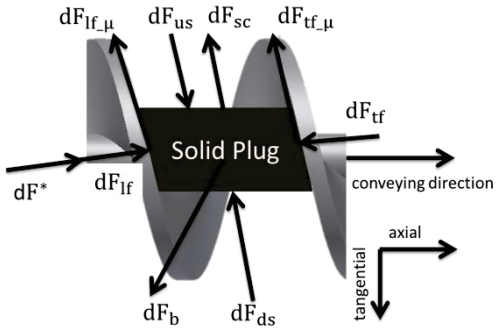

Result

$$\sigma = \sigma_0 \mathrm{Exp}\left[\frac{(KB_1 - A_1)}{(KB_2 + A_2)} L\right]$$

Parameters

$$K = \frac{1 - \mu_s \tan(\bar{\phi})}{\tan(\bar{\phi}) + \mu_s}$$

$$A_1 = \frac{\mu_b W_b \sin(\alpha)}{\sin(\phi_b)} k_r + \mu_s W_{sc} k_r + 2\mu_s H k_t \qquad A_2 = H\bar{W}\sin(\bar{\phi})$$

$$B_1 = \frac{D_b \mu_b W_b \cos(\alpha)}{\bar{D}\sin(\phi_b)} k_r - \frac{D_{sc} \mu_s W_{sc} \cot(\phi_{sc})}{\bar{D}} k_r - 2\mu_s H \cot(\bar{\phi}) k_t \qquad B_2 = H\bar{W}\cos(\bar{\phi})$$

Table 4.1. Continued.

Campbell et al. (1995)

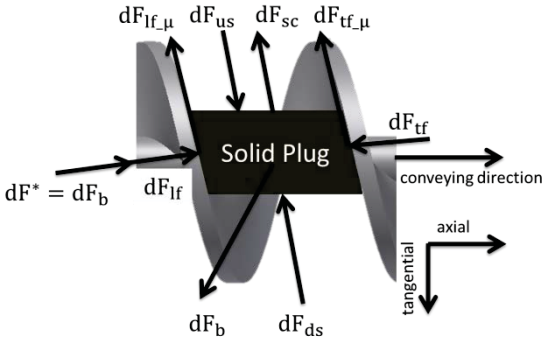

Result

$$\sigma = \sigma_0 * \mathrm{Exp}\left\{\frac{L}{A_2}\left[-A_1 + \mu_b W_b \cot(\phi_b) k_r - \mu_s \mu_b W_b k_r\right]\right\}$$

Parameters

$$A_1 = \frac{\mu_b W_b \sin(\alpha)}{\sin(\phi_b)} k_r + \mu_s W_{sc} k_r + 2\mu_s H k_t \qquad A_2 = H \bar{W} \sin(\bar{\phi})$$

Table 4.1. Continued.

Hyun et al. (1997a)

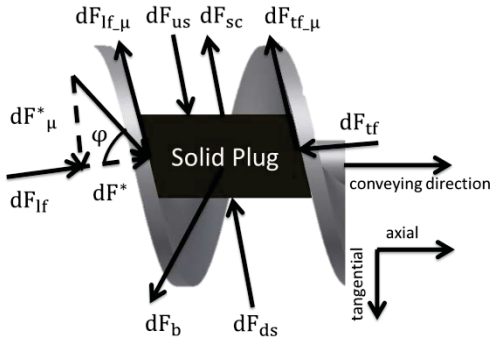

Result

$$\sigma = \sigma_0 \mathrm{Exp}\left[\frac{(KB_1 - A_1)}{(KB_2 + A_2)}L\right]$$

Parameters

$$K = \cot(\bar{\phi})$$

$$A_1 = \frac{\mu_b W_b \sin(\alpha)}{\sin(\phi_b)} k_r + \mu_s W_{sc} k_r + 2\mu_s H k_t \qquad A_2 = H\bar{W}\sin(\bar{\phi})$$

$$B_1 = \frac{D_b \mu_b W_b \cos(\alpha)}{\bar{D}\sin(\phi_b)} k_r - \frac{D_{sc}\mu_s W_{sc}\cot(\phi_s)}{\bar{D}} k_r - 2\mu_s H\cot(\bar{\phi})k_t \qquad B_2 = H\bar{W}\cos(\bar{\phi})$$

4.1.2 Model Behavior

After understanding the derivation of the Solid Plug model, a discussion of how the model behaves is presented here. From this point onward, the feeder outlet stress will be discussed as a function of mass flow rate instead of the conveying angle. While the conveying angle is used for the derivation of the feeder stress, mass flow rate is more intuitive and a more easily measured parameter.

According to the Solid Plug model there are two mechanisms by which the material in a feed screw is conveyed: (1) the difference between the feed screw and barrel

frictional forces, and (2) the feeder inlet-outlet axial stress differential. The barrel frictional force and feeder inlet stress convey material downstream whereas the friction due to the feed screw and the feeder outlet stress retard the motion of the material downstream. Increasing the conveying forces or decreasing the retarding force due to the friction of the feed screw increases the feeder outlet stress for a given mass flow rate. Assuming the frictional forces and feeder inlet stress are constant, a maximum mass flow rate results in a predicted feeder outlet stress of zero, while when the mass flow rate is zero the feeder outlet stress reaches its maximum. The trends shown while discussing the results are explained by these Solid Plug model behaviors.

The effect of varying the applied stress ratio is also investigated. A larger stress ratio means a greater stress is applied at the boundaries (barrel, screw core, and screw flights). The stress ratio affects the Solid Plug model feeder outlet stress predictions greatly because the stress ratio directly multiplies the exponent of the exponential in the Solid Plug model (Table 4.1, Hyun model). When the conveying force is greater than the retarding force, the exponent of the exponential is negative and a lower stress ratio results in a higher outlet stress for a given mass flow rate. The increased feeder outlet stress for the same mass flow rate is a result of decreasing the exponent of a negative exponential.

4.2 Expanding the Solid Plug Model into a Feeder Torque-Outlet Stress Relationship

The Solid Plug model is of particular interest to the work in this thesis not only because the Solid Plug model predicts the feeder outlet stress, but all of the Solid Plug models, except for the Solid Plug model developed by Campbell et al. (1995), also incorporate a torque balance. The torque balance applied in the Solid Plug models relates

the torques acting on the material in a feed screw due to the barrel, screw core, and screw flights to the feed screw axial stress. These relationships present the opportunity to expand the Solid Plug model derivation to a feeder torque-outlet stress relationship. A relationship between the feed screw torque and feeder outlet stress has not previously been derived in the literature using the Solid Plug model. The Solid Plug models presented in the literature derive a relationship between the mass flow rate and feeder outlet stress. The application of the Solid Plug model to the theory presented by Yu et al. (1997) on modeling feeder torque, which is discussed below, is where the current work differs from the Solid Plug models presented in the literature.

Provided a feeder torque-outlet stress relationship and measuring the feed screw torque, which is an output given by some roll compactors, allows for the feeder outlet stress (i.e., roll inlet stress) to be predicted. Again, the feeder outlet stress is a necessary input parameter in existing powder roll compaction models. While the feeder torque model developed by Yu et al. (1997) relates the feed screw torque to the feeder inlet stress, in the derivation that follows, the feed screw torque is related to the feeder outlet stress by applying the Solid Plug model developed by Tadmor et al. (1972) to the theory presented by Yu et al. (1997) on modeling feeder torque. Applying the Solid Plug model to the feeder torque model allows for the stress along the length of a feed screw to have an axial dependence, whereas the feeder torque model developed by Yu et al. (1997) assumes that the stress along the length of a feed screw has no axial dependence. Therefore, unlike the feeder torque model presented in Section 2.4, in the derivation that follows the torque on each leading screw flight will be different. In order to relate the total feeder torque (T_{total}), which is equivalent to the summation of the torques on each

leading screw flight, to the feeder outlet stress (σ_f), the derivation below must relate the stress at each leading screw flight (σ_i) to the feeder outlet stress.

In the feeder torque model (Yu et al. 1997), the torque on a leading screw flight is given by multiplying the tangential component of the force acting on the leading screw flight by its moment arm. The torque on a leading screw flight in the Solid Plug model is,

$$dT = \frac{\bar{D}}{2} dF^* \sin\left(\bar{\phi}\right), \tag{4.28}$$

which is the tangential component of the unknown force at the leading screw flight (dF^*) multiplied by the moment arm at which it acts ($\bar{D}/2$). The parameter T represents the torque on a leading screw flight, which equals the torque on a feed screw due to a single screw channel. Defining the torque on a leading screw flight as the torque due to a single screw channel is the application of the feeder torque model (Yu et al., 1997). The remainder of the derivation applies the Solid Plug model to determine a relationship between the tangential force at each leading screw flight and the feeder outlet stress.

In order to get the torque on a leading screw flight in terms of the feeder stress, the definition of the unknown force at the leading screw flight is substituted into Equation (4.28) where the conveying force is defined by the Solid Plug model as,

$$dF^* = \frac{B_1 \sigma dL - B_2 d\sigma}{\sin(\bar{\phi}) + \mu_s \cos(\bar{\phi})}, \tag{4.29}$$

which is derived by substituting Equations (4.3-4.11) into Equation (4.19). The parameters B_1 and B_2 are the same as defined previously (Equations (4.24) and (4.25)). The resulting equation is then,

$$dT = \frac{\bar{D}\sin(\bar{\phi})}{2}\left[\frac{B_1\sigma dL - B_2 d\sigma}{\sin(\bar{\phi}) + \mu_s\cos(\bar{\phi})}\right] \tag{4.30}$$

The torque definition is further simplified by substituting in the differential equation from the Solid Plug model (Equation (4.20)),

$$dT = \frac{\bar{D}\sin(\bar{\phi})}{2}\left[\frac{B_1A_2 + B_2A_1}{(A_2 + KB_2)(\sin(\bar{\phi}) + \mu_s\cos(\bar{\phi}))}\right]\sigma dL\,, \tag{4.31}$$

where σ is the stress at the current location (L). Integrating the above equation over a single screw channel gives the torque over a single screw flight,

$$T = C^*L_P\sigma\,, \tag{4.32}$$

where C is defined as,

$$C = \frac{\bar{D}\sin(\bar{\phi})(B_1A_2 + B_2A_1)}{2(A_2 + KB_2)(\sin(\bar{\phi}) + \mu_s\cos(\bar{\phi}))} \tag{4.33}$$

Finally, the torque over a single screw flight is in terms of the Solid Plug model input parameters, pitch length (L_P), and the average axial stress acting on the leading screw flight (σ).

The total feeder torque (T_{total}) is then the summation of the torques due to each leading screw flight,

$$T_{total} = \sum_{i=1}^{m} T_i = CL_p\sum_{i=1}^{m}\sigma_i\,, \tag{4.34}$$

where T_i is the torque on the feed screw due to the i^{th} leading screw flight downstream from the feeder inlet, σ_i is the average axial stress at the i^{th} leading screw flight, and m is the number of screw flights. Equation (4.34) gives the total feeder torque as a function of the stress at each leading screw flight. In order to obtain the feeder torque in terms of the

feeder outlet stress, the stress at each leading screw flight must be related to the feeder outlet stress. In the derivation below, the stress at each leading screw flight is first related to the feeder inlet stress which is then related to the feeder outlet stress. These relationships can be determined from the Solid Plug model (Equation (4.20)). From the Solid Plug model, the stress an axial distance dL downstream from the feeder inlet (σ_{dL}) is related to the feeder inlet stress by,

$$\sigma_{dL} = \frac{KB_1 - A_1}{KB_2 + A_2} dL\sigma_0 + \sigma_0 \tag{4.35}$$

Continuing downstream, the stress an axial distance 2dL from the feeder inlet (σ_{2dL}) is given by,

$$\sigma_{2dL} = \frac{KB_1 - A_1}{KB_2 + A_2} dL\sigma_{dL} + \sigma_{dL}, \tag{4.36}$$

which can be related to the feeder inlet stress by substituting Equation (4.35) into Equation (4.36),

$$\sigma_{2dL} = \frac{KB_1 - A_1}{KB_2 + A_2}^2 dL^2\sigma_0 + 2\frac{KB_1 - A_1}{KB_2 + A_2} dL\sigma_0 + \sigma_0 \tag{4.37}$$

The stress any axial distance downstream from the feeder inlet (σ_{ndL}) can be related to the feeder inlet stress by,

$$\sigma_{ndL} = \left[\frac{KB_1 - A_1}{KB_2 + A_2} dL\right]^n \sigma_0 + \sum_{j=1}^{n-1}\left[\frac{KB_1 - A_1}{KB_2 + A_2} dL\right]^{n-j} n\sigma_0 + \sigma_0, \tag{4.38}$$

where the axial distance downstream from the feeder inlet is given by n*dL. Again, n is the number of steps downstream from the feeder inlet of size dL. The stress at the i^{th} leading screw flight can be determined by setting the axial distance downstream from the

feeder inlet equal to the location of the leading screw flight ($n * dL = i * L_p$, where L_p again is the pitch length). Setting $n = i(L_P/dL)$, and substituting Equation (4.38) into Equation (4.34) gives the feeder torque in terms of the feeder inlet stress,

$$T_{total} = \sum_{i=1}^{m} T_i = CL_p \sum_{i=1}^{m} \left(\left[\frac{KB_1 - A_1}{KB_2 + A_2} dL \right]^{i(L_P/dL)} \sigma_0 + \sum_{j=1}^{i(L_P/dL)-1} \left[\frac{KB_1 - A_1}{KB_2 + A_2} dL \right]^{i(L_P/dL)-j} i(L_P/dL)\sigma_0 + \sigma_0 \right) \tag{4.39}$$

Lastly, the feeder inlet stress is related to the feeder outlet stress (σ_f) by setting $n = L_f/dL$ in Equation (4.38),

$$\sigma_f = \left[\frac{KB_1 - A_1}{KB_2 + A_2} dL \right]^{L_f/dL} \sigma_0 + \sum_{j=1}^{L_f/dL-1} \left[\frac{KB_1 - A_1}{KB_2 + A_2} dL \right]^{(L_f/dL-j)} (L_f/dL)\sigma_0 + \sigma_0 \tag{4.40}$$

Solving Equation (4.40) for the feeder inlet stress and substituting into Equation (4.39) gives the feeder torque in terms of the feeder outlet stress,

$$T_{total} = \sum_{0}^{n} T_i = CL_p\sigma_f \frac{\sum_{i=1}^{m} \left(\left[\frac{KB_1 - A_1}{KB_2 + A_2} dL \right]^{i(L_P/dL)} + i\frac{L_P}{dL} \sum_{j=1}^{i(L_P/dL)-1} \left[\frac{KB_1 - A_1}{KB_2 + A_2} dL \right]^{i(L_P/dL)-j} + 1 \right)}{\left[\frac{KB_1 - A_1}{KB_2 + A_2} dL \right]^{L_f/dL} + \frac{L_f}{dL} \sum_{j=1}^{L_f/dL-1} \left[\frac{KB_1 - A_1}{KB_2 + A_2} dL \right]^{(L_f/dL-j)} + 1} \tag{4.41}$$

The above equation shows that there is a linear relationship between the feeder torque and feeder outlet stress, and that the feeder torque-outlet stress relationship depends on the same parameters as the Solid Plug model.

CHAPTER 5. SOLID PLUG MODEL INPUT PARAMETERS

In order to predict the feeder outlet stress, the Solid Plug model requires as inputs: the feeder geometry, feed screw speed, mass flow rate, feeder inlet stress, material density, material stress ratio, and material-feeder friction coefficients. All input parameters necessary to predict the experimental results are given in this chapter (Table 5.1). The screw speed and experimental mass flow rate range are given in Table 5.1; however, they are discussed in Chapters 6 and 7, respectively.

Table 5.1. Solid Plug model experimental input parameters.

Input Parameter	Notation	Input Value
Screw flight thickness	e	0.32 ± 0.01 cm
Number of screw flights	p	2
Total feeder length	L_f	21.0 ± 0.01 cm
Pitch length	L_p	2.09 ± 0.01 cm
Screw core diameter	D_{sc}	1.40 ± 0.01 cm
Barrel diameter	D_b	3.80 ± 0.01 cm
Average feeder diameter	$\overline{D}$	2.60 ± 0.02 cm
Screw channel width at the screw core	W_{sc}	1.20 ± 0.01 cm
Screw channel width at the barrel surface	W_b	1.65 ± 0.01 cm
Average screw channel width	$\overline{W}$	1.54 ± 0.01 cm
Helical angle at the screw core	$\emptyset_{sc}$	43.54 ± 0.25 deg
Helical angle at the barrel surface	$\emptyset_b$	19.29 ± 0.10 deg
Average helical angle	$\overline{\emptyset}$	27.10 ± 0.21 deg
Screw channel height	H	1.05 ± 0.01 cm
Stress ratio applied at the barrel and screw core surfaces	k_r	1
Stress ratio applied at the screw flights	k_t	1
Feeder inlet stress	σ_0	200 Pa
Barrel friction coefficient	μ_b	0.28
Screw friction coefficient	μ_s	0.15
Stress-density relationship	$\rho(\sigma)$	$\frac{\rho(\sigma)}{\rho_{pb}} = 0.029 * \log(\sigma/\sigma_0) + 1.154$
Bulk density of Avicel PH 102	ρ_{pb}	$0.32\ g/cm^3$
Feed screw speed	V_s	30 ± 0.3 rpm
Mass flow rate	$\dot{M}$	$220 - 245\ g/min$

5.1 Feeder Geometry

The feed screw (figure 5.1) and barrel which comprise the components of the feeder were taken from a WP 120 Alexanderwerks Roll Compactor. While most of the feed screw geometry was measured using Vernier calipers, it was not possible to measure the average channel width, channel width at the screw core, or helical angles. Instead they were calculated (Equations (5.1) – (5.3)) (White et al., 2003) using,

$$\bar{W} = L_P \cos\left(\bar{\phi}\right) - e, \tag{5.1}$$

$$W_{sc} = L_P \cos\left(\phi_{sc}\right) - e, \tag{5.2}$$

and,

$$\phi = \arctan\left(\frac{p*L_p}{\pi D}\right) \tag{5.3}$$

The diameter (D) in Equation (5.3) varied depending on where the helical angle (∅) was being calculated. For example, in order to find the helical angle at the screw core ($\emptyset_{sc}$), the diameter at the screw core (D_{sc}) was taken in Equation (5.3).

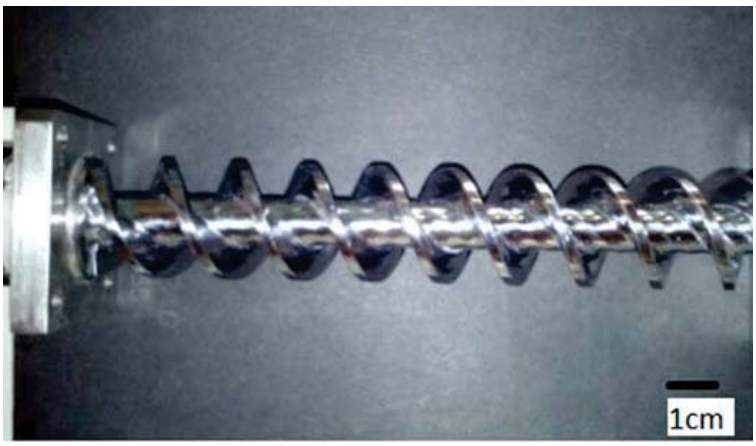

Figure 5.1. An image of the standard WP 120 Alexanderwerks Roll Compactor feed screw used in the experimental trials.

5.2 Feeder Inlet Stress

The feeder inlet stress was assumed to be constant and equal to the outlet stress of the hopper used in the experiments, which was from a WP 120 Alexanderwerks Roll Compactor. The hopper outlet stress was experimentally determined by measuring the force at the hopper outlet and dividing by the hopper outlet area (12.9 cm^2). In the experimental setup shown (Figure 5.2), the hopper was elevated slightly above a spacer placed on a laboratory scale (Mettler Toledo SB 8001), such that the scale was not measuring the weight of the hopper. Also, the gap between the spacer and hopper outlet was small enough to prevent material from flowing out of the hopper. The spacer simply made it easier to adjust the experimental setup. The goal was to measure the weight of the material not supported by the hopper walls (Janssen, 1895).

Figure 5.2. Experimental setup to measure the hopper outlet stress (feeder inlet stress).

During the measurement of the hopper outlet stress, material was carefully added to the hopper in order to prevent compaction of the material within the hopper. Material

compaction would occur due to impact when either a large amount of material was added, or material was poured from a greater height above the hopper. It was observed that if the material was poured into the hopper carelessly, material would impact at the base of the hopper and bridge across the hopper outlet. In these instances there would be no measured hopper outlet stress. Microcrystalline cellulose (Avicel PH 102), the material used during experimental trials, was thus added to the hopper approximately 50 grams at a time in order to capture the relationship between the mass of material in the hopper and the hopper outlet stress (Figure 5.3). This process of measuring the hopper outlet stress was performed three separate times.

The asymptotic trend shown in Figure 5.3 matches that of Janssen's analysis (Janssen, 1895) for stress in a silo. Janssen's analysis predicts that an asymptotic stress value is reached as the bed depth of a granular material increases. Here, increasing the mass of material in the hopper has the same effect. An experimental asymptotic stress of 200 Pa is reached when the hopper is full, which is then taken to be the feeder inlet stress.

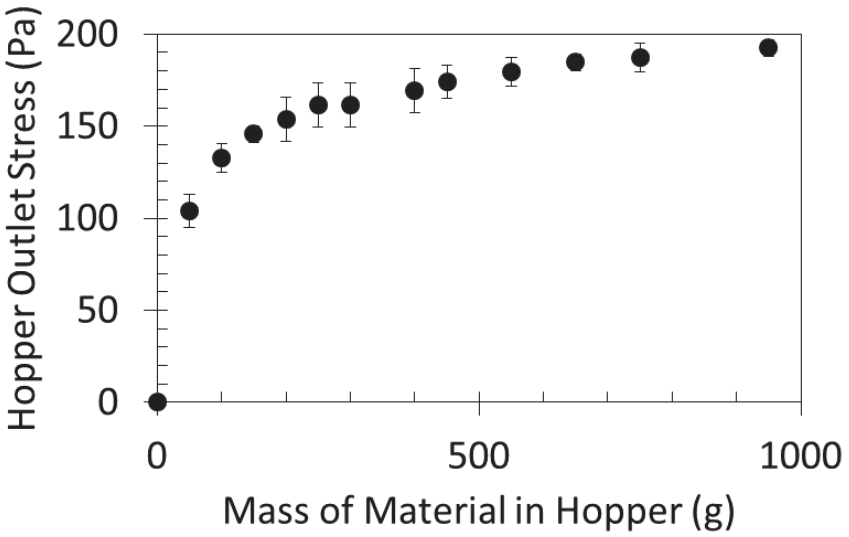

Figure 5.3. Experimentally measured hopper outlet stress as a function of the mass of material in the hopper. The asymptotic outlet stress of 200 Pa is set as the feeder inlet stress for the Solid Plug model. The error bars correspond to the standard deviation between three separate measurements.

5.3 Material Input Parameters

An FT4 powder rheometer (Figure 5.4) was used to measure the stress-density relationship, stress ratio, and material-feeder friction coefficients of microcrystalline cellulose (Avicel PH 102). Avicel PH 102 is a pharmaceutical excipient commonly used as a binder in dry granulation processes and was used in all of the experimental trials. The FT4 rheometer is capable of applying forces up to 50 N with a resolution of +/- 0.0001 N, which allowed the range of stresses (0.2- 20 kPa) applied in the tests to correspond to those expected within a roll compactor powder feed screw.

Figure 5.4. FT4 powder rheometer used for material characterization.

The steps for each of the measurements discussed below are the conditioning and compaction cycles of the material. After material was poured into a 50 mm diameter, 85 ml vessel (Figure 5.5), the material was conditioned in order to create a more homogenously dense sample and to remove operator bias as to how the sample was prepared. A 48 mm blade (Figure 5.6) rotated at a rate of 60 mm/sec and traversed through the sample. Next, the 48 mm blade was removed from the rheometer and a vented piston was attached (Figure 5.6). The piston applied a normal force of 0.2 kPa, at a rate of 0.05 mm/sec for 60 seconds to compact the material. The sample was then split by rotating the top half of the 50 mm diameter, 85 ml vessel (Figure 5.5). Splitting the sample created a level powder bed surface and reduced the powder bed height. The specific steps for each measurement and their corresponding results are discussed below.

Figure 5.5. FT4 vessel for material testing.

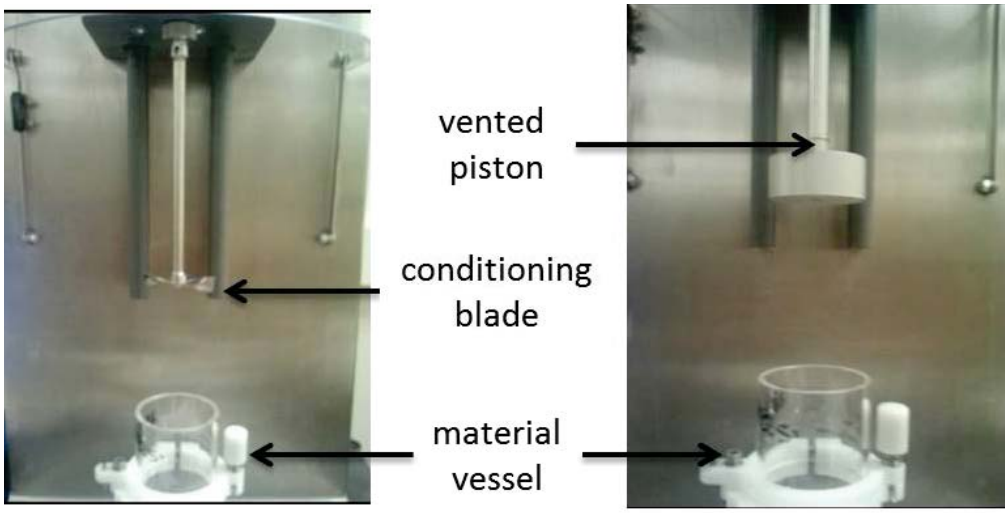

Figure 5.6. FT4 conditioning blade (left) and vented piston (right) attachments used to prepare the samples.

5.3.1 Stress-Density Relationship

The materials used in roller compaction processes in the pharmaceutical industry are highly compressible in nature and therefore the constant material density assumption made by the Solid Plug models in the literature (Darnell et al., 1956; Tadmor et al., 1972;

Campbell et al., 1995) is a poor one. Instead, in the present work a stress-density relationship is applied to the Solid Plug models. The stress-density relationship for Avicel PH 102 measured using an FT4 rheometer is shown in Figure 5.7. The poured bulk density ($\rho_{pb} = 0.32\ g/cm^3$) and tapped bulk density ($\rho_{tb} = 0.42\ g/cm^3$), which were measured using an Agilent 350 Tapped Density Tester and following the USP 25-NF 20 <616> standard procedures, are also recorded for reference. In order to measure the stress-density relationship, the material in the vessel was compacted using a compaction piston. After the conditioning and compaction cycles described above, the compaction piston applied a specified normal stress for 60 sec. The FT4 rheometer calculates the density of the material in the vessel and measures the normal stress applied by the compaction piston. By varying the applied normal stress, a stress-density relationship can be determined. A logarithmic curve fit was applied to the experimental data (Figure 5.7) in order to apply the stress-density relationship to the Solid Plug model (Figure 4.5). A logarithmic curve fit was chosen because in literature (Briscoe et al., 1997) the stress-density relationship of particulate material has been shown to follow a logarithmic trend.

There is little uncertainty in the stress-density relationship measured by the FT4 rheometer because of the accuracy of the stress and density measurements. Over the applied stress range of 0.2 kPa – 20 kPa, the uncertainty of the applied normal stress varied from 7.3×10^{-2} kPa – 5.1×10^{-4} kPa, respectively. The uncertainty is small in comparison to the applied normal stress due to the resolution of the force measured by the FT4 rheometer (+/- 0.0001 N). Over the applied stress range the equivalent applied forces ranged from 0.25 N to 36 N. The resolution of the force measured by the FT4

rheometer also contributes to the small uncertainty in the density measurements. Again, the FT4 rheometer directly measures the material density. The uncertainty of the material's weight and volume both contribute to the uncertainty of the material's density. The weight of the material is calculated as the force measured by the FT4 rheometer divided by the gravitational constant. Therefore, the uncertainty of the material's weight is proportional to the uncertainty of the force measured. The volume of the material is calculated by multiplying the cross sectional area of the material vessel (Figure 5.5) by the depth of the powder bed. The depth of the powder bed is calculated by subtracting the displacement of the compaction piston from the known length of the material vessel. The uncertainty in the displacement of the piston is +/- 0.001 cm. As a result of the uncertainty in the material's weight and volume, the largest uncertainty of the material's density was calculated to be 0.01% g/cm^3.

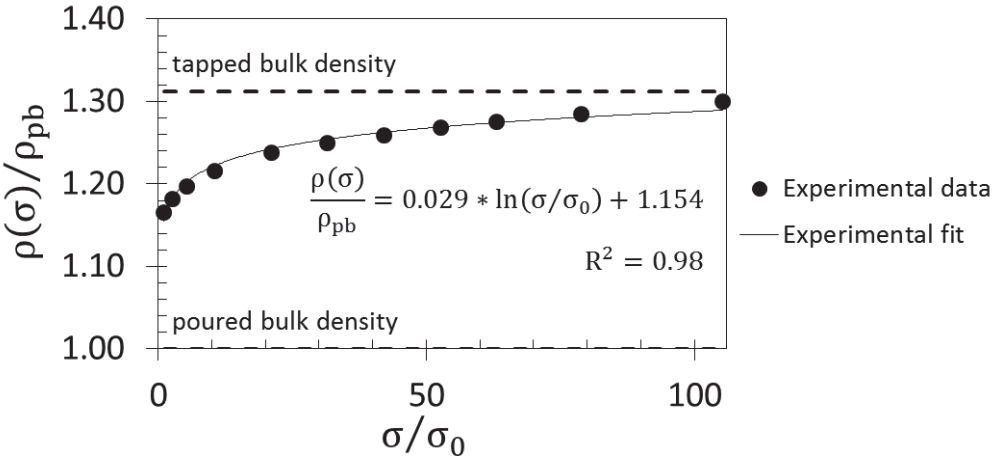

Figure 5.7. Stress-density relationship for Avicel 102, measured using a FT4 compression test. An empirical fitting equation is also shown, where the stress has normalized by the feeder inlet stress and the material density has been normalized by the poured bulk density (ρ_{pb}).

The material stress-density relationship is incorporated into the conveying angle equation (Equation (4.27)), where typically the material density is taken as a constant. The iterative method of solving the Solid Plug model with the application of the stress-density relationship is outlined in Figure 4.5. To ensure that the Solid Plug models' predictions were independent of the step size downstream, a step size independence test was performed. The step size, which was related to the feeder geometry by the pitch length (L_P), was decreased until a variation of less than 1% occurred between feeder outlet stress predictions for successive step sizes (Table 5.2). The necessary step size to meet the 1% threshold was $L_P/1000$. The influence of the stress-density relationship is discussed more in Chapter 9.

Table 5.2. Variation in the feeder outlet stress due to a change in step size.

Step Size	Maximum Percent Difference in Feeder Outlet Stress from the Prior Step Size Over the Experimental Mass Flow Rate Range
L_p	---
$L_p/10$	$7.35*10^4$ %
$L_p/100$	90.06 %
$L_p/250$	4.80 %
$L_p/500$	1.60 %
$L_p/1000$	0.80 %

5.3.2 Stress Ratio

The stress ratio is the ratio of the minor to major principal stresses acting in the material ($k = \sigma_2/\sigma_1$). In the literature, the range of stress ratios given for powder materials is between 0.3 – 0.6 (Fenner, 1977). These experimentally measured stress

ratios come from punch and die experiments in which the material is static. For microcrystalline cellulose, Michrafy et al. (2004) uses a stress ratio of 0.45; however, this value comes from a curve fit of experimental data in which sodium chloride powder was used (Es-Saheb, 1992, Figure 6).

For the current work, the stress ratio was calculated from shear cell tests performed using an FT4 rheometer 48 mm shear cell. After the initial conditioning steps of the material, the vented piston was replaced with the shear cell attachment (Figure 5.8). For a single test, the shear cell applied five normal stresses ranging from 20% - 100% of the consolidation stress. At each applied normal stress the material was sheared at a rate of 30 deg/min till incipient powder failure, which corresponded to the maximum torque reading from the FT4 rheometer. The maximum shear stress vs. normal stress relationship was plotted to produce a yield locus. The data analysis software then produced a Mohr's circle corresponding to incipient flow. The Mohr's circle gives the principal stresses (σ_1 and σ_2) as the x intercepts (Figure 5.9). The consolidation stress was varied from 0.2 - 20 kPa to produce a family of Mohr's circles, from which the major to minor principal stresses are plotted in Figure 5.10. The measured stress ratio of Avicel PH 102 for these conditions was 0.22. The stress ratio equation (Equation (5.4)) derived from Mohr's circle analysis by Yu et al. (1997),

$$k = \frac{1}{1 + 2\tan(\delta)^2 + 2\left[\left(1+\tan(\delta)^2\right)\left(\tan(\delta)^2 - \mu_w{}^2\right)\right]^{1/2}}, \tag{5.4}$$

verified the experimentally measured stress ratio. The stress ratio of Avicel PH 102 was calculated to be 0.23, where the material internal friction angle (δ) was calculated from

the shear cell measurements to be 43.23 deg and the wall friction coefficient (μ_w) was taken to be 0.15 (note Equation 5.4 is insensitive to the wall friction coefficient).

The uncertainty in the experimentally measured stress ratio results from the uncertainty of the normal stress and shear stress measurements made by the FT4 rheometer (Figure 5.9). The relative uncertainty of the normal stress stays relatively constant at 0.4% over the applied stress range (0.2 kPa – 20 kPa). The shear stress (τ) is calculated by the FT4 rheometer by applying the following definition,

$$\tau = \frac{Tr}{J_T}, \tag{5.5}$$

where T is the torque acting on the shear cell, r is the distance from the axis of rotation to the outer diameter of the shear cell, and J_T is the torsion constant. Given that r and J_T are constants, the uncertainty of the shear stress is proportional to the uncertainty of the torque measurements. The FT4 rheometer is capable of measuring torques up to 900 mN.m with a resolution of +/- 0.02 mN.m. The uncertainty of the torque measurements ranged from 0.01% - 0.53%, decreasing as the applied shear stress increased. Due to the small uncertainty in the normal and shear stress measurements, the uncertainty of the stress ratio is insignificant.

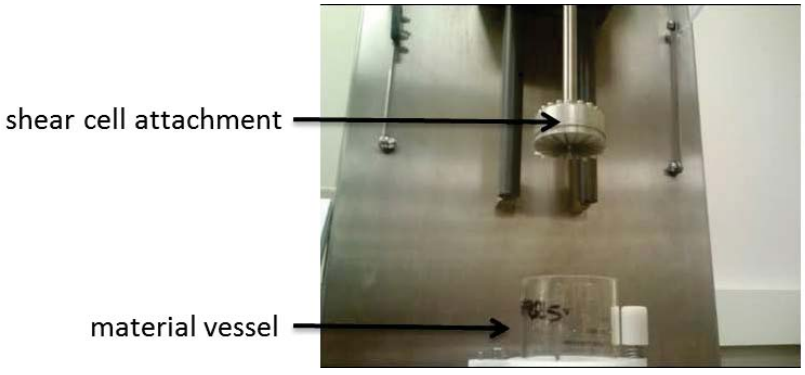

Figure 5.8. FT4 48 mm shear cell attachment.

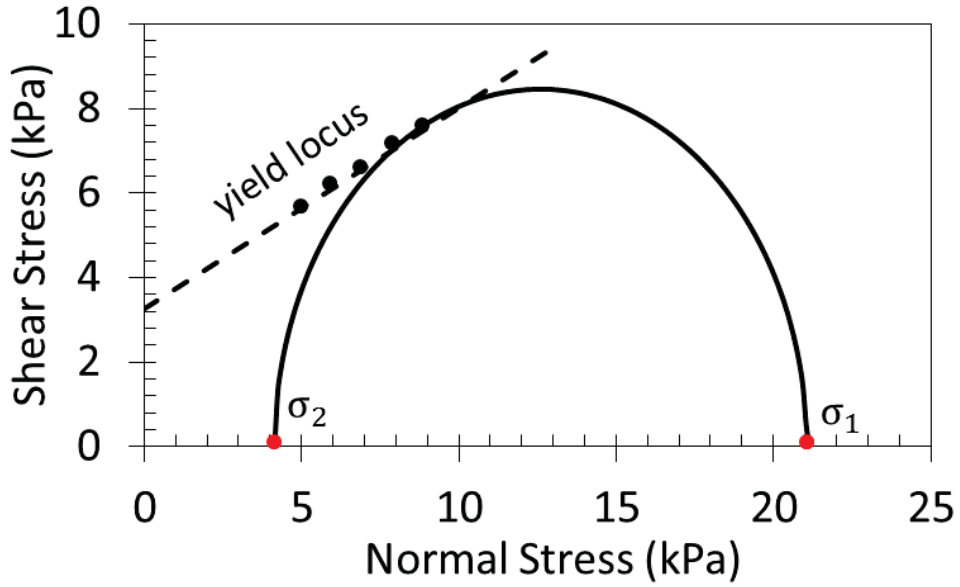

Figure 5.9. Mohr's circle created from analysis of a single shear cell run, highlighting the major and minor principal stresses.

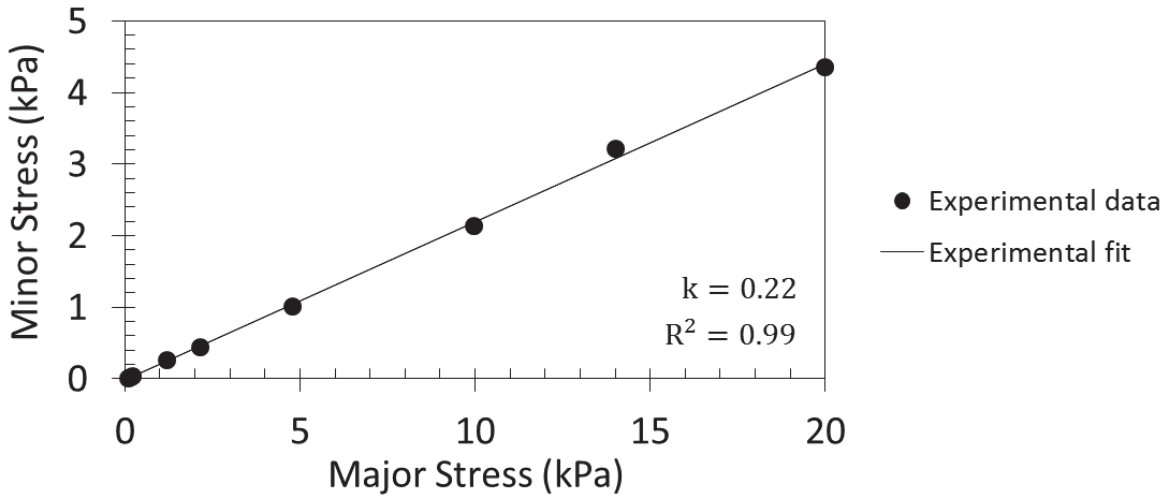

Figure 5.10. Major and minor principal stresses recorded for each shear cell run. The ratio of the minor to major principal stresses (slope of the line) gives the stress ratio for Avicel PH 102.

The stress ratio measured in this work and those measured in the literature are for experimental setups where the material is static. These experimentally measured static stress ratios do not replicate the feed screw environment. The shear cell rotated at a rate

of 0.083 rpm (instrumentation standard, shear rate $18^{o}/\min$) compared to the feed screw which rotates at 30 rpm. The stress ratio of sheared material is shown in the literature for the kinetic theory of granular materials (Savage et al., 1981; Walton et al., 1986; Lun et al., 1987; Campbell, 1989; Lun, 1991;) to be different than those experimentally measured values of a static material (Es-Saheb, 1992; Hyun et al. 1997a; Briscoe et al. 1998).

The case of simple sheared material at high shear rates is the focus of analytical and computational models developed in the literature for the kinetic theory of granular materials. Since the kinetic theory of granular materials is well developed in the literature and not of primary focus here, it will not be discussed in detail. The results of the models, however, are given. An analytical model of the kinetic theory for granular materials (Lun et al., 1987; Lun, 1991) predicts a stress ratio of one, and two and three dimensional computational DEM models (Walton, 1986; Campbell, 1989; da Cruz et al., 2005) also indicate a stress ratio equal to one for solid fractions between 0.2-0.6. These DEM models assume the granular material to be smooth, hard, elastic spheres, with varying degrees of elasticity and roughness. Since the particles in the simulations were assumed to be hard (non-deformable), solid fractions greater than 0.6 could not be attained. However, DEM simulations which used soft particles (deformable) (Walton et al., 1986) were able to attain solid fractions up to 0.8. While the DEM models which used soft particles also indicated a stress ratio equal to one for solid fractions between 0.2- 0.6, at solid fractions greater than 0.6 the stress ratio was shown to decrease (Walton et al. 1986).

From the kinetic theory for granular materials, a stress ratio of one is thought to be more applicable for the powder feed screw of a roll compactor than the experimentally measured static stress ratio. A stress ratio of one is thought to be more applicable because the poured bulk density of Avicel PH 102 gives a solid fraction above 0.2 $\left(\frac{\text{poured bulk density}}{\text{true density}} = \frac{0.32\ \text{g/cm}^3}{1.52\ \text{g/cm}^3}\right)$, which is the point where the kinetic theory for granular material computational models approach a stress ratio of one predicted by the analytical models. With an expected increase in stress along the length of the feed screw, the solid fractions are then expected to be greater than 0.2. While the kinetic theory for granular materials shows that the stress ratio may vary along the length of the feed screw as the solid fraction of the material increases beyond 0.6, the current work assumes a constant stress ratio as was done in the Solid Plug models (Tadmor et al., 1972; Lovegrove et al., 1974; Campbell et al., 1995; Hyun et al., 1997a). The stress ratio is also assumed to be one because the kinetic theory of granular materials captures the shearing environment which the material in the feed screw is subject to during conveying, whereas the static experimental measurements of the stress ratio do not. Again, the shear cell rotated at a rate of 0.083 rpm and the screw rotated at a rate of 30 rpm.

The remainder of this thesis focuses on Solid Plug models for which a stress ratio of one is applied. Nevertheless, the experimentally measured high solid fraction stress ratio will also be applied to the Solid Plug models in order to observe the effects of the stress ratio. The application of the experimentally measured static stress ratio is reasonable since the stress ratio applied in the work of Hyun et al. (1997a) was measured using a static punch and die experiment. However, a majority of the Solid Plug models

assume a stress ratio of one (Darnell et al., 1956; Tadmor et al., 1972; Campbell et al., 1995).

5.3.3 Friction Coefficients

The last material parameters needed for the Solid Plug model are the feed screw and barrel friction coefficients. In order to measure these friction coefficients, material test coupons of the same surface roughness and surface finish as the feed screw and barrel needed to be made. In order to characterize the feed screw and barrel surfaces, the surface roughness was measured using an optical surface profilometer (Zemetrics Zescope). The surface roughness values of the feed screw and barrel ranged from 0.2 – 0.25 and 0.58 – 0.64 μm, respectively. The surface finishes could not be attained from the manufacturer; therefore, suitable material test coupons could not be produced for friction measurements. Instead, the friction coefficients were estimated based on the surface roughness values alone. The sensitivity of the Solid Plug model to the friction coefficients is discussed in Chapter 8 because the surface finish of a material has been shown to vary the friction coefficient values by one half to one third (Darnell et al., 1956).

To estimate the friction coefficients of the feed screw and barrel, the friction coefficients for three material test coupons of varying roughness values (1.20, 0.28, and 0.05 μm) (Figure 5.11) were measured using an FT4 rheometer. The material test coupons were provided with the FT4 rheometer. Both the material test coupons (http://www.freemantech.co.uk/) and the feed screw and barrel (http://www.alexanderwerk.com/) were made from medical grade stainless steel. After conditioning the material in the vessel, the wall friction material test coupons were

attached to the FT4 rheometer and the material was sheared at a rate of $18^{o}/\text{min}$. The FT4 rheometer then calculates the friction coefficients as the ratio of the shear stress to the applied normal stress. The friction coefficients could then be characterized over the range of 0.2 – 20 kPa by varying the applied normal stress (Figure 5.12). Each of the wall friction coefficients was observed to reach a constant value over the applied stress range of 5 – 20 kPa. From the friction coefficients measured over the stress range of 5 – 20 kPa, where the friction coefficient remains nearly constant, the friction coefficients of the feed screw and barrel were interpolated to be 0.15 and 0.28, respectively (Figure 5.13). These friction coefficients were assumed to be constant over the length of the feeder.

The FT4 rheometer calculates the wall friction coefficient (μ_w) by applying the following definition,

$$\mu_w = \frac{\tau}{\sigma}, \tag{5.6}$$

where σ is the applied normal stress and τ is the shear stress. The uncertainty of the wall friction coefficient then depends on the uncertainty of both the normal and shear stress measurements. Since the uncertainty of the normal and shear stress measurements have been discussed previously within this section, only the uncertainty of the wall friction coefficient is given here. The uncertainty in the friction coefficients ranged from 0.04% - 0.27%.

Figure 5.11. Wall friction test coupons used to measure friction coefficients (from left to right 1.20, 0.28, and 0.05 μm roughness).

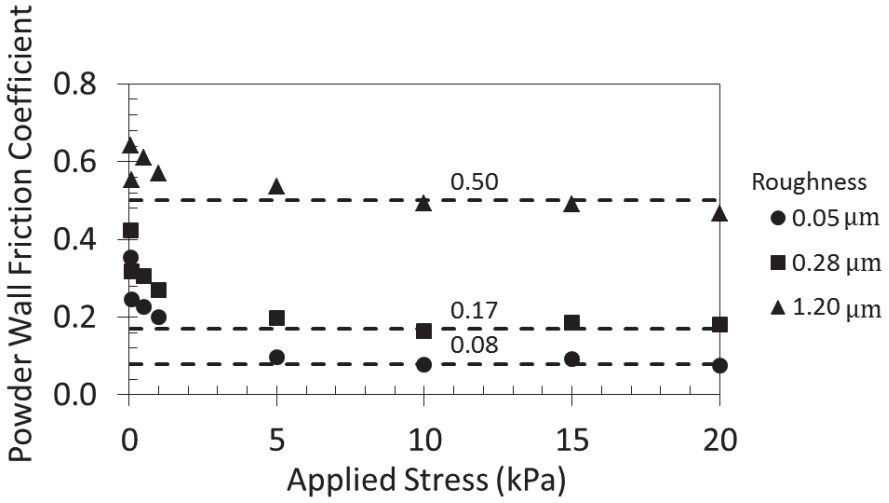

Figure 5.12. Measurements of the friction coefficients for wall friction test coupons of 1.20, 0.28, and 0.05 μm roughness. The dashed lines are the average friction coefficient values over the stress range 5 – 20 kPa.

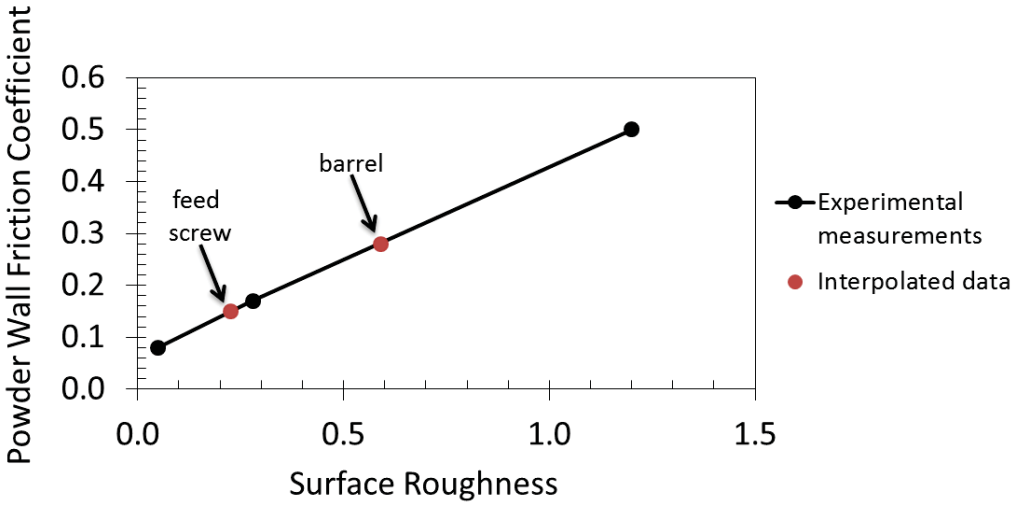

Figure 5.13. Friction coefficients as a function of the surface roughness for the wall friction test coupons. This plot was used to interpolate the friction coefficients of the feed screw and barrel with surface roughness values measured to be 0.23 and 0.59 μm, respectively.

CHAPTER 6. EXPERIMENTAL METHOD

The experimental setup shown in Figures 6.1 and 6.2 tests the applicability of the Solid Plug models (Darnell et al., 1956; Tadmor et al., 1972; Campbell et al., 1995; Hyun et al., 1997a) to a powder feed screw of a roll compactor and it measures the feed screw torque-outlet stress relationship. The experimental setup was designed to simulate a WP 120 Alexanderwerks Roll Compactor feed screw section. The feed screw, barrel, and hopper used in the experiment are taken directly from a WP 120 Alexanderwerks Roll Compactor, and the feed screw drive system was capable of generating the maximum screw speed (60 rpm) and torque (38 N.m) of a WP 120 Alexanderwerks Roll Compactor.

The feed screw drive system included an adjustable speed DC motor (Dayton 1F798) and a 10:1 ratio gear box (Boston Gear F718-B5). Between the motor and gear box is a torque sensor (Futek TRS605), and to assure that the torque sensor was not overloaded, a shaft-to-shaft mount slip ring (TORQ-TENDER Zero-Max H-TLC-1000-C) was implemented as the connection between the gear box and feed screw. The slip ring works such that, if the feeder torque exceeded 40 N.m, then the feed screw shaft would disengage from the drive system, eliminating the torque.

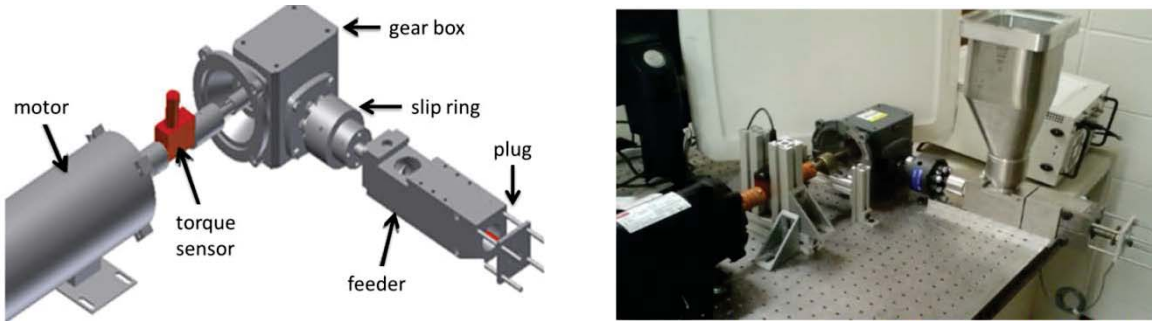

Figure 6.1. Experimental setup used to simulate the feed screw section of a WP 120 Alexanderwerks Roll Compactor.

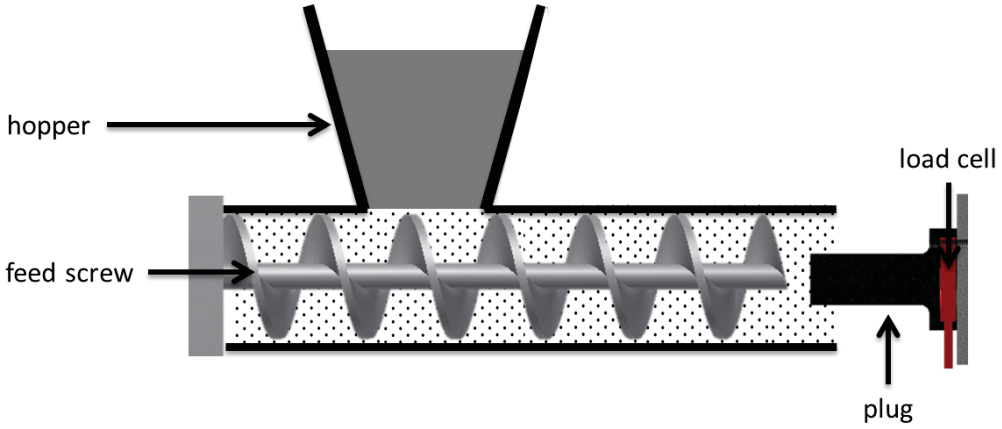

Figure 6.2. Schematic of the experimental feeder setup.

In order to measure and vary the feeder outlet stress, plugs of different cross-sectional areas were positioned at the feeder outlet (Figure 6.3). For the experimental trials a single plug which gave an open outlet area-to-barrel outlet area ratio of 0.75 was made (Figure 6.4). In order to decrease the open outlet area-to-barrel outlet area ratio further, attachments which increased the cross-sectional area of the plug (Figure 6.5) were also made. The experimental approach applied here is similar to the experimental approach applied in the literature (Hyun et al., 1997a). The plugs at the feeder outlet mimic the flow restrictions due to the rolls at the outlet of a roll compactor. The ratios of open outlet area-to-barrel outlet area tested in this study ranged from 0.75 – 0.36 (Table

6.1). At open outlet area-to-barrel outlet area ratios greater than 0.75 no measureable outlet stress was applied to the plugs and at ratios lower than 0.36 the feeder would jam. The outlet stress was calculated by dividing the force applied to the plug by the cross-sectional area of the plug. The force applied to the plug was measured by a 250 lbf load button load cell (Futek LLB400) located at the base of the plug (Figure 6.6). The uncertainty of the load cell measurements was +/- 0.001 lbf. The relative uncertainty of the calculated outlet stress is given in Appendix B. The load cell was wired to an NI DAQ device (National Instruments NI cDAQ-9171), which allowed the force to be recorded by a LabView program and supplied the load cell with 10 V of power (equivalent to the excitation during calibration). The rate of data acquisition for the load cell was 100 Hz. The plug was inserted 0.6 +/- 0.1 cm into the barrel leaving 0.4 +/-0.1 cm between the end of the feed screw and the plug (Figure 6.4). The plug insertion depth was set to 0.6 cm to ensure that the attachments (Figure 6.5), which were 0.5 cm thick, were fully inserted into the barrel. Also, the distance between the end of the feed screw and the plug was maximized to ensure that the plug did not come into contact with the feed screw during the experimental trials. It is discussed in Chapter 7 that the insertion depth of the plug had have no effect on the experimental measurements.

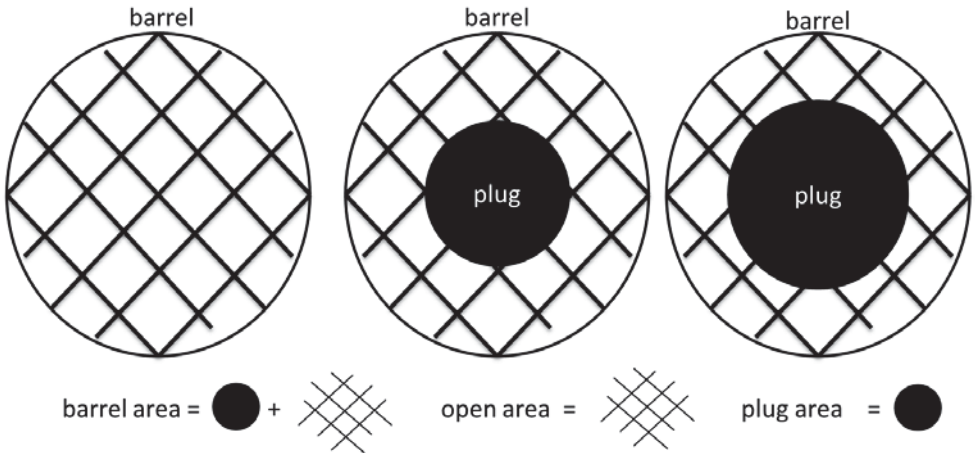

Figure 6.3. Feeder outlet schematic, demonstrating a decrease in the ratio of open area to barrel area as the plug area increases to the right.

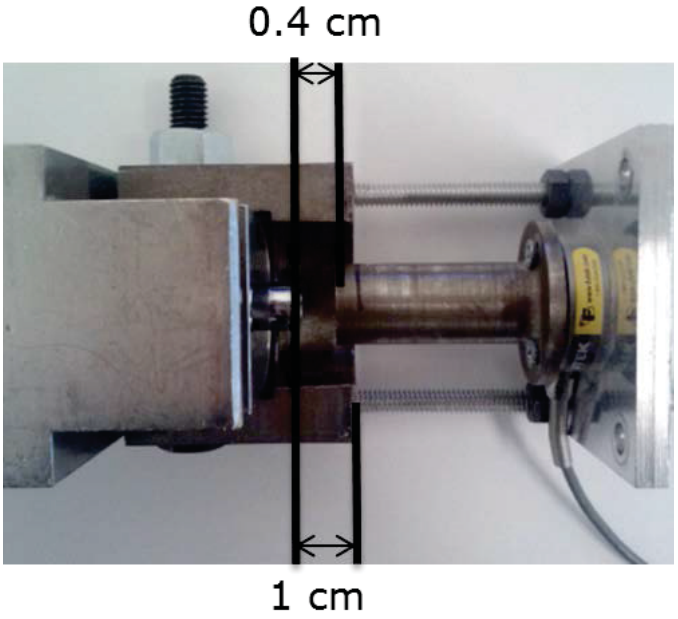

Figure 6.4. Image showing the gap between the feed screw tip (left) and plug (right).

Figure 6.5. Image showing the plug attachments. The plug diameters from left to right are 2.09, 2.29, 2.50, 2.67, 2.85, and 3.04.

Table 6.1. List of the plug diameters, corresponding open outlet areas, and ratios of the open area to barrel area applied in the experimental trials.

Barrel Diameter (cm)	Plug Diameters (cm)	Corresponding Open Outlet Area (cm^2)	$\frac{\text{Open Area}}{\text{Barrel Area}}$
3.81	0.00	11.40	1.00
	1.90 +/- 0.01	8.55	0.75
	2.09 +/- 0.01	7.98	0.70
	2.29 +/- 0.01	7.30	0.64
	2.50 +/- 0.01	6.61	0.58
	2.67 +/- 0.01	5.81	0.51
	2.85 +/- 0.01	5.02	0.44
	3.04 +/- 0.01	4.10	0.36

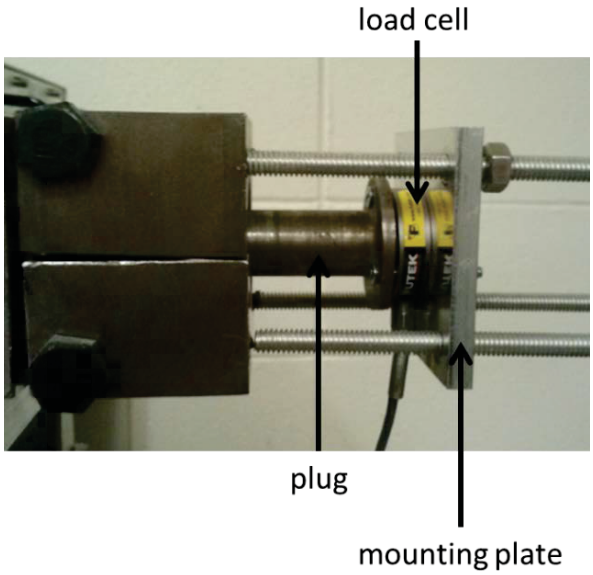

Figure 6.6. The barrel outlet boundary condition for the experimental setup, highlighting the plug, load cell, and mounting plate.

For the plug to be mounted on the feeder, an attachment to the barrel was made out of steel (Figure 6.7). This attachment also provided space for the plug between the feed screw tip and feeder outlet. The outlet area of the attachment was the same as that of the original feeder outlet area. Threaded rods extending from the feeder attachment held the mounting plate for the plug and load cell. Clearance holes in the mounting plate allowed for the plug to be translated in and out of the barrel, which is how the plug insertion depth was set. Once the plug was at the proper insertion depth, the mounting plate was fixed into place with lock nuts on either side, effectively clamping it in place. The plug, load cell, and mounting plate assembly were fastened together. Clearance holes in the plug and mounting plate meant that the stress was not being transferred to the fasteners, but that the stress was transferred to the load cell.

Figure 6.7. Image showing the feeder attachment (bottom) and the original feeder geometry (top).

To measure the feeder torque, a 5 N.m torque sensor (Futek TRS605) was placed between the motor and gear box (Figure 6.1) of the drive system. The torque read by the sensor was then multiplied by the gear box ratio (10:1) to determine the feed screw torque. The uncertainty of the torque sensor reading was +/- 0.0001 N.m, therefore the uncertainty of the recorded data is +/- 0.001 N.m. The torque sensor was supplied 12 V of power (Agilent E3361A), equivalent to the power supplied during calibration. The signal output of the sensor was connected to a LabView chassis (National Instruments NI PXI 1042) and a LabView code then recorded and plotted the signal output of the torque sensor at a rate of 100 Hz. A high pass filter with a threshold equal to the motor frequency was used to eliminate the noise from the motor in the torque signal. A fast Fourier transform (fft), performed on the torque signal, determined that the noise was coming from the motor (Figure 6.8).

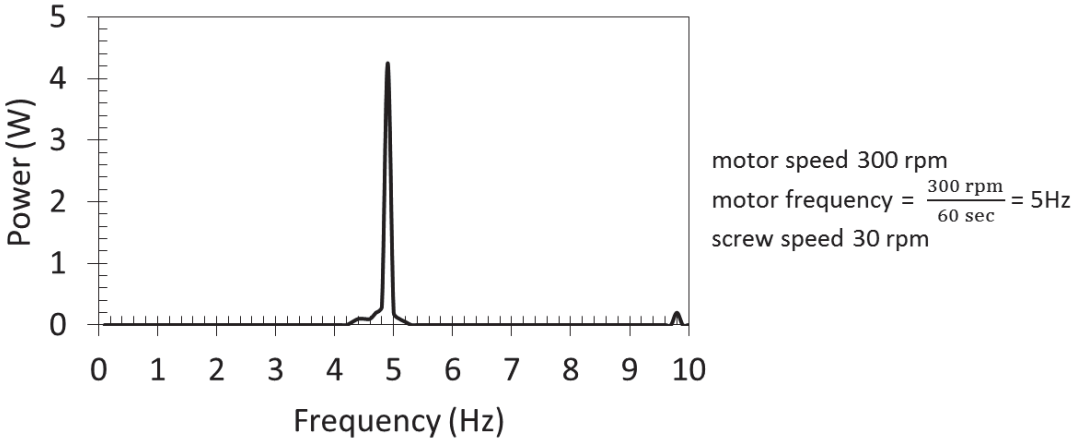

Figure 6.8. FFT performed on the torque sensor signal to determine the applied high pass filter cutoff frequency.

The remaining Solid Plug model parameters which needed to be measured during the experimental trials were the feed screw speed and mass flow rate. The feed screw speed was measured using a digital tachometer (TONDAJ DT-2234C). For the experimental trials the screw speed was initially set to 30 +/-0.3 rpm. The screw speed was not continuously measured but was measured intermittently during testing. Fluctuations of 1-2 rpm were observed.

Lastly, the Solid Plug model requires the mass flow rate, which was experimentally measured by collecting material exiting the feeder on a laboratory balance (Mettler Toledo SB 8001). The balance was connected to a computer that used a LabView program to gather the balance readout as a function of time and plotted the mass flow rate. The precision of the scale was 0.1 grams and the measurement was at a rate of 5.5 Hz, which was the maximum sampling rate of the balance. The relative uncertainty of the mass flow rate is calculated in Appendix B.

For each experimental trial, first the feed screw speed was set to 30 rpm. Next, the motor was turned off and the plug at the feeder outlet was put into place. The hopper

was then filled by adding approximately 50 grams of microcrystalline cellulose (Avicel PH 102) at a time. Care was taken to minimize the height above the hopper from which the material was poured. This was done in order to replicate the conditions under which the feeder inlet stress was measured (Chapter 5). Once the hopper was filled, the load cell, torque sensor, and balance were set to record data. The motor of the feed screw drive system was turned on, with the screw speed still set to 30 rpm. At this point, all instruments started recording data. The experimental trial was run till the hopper was emptied, then all instruments which were recording data were stopped and the motor was turned off. After each trial, the feed screw was removed from the barrel and both the feed screw and barrel were cleaned to remove any compacted material. The material was discarded after each trial because jamming occurred at different conditions for reused material. This was attributed to the material losing compressibility after an experimental trial. Jamming conditions are discussed in Chapter 7. Three experimental trials were performed for each plug size.

The raw data, which was recorded by the balance, load cell, and torque sensor, are shown in Figures 6.9 – 6.11, respectively. The results that are shown in the following chapters for mass flow rate, feeder outlet stress, and feeder torque are the steady state values. The steady state has been defined as the point at which the measured quantity changes by less than 20% for a period of 30 seconds. The region defined by steady state is marked in the plots below. Also shown in Figures 6.10 and 6.11 below is the scatter of the experimental measurements. The scatter of the experimental measurements is defined in the current work as +/- one standard deviation from the average steady state value. In

the following chapter the scatter of the experimental data will be compared to the uncertainty of the experimental measurements due to the sensitivity of the sensors.

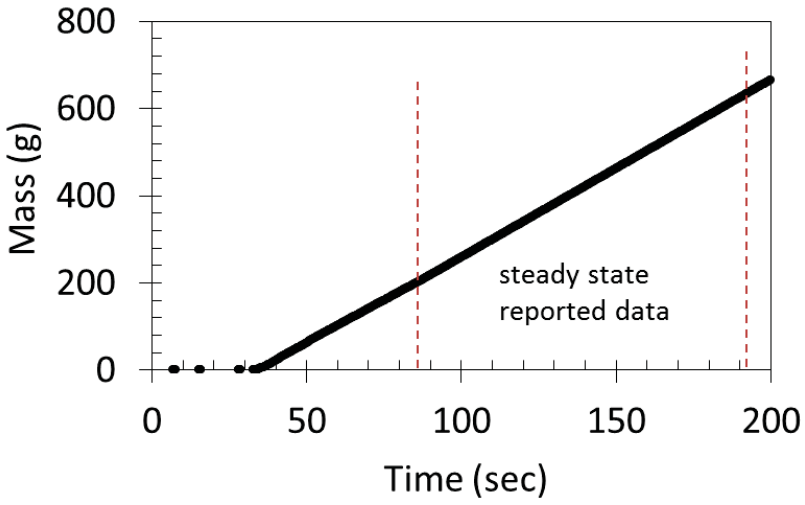

Figure 6.9. Example of the experimentally measured mass exiting the feeder as a function of time, illustrating the steady state mass flow rate range over which the results are collected.

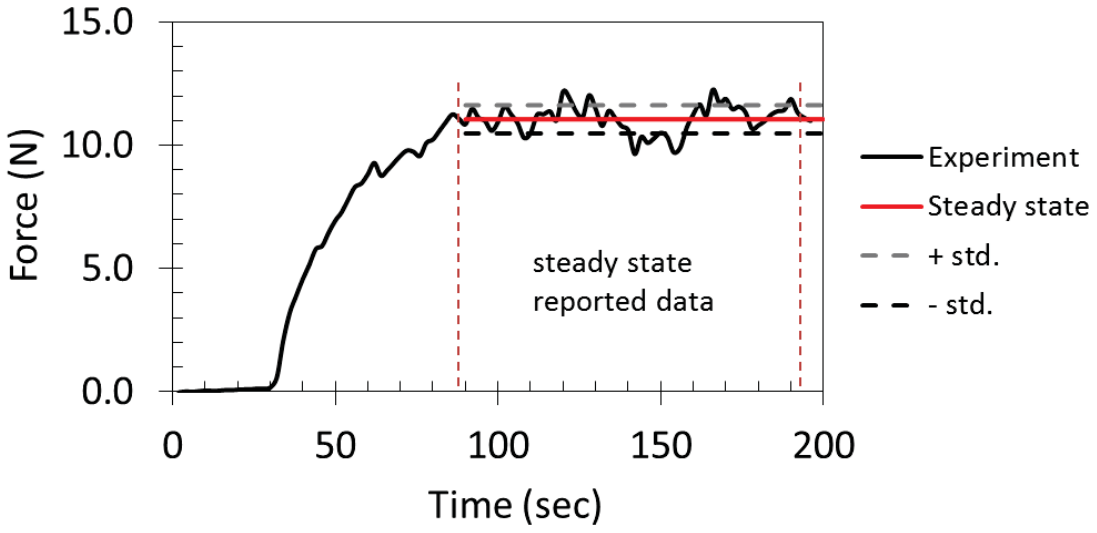

Figure 6.10. Example of the force experimentally measured by the load cell at the base of the plug, illustrating the steady state range from which the results are collected.

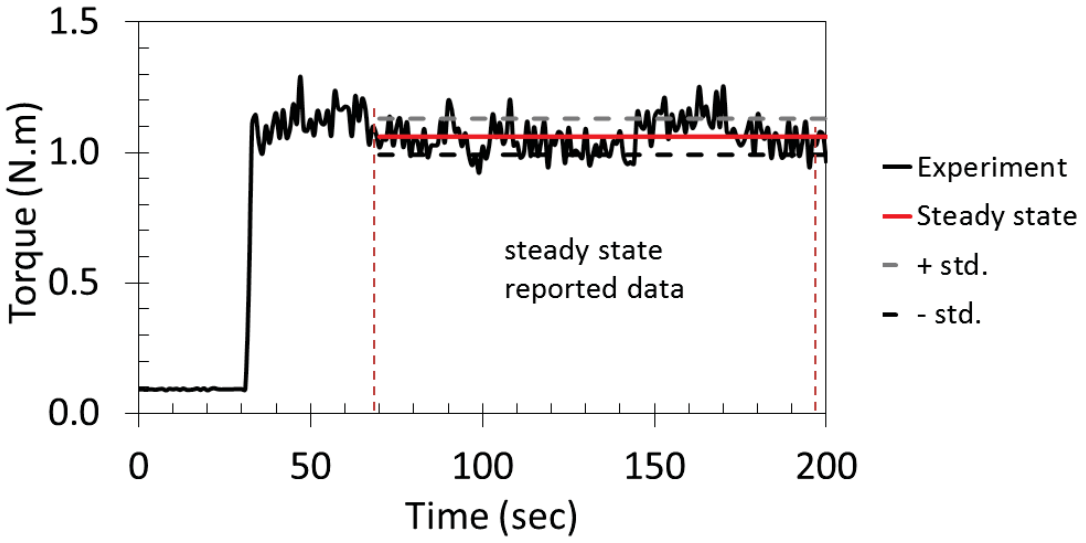

Figure 6.11. Example of the experimentally measured feeder torque, illustrating the steady state range from which the results are collected.

CHAPTER 7. COMPARISONS BETWEEN EXPERIMENTAL RESULTS AND THE SOLID PLUG MODELS

The experimental measurements of the feed screw mass flow rate, outlet stress, and torque are presented in this section. The discussion focuses on the comparisons between the Solid Plug models' predictions and experimental measurements. The Solid Plug model's outputs use the input parameters measured in Chapter 5. The Solid Plug models were iteratively solved by stepping along the feed screw in step sizes of Lp/1000 and applying the stress-density relationship at each step (Figure 4.5).

7.1 Experimental Observations

While performing experimental trials there were a number of notable observations:

1. The measured steady state values of the mass flow rate, feeder outlet stress, and feeder torque were independent of the hopper fill level. These values were only affected when the hopper emptied completely, affecting the screw channel fill level.
2. As long as the face of the plug was inserted past the plane of the barrel outlet, the plug insertion depth had no effect on the outlet stress or torque measurements.
3. When the same material was used in multiple experimental trials, the material's loss of compressibility increased the open outlet area value at which jamming occurred. Therefore, all of the experimental measurements reported are from

experiments performed with material that had not been previously used.

4. After the experimental trials a thin layer of material was observed to have formed along the bottom of the barrel. This layer of material was a result of there being a gap between the tip of the screw flights and the barrel surface.
5. The bulk density of the material was not observed to change much along the length of the feeder, except for within the last few screw flights (Figure 7.1). Up until the last few screw flights the material was observed to be free flowing. A clam shell barrel was used to allow observations of the material compaction in just a few experiments for this purpose. In all other cases, the WP 120 Alexanderwerks Roll Compactor barrel was used.

These experimental observations suggest that the stress increase along the feeder length occurs primarily in the last few screw flights, and that the stress upstream due to the hopper fill level is less significant. It further indicates the importance of implementing a stress-density relationship in the Solid Plug model as opposed to assuming constant density along the barrel length.

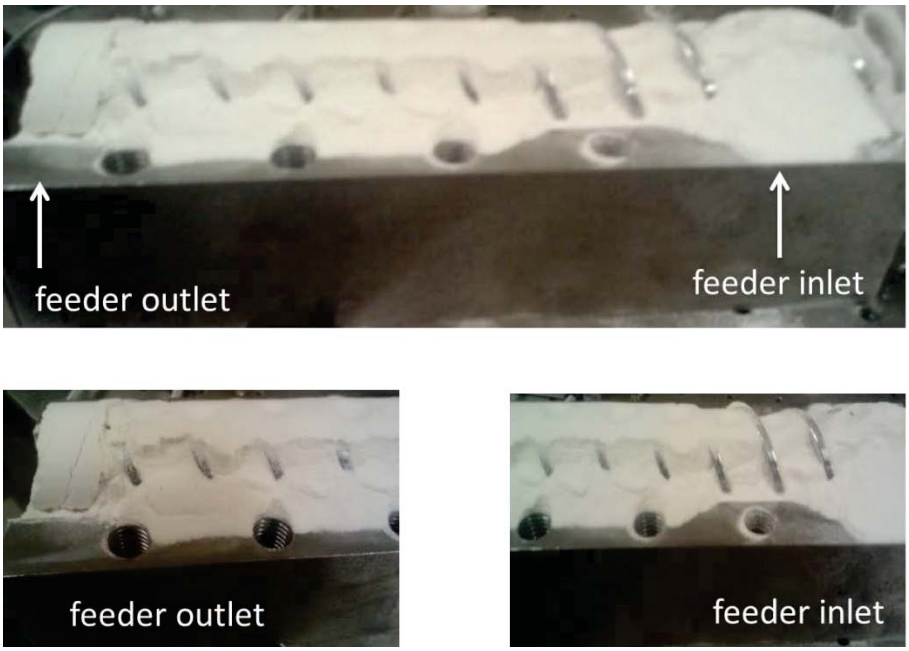

Figure 7.1. Image taken after removing the top of a clam shell barrel. The image shows material (Avicel PH 102) along the feeder length after an experimental trial. The material at the feeder outlet is compacted more significantly than the material at the feeder inlet.

7.2 Conveying Angle Verification

As previously shown (Chapter 4), the Solid Plug model relates the mass flow rate to the feeder outlet stress by the conveying angle. The mass flow rate-conveying angle relationship (Equation (4.27)) applied within the Solid Plug model was verified experimentally for open outlet conditions, i.e., no applied outlet stress (Figure 7.2).

The conveying angle was taken to be $\pi/2$, corresponding to the theoretical maximum mass flow rate expected when there is no applied outlet stress (Tadmor et al., 1972), and the material bulk density was taken as the poured bulk density (Avicel PH 102; 0.32 g/cm^3). The screw speed was then varied to generate different mass flow rates.

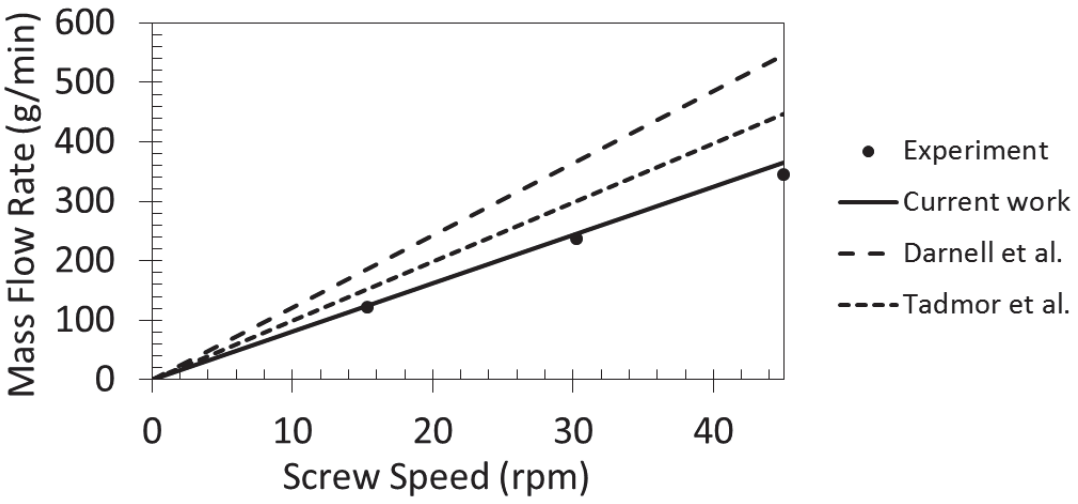

Figure 7.2. Comparison between the experimental and the theoretical mass flow rate for an open outlet condition. The assumptions of Darnell et al. (1956), Tadmor et al. (1972), and the current work are compared.

The three theories presented in Figure 7.2 vary in their assumptions of the screw channel cross-sectional areas (Figure 7.3). Darnell et al. (1956) takes the entire screw channel cross-sectional area, Tadmor et al. (1972) accounts for the screw flight thickness, and the current work accounts for both the screw flight thickness and the gap between the barrel and screw flights. The mass flow rate-conveying angle relationship (Equation (4.27)) only varies slightly between the three models. The height of the screw channel (H) is measured as the distance between the screw core and barrel in the work of Darnell et al. (1956) and Tadmor et al. (1972) whereas in the current work the channel height is taken to be the distance from the screw core to the screw flight tip. The difference in the screw channel heights is then the gap between the screw flights and barrel. Additionally, not accounting for the screw flight thickness simply means that the screw flight thickness is set to zero ($e = 0$).

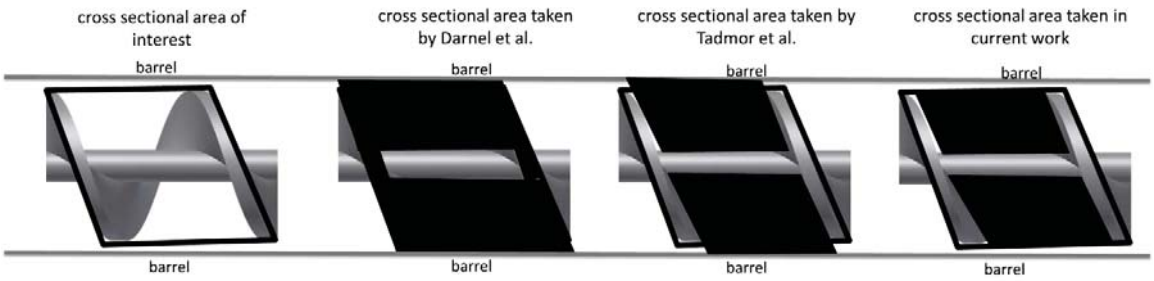

Figure 7.3. Moving left to right the images show the outlined screw channel cross-sectional area of interest, the screw channel cross-sectional area taken in the work of Darnell et al. (1956), the screw channel cross-sectional area taken in the work of Tadmor et al. (1972), and lastly the screw channel cross-sectional area taken in the current work. The blackened areas are the cross- sectional areas.

A relative error of less than 5% is observed when the mass flow rate-conveying angle relationship accounts for the screw flight thickness and the gap between the screw flights and barrel. The current work shows that the gap between the screw flights and barrel should not be neglected in this case. The relative error between mass flow rate-conveying angle relationship and experimental measurements increases as the screw speed increases, likely due to a decrease in the screw channel fill level. The screw channel fill level decreases as the screw speed increases because there is less time for the material to flow into the screw channel from the hopper (Moysey et al., 2004).

Such a simplistic equation to predict the mass flow can be an asset for continuous manufacturing in the pharmaceutical industry. Continuous manufacturing requires controllable and predictable mass flow rates of feeders for accurate dosing of formulation ingredients. This simplistic mass flow rate prediction does not, however, account for material flowability. A decrease in material flowability is expected to result in a decrease in the screw channel fill fraction due to the material flow in the hopper at the feeder inlet. Reduced fill fractions will cause the mass flow rate model to over-predict experimental

results because the mass flow rate model assumes completely filled screw channels. The material used for the experiments in this thesis (Avicel PH 102) had good flowability; therefore the assumption of completely filled screw channels is reasonable. However this assumption may not hold for materials with poor flowability. Thus, experimental measurements with materials of varying flowability are needed for complete validation of the mass flow rate model. If material flowability does affect the screw channel fill fraction, the material flowability could be accounted for in the mass flow rate model by incorporating the screw channel fill fraction.

7.3 Experimental Results

After verification of the mass flow rate-conveying angle relationship for an open outlet condition, the feeder mass flow rate, outlet stress, and torque were experimentally measured for restricted outlet conditions. Again, the feeder outlet was restricted by plugs of varying cross-sectional areas (Chapter 5). The plugs are meant to mimic the flow restrictions due to the rolls at the outlet of a roll compactor. Three experimental trials were performed for each plug cross-sectional area and the average steady state results from each trial are presented below.

7.3.1 Mass Flow Rate

While the range of experimentally measured mass flow rates has been presented in Chapter 5, the measurements are discussed here. As the open outlet area-to-barrel area ratio was reduced from 0.75 to 0.44 by using plugs of different cross-sectional areas, the mass flow rate reduced by approximately 10% from the open outlet condition mass flow

rate (Figure 7.4). These mass flow rates provided the mass flow rate range input into the Solid Plug model in order to predict the feeder outlet stress. The uncertainty of the mass flow rate measurements due to the uncertainty of the mass measured by the balance (+/- 0.1 g) and the uncertainty of the time kept by the CPU (+/- 0.0001 s) was on the order of 0.1 g/min (Appendix B). The uncertainty of the mass flow rate cannot be seen in Figure 7.4 because the mass flow rate is normalizing by the open outlet mass flow rate.

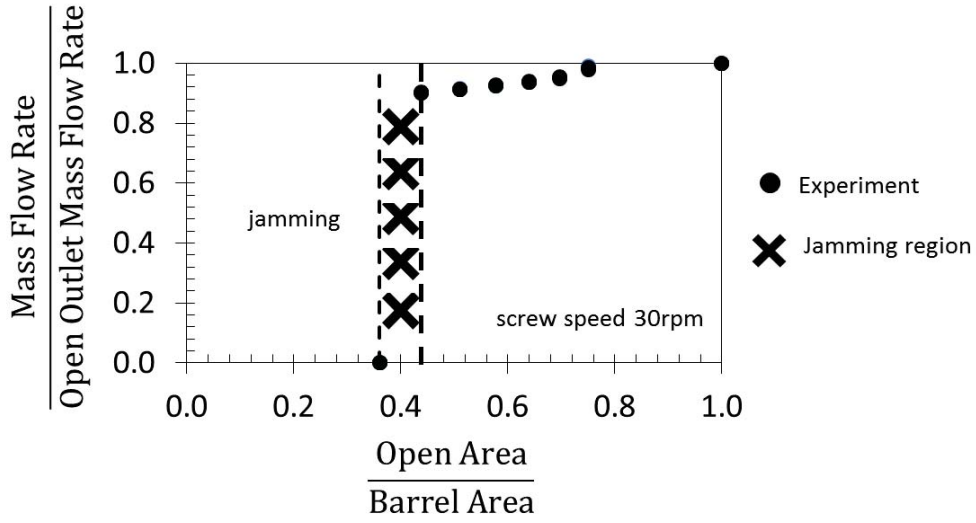

Figure 7.4. Experimentally measured mass flow rate as a function of the open outlet area-to-barrel area ratio. Jamming of the feeder outlet begins at an open outlet area-to-barrel area ratio with the jamming region. The exact open outlet area-to-barrel area ratio at which jamming occurs cannot be determined since the data is not continuous.

Note that the mass flow rate changes only slightly despite a wide range of open outlet areas (Figure 7.4). Further reduction of the open outlet area-to-barrel area ratio caused the feeder to jam. Jamming occurred when compacted material seized at the feeder outlet, reducing the mass flow rate to zero. The feeder torque would increase for the jammed state until reaching the maximum torque of the experimental setup at which

point the experiment was stopped. In order to extrude material at the jamming state, the torque capabilities of the experimental setup would need to be increased beyond the torque capacity of the device.

7.3.2 Feeder Outlet Stress

While it was shown that the experimentally measured was relatively insensitive to a decrease in open outlet area, until the feeder jammed, the opposite trend was observed for the feeder outlet stress. Shown in Figure 7.5 are the feeder outlet stress measurements from the three separate tests performed at each open area-to-barrel area ratio. The reduction of the open outlet area caused a rapid increase in the feeder outlet stress as the jamming state was approached. The span of experimental data was bounded by the jamming state of the feeder and the sensitivity of the load cell at the base of the plug.

The scatter of the experimental feeder outlet stress measurements (+/- one standard deviation) shown in Figure 7.5 is on the order of 0.5 kPa. Although it appears as though the scatter of the experimental measurements decreases as the outlet stress increases, the scatter remains relatively constant throughout the experimental measurements. The scatter appears to decrease due to the logarithmic scale. Also, the scatter of the experimental data is more significant than the uncertainty of the feeder outlet stress measurements, which varied from 0.02-0.3 kPa (Appendix B). Again, the uncertainties in the feeder outlet stress calculations result from the uncertainty of the measurements made by the load cell at the feeder outlet. In the experimental trials, only applied loads greater than 1.0 N were considered. An applied load less than 1.0 N was lower than the combined sensitivity limit of the load cell and scatter of the load cell

signal. The loads applied to the load cell exceeded this lower limit when the open outlet area –to-barrel area ratio was less than 0.64.

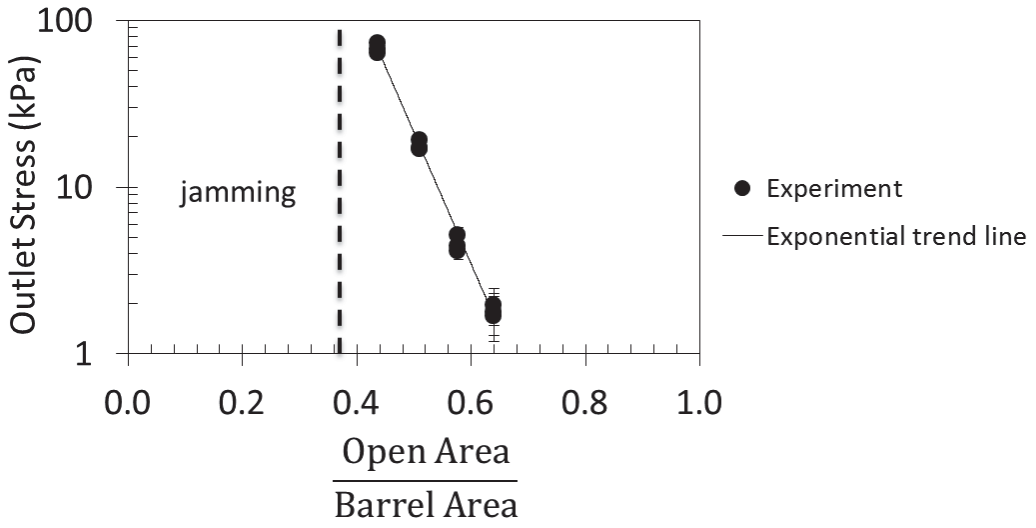

Figure 7.5. Experimentally measured feeder outlet stress as a function of the normalized outlet area.

In order to compare the experimental measurements with the outputs of the Solid Plug models, the feeder outlet stress was plotted as a function of the mass flow rate (Figure 7.6). The small decrease in mass flow rate and rapid increase in feeder outlet stress, resulting from the reduction in open outlet area, leads to a relationship where the feeder outlet stress is highly sensitive to the mass flow rate. Overall, a less than 10% reduction in the mass flow rate from the open outlet condition mass flow rate (i.e., no applied outlet stress) resulted in an increase of four orders of magnitude in the feeder outlet stress. The experimental results also follow an exponential trend, as predicted by the Solid Plug model. The variations in mass flow rate and feeder outlet stress between trials are most distinctly shown in Figure 7.6. The feeder outlet stress varies to a greater degree between trials as the outlet stress increases.

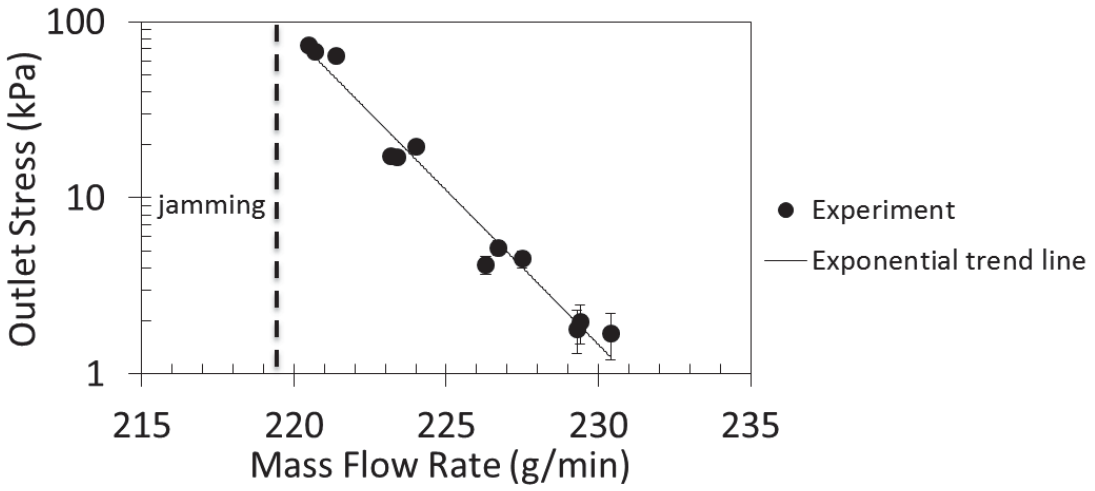

Figure 7.6. Experimentally measured feeder outlet stress as a function of the mass flow rate.

The feeder outlet stress predictions of the Solid Plug models developed by Tadmor et al. (1972), Campbell et al. (1995), and Hyun et al. (1997a), based on the input parameters defined in Chapter 5, are presented in Figure 7.7. The predictions shown were solved numerically by solving the algorithm in Figure 4.5 using WOLFRAM Mathematica 9.0. Along with the feeder outlet stress predictions of the Solid Plug models and the experimental results following an exponential trend, both are sensitive to the mass flow rate as well.

Over the same range of mass flow rates, the Solid Plug models' predictions and the experimentally measured feeder outlet stresses are different by several orders of magnitude. The Solid Plug models' predictions are orders of magnitude different from the experimental results because the Solid Plug models get the axial variation in the stress incorrect and predict a decrease in stress along the length of the feed screw. A Solid Plug model prediction where the stress decreases from the feeder inlet to the feeder outlet results from the retarding forces being greater than the conveying forces. Both the

conveying and retarding forces are affected by the friction coefficients and stress ratios. The Solid Plug models' predictions (Figure 7.7), then, suggest that the friction coefficients and stress ratios applied are incorrect (Chapter 5). The next chapter will focus on the sensitivity of the Solid Plug models to the friction coefficients and stress ratios.

The models' under-estimations of the experimental results by orders of magnitude are not demonstrated in the literature; however, the Tadmor model was shown to over-predict experimental results by orders of magnitude in the work of Fang et al. (1991). The work done by Hyun et al. (1997a) compared experimental results with the Solid Plug models of Darnell et al. (1956), Campbell et al. (1995), and Hyun et al. (1997a) with varying accuracy although all of the models were within 50% of the experimental results. The Hyun model predictions agreed best with the experimental results. The application of the Darnell model in the work of Hyun et al. (1997a) is identical to the application of the Tadmor model in the current work. The only difference between the models is that the Darnell model assumes the barrel and feed screw friction coefficients to be equal; this assumption was ignored in the work of Hyun et al (1997a).

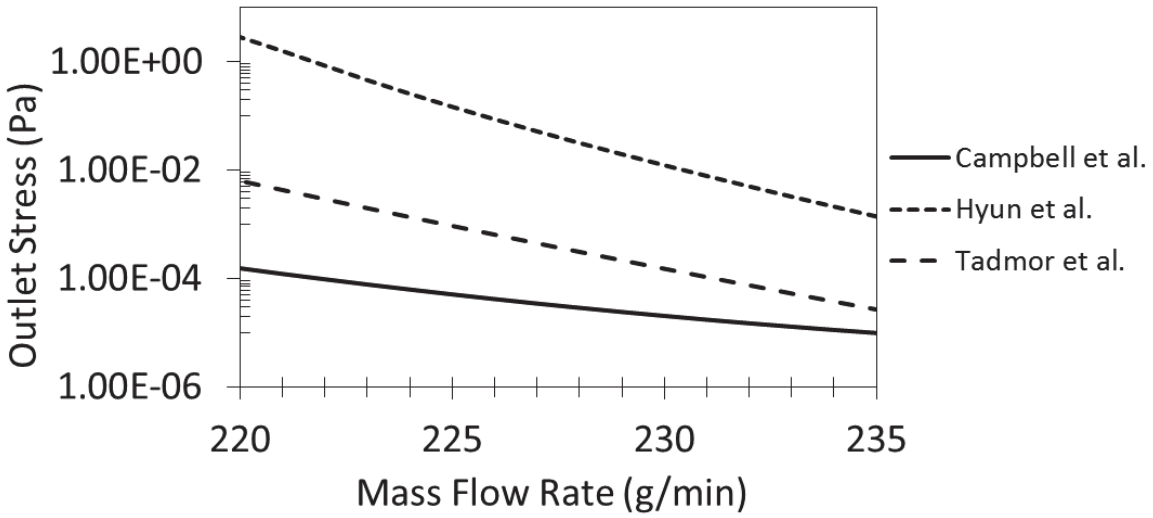

Figure 7.7. Solid Plug model predictions of the feeder outlet stress for the models developed by Tadmor et al. (1972), Campbell et al. (1995), and Hyun et al. (1997a) using the input parameters defined in Chapter 7 (k = 1). Note that the experimental data are at least four orders of magnitude larger than the model predictions and, hence, are not shown in the figure.

Briefly, to determine the effects of the assumed stress ratio of one, the stress ratio experimentally measured for Avicel PH 102 ($k = k_t = k_r = 0.22$) was applied to the Solid Plug models (Figure 7.8). There are two distinct differences in the Solid Plug models when applying the experimentally measured static stress ratio (k = 0.22) as opposed to a stress ratio of one: (1) the feeder outlet stress predictions increase by several orders of magnitude, and (2) the feeder outlet stress predictions sensitivity to the mass flow rate decreases. Still, when applying the experimentally measured stress ratio, the Solid Plug models poorly predict the experimental results by two orders of magnitude.

Although the stress ratios measured in punch and die experiments are shown to be constant (Es-Saheb, 1992; Michrafy et al., 2004) and the stress ratio applied to the Solid Plug model in the work of Hyun et al. (1997a) was held constant, the kinetic theory of granular materials showed that the stress ratio was dependent on the solid fraction when

the solid fraction was above 0.6 (Walton et al., 1986). The solid fraction at which the stress ratio decreases from a value of one may differ when comparing the simulations done by Walton et al. (1986) to the experimental work in this thesis, therefore the stress ratio may vary along the length of the feed screw from a value of one for small solid fractions to 0.22 for large solid fractions (Figure 7.1). Due to the potential variation of the stress ratio along the length of the feed screw, the sensitivity of the Solid Plug models to the stress ratios is discussed further in Chapters 8 and 10.

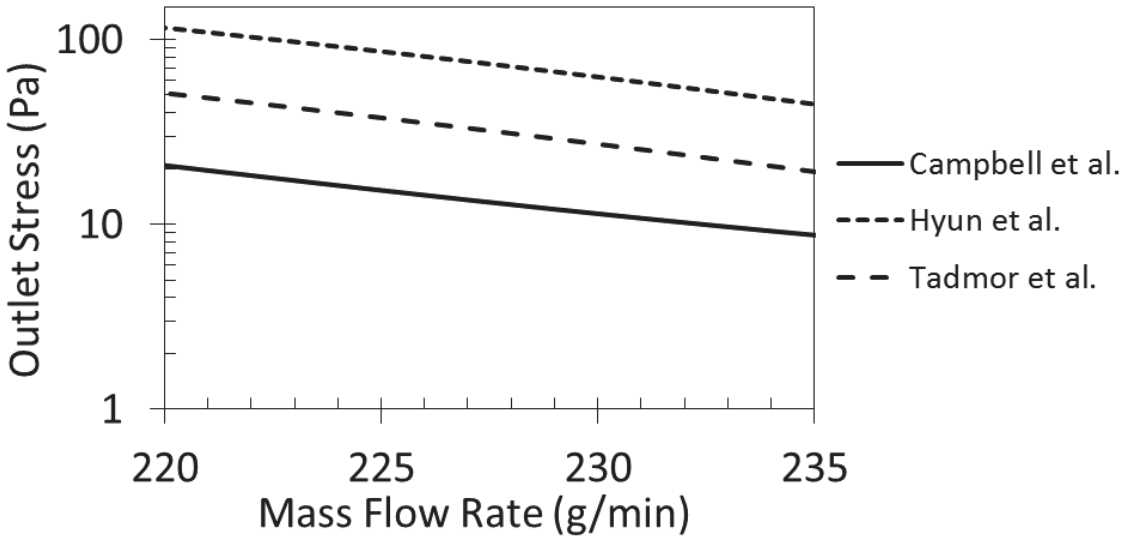

Figure 7.8. Solid Plug model predictions of feeder outlet stress for the models developed by Tadmor et al. (1972), Campbell et al. (1995), and Hyun et al. (1997a) using the experimentally measured stress ratio of 0.22. The experimental stress values are two orders of magnitude larger than the predictions and, hence, are not shown in the figure.

Finally, it should be noted that it was attempted to match the algorithm applied to the Solid Plug models in this work with the results presented in the literature (Lovegrove et al., 1984; Fang et al., 1991; Hyun et al., 1997a), however, none of these works provided a full set of defined parameters. The works of Lovegrove et al. (1984) and Fang et al. (1991) did not fully define the feed screw geometry, while the work of Hyun et al.

(1997a) did not provide sufficient information to determine the experimentally measured friction coefficients and material densities, which were temperature and stress dependent parameters applied to the Solid Plug models.

7.3.3 Feeder Torque-Outlet Stress Relationship

The experimental setup also captured the feeder torque-outlet stress relationship. The trend shown by the feeder torque as a function of the open outlet area (Figure 7.9) is similar to the trend shown by the feeder outlet stress. The feeder torque increases rapidly as the jamming state of the feeder is approached. Plotting the feeder torque as a function of the feeder outlet stress (Figure 7.10) exhibits a linear relationship, as predicted by the extended derivation of the Solid Plug model (Equation (4.41)). The quantitative predictions of the feeder torque-outlet stress relationship, though, are poor due to the Solid Plug model's inability to predict the feeder outlet stress.

The scatter of the torque measurements, which are easiest to observe in Figure 7.10, are +/- 0.1 N.m. The scatter was greatly diminished by applying the low pass filter to eliminate the noise from the motor (Chapter 6). Like the scatter of the feeder outlet stress measurements, the scatter of the torque measurements was significantly greater than the uncertainty of the torque sensor which was +/- 0.001 N.m.

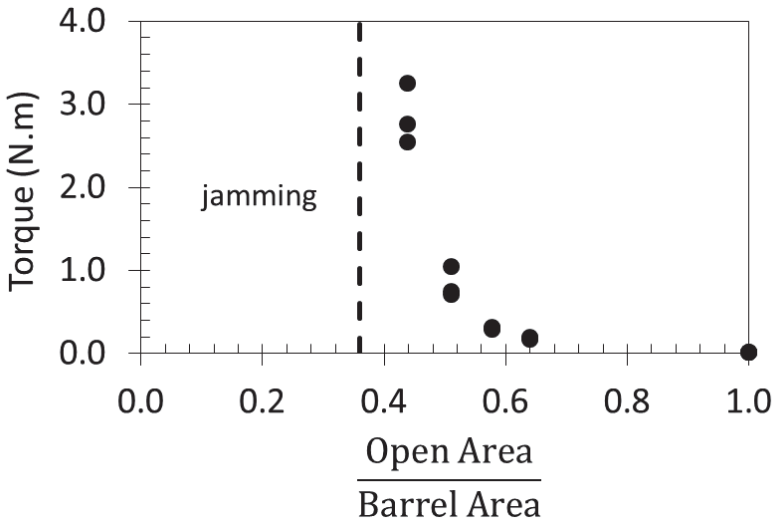

Figure 7.9. Experimentally measured feeder torque as a function of the normalized outlet area.

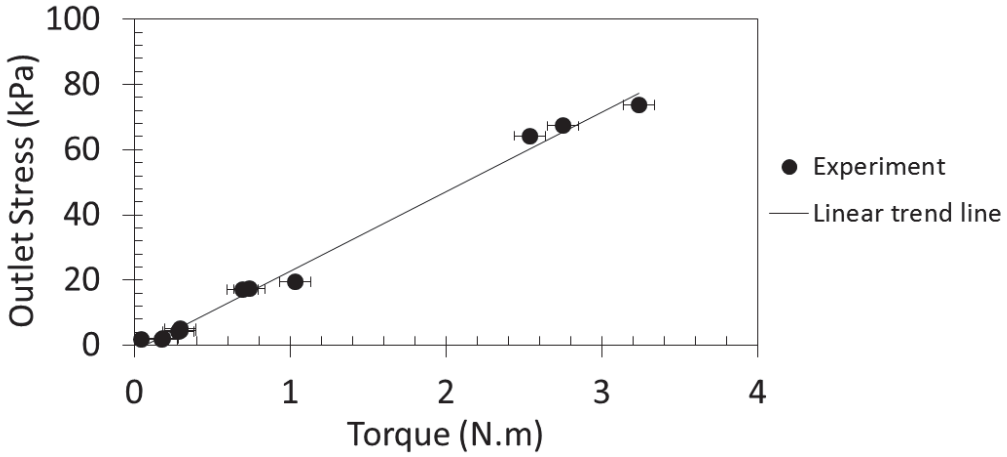

Figure 7.10. Experimentally measured feeder torque-outlet stress relationship.

Although the Solid Plug models are unable to predict the feeder outlet stress, the linear relationship between screw torque and feeder outlet stress could be used to determine the outlet stress by fitting the slope empirically and measuring the screw torque online. The roll inlet stress could then be input into roll compaction models to predict parameters such as roll force, roll torque, ribbon density, and nip angle.

Reasons for the large discrepancies between the experimental results and predictions of the Solid Plug models are discussed in the following chapters. Accurate predictions from the Solid Plug model would eliminate the need for any empirical fitting measurements. The sensitivity of the Solid Plug models to the material input parameters (stress ratios and friction coefficients) and the application of the stress-density relationship will be examined in the following chapter. Lastly, the Solid Plug models will be fit to experimental results to determine the necessary input parameters to predict the experimental results.

CHAPTER 8. THE SOLID PLUG MODELS' SENSITIVITY TO MATERIAL INPUT PARAMETERS

The sensitivity of the Solid Plug models developed by Tadmor et al. (1972), Campbell et al. (1995), and Hyun et al. (1997a) to the friction coefficients and stress ratios are presented in this chapter. The determination of the Solid Plug models' sensitivity to the friction coefficients is necessary due to the unknown surface finishes of the barrel and feed screw. Darnell et al. (1956) specifies that a material's friction coefficient can change by one third to one half based on the surface finish. The sensitivity of the Solid Plug models to the stress ratios is examined because, while the stress ratios at each of the boundaries (barrel, screw core, and screw flights) are assumed equal in the current work ($k_t = k_r$) and the work of Hyun et al. (1997a), Moysey et al. (2004) have shown through DEM simulations that the stresses at the boundaries are not equal. While the stress ratios at the leading screw flight and barrel were almost one, the stress ratios at the screw core and trailing screw flight were shown to be 0.8 and 0.36 (Moysey et al., 2004), where the stress ratio is the ratio of the stress at the specified boundary to the down channel stress. The sensitivity of the Solid Plug models to the friction coefficients and stress ratios was determined for 10% variations of the parameters. In this chapter, the friction coefficients and stress ratios were varied independently while all other input parameters are specified in Table 5.1.

8.1 Friction Coefficients

As previously stated, the barrel frictional force acts as a conveying force and the feed screw frictional force acts as a retarding force on the material in a feed screw. The expectations are then that an increase in the barrel friction coefficient or a decrease in the screw friction coefficient will increase the driving force, resulting in an increased feeder outlet stress prediction for a given mass flow rate. These expectations are not, however, followed when the barrel friction coefficient is varied (Figures 8.1), but are followed when the feed screw friction coefficient is varied (Figure 8.2). The results are discussed in the following sections.

8.1.1 Barrel Friction Coefficient

The trend shown by each Solid Plug model as the barrel friction coefficient varies is that the slope of the predicted feeder outlet stress curve changes (Figure 8.1). An increase in the barrel friction coefficient increases the slope and a decrease in the barrel friction coefficient decreases the slope. The fact that the slope of the feeder outlet stress curve depends on the barrel friction coefficient makes sense because the barrel frictional force acts at the conveying angle which depends on the mass flow rate. The Solid Plug models' sensitivity to the barrel friction coefficient is then dependent on the mass flow rate. Observing a greater span of mass flow rates than those experimentally measured showed that the Solid Plug models' sensitivity to the barrel friction coefficient does not grow unbounded because of the effects of the stress-density relationship, which will be highlighted in the next chapter.

The Tadmor and Campbell models are shown to become less sensitive to the barrel friction coefficient as the mass flow rate is reduced (Figure 8.1a and Figure 8.1c) whereas the Hyun model is observed to have the opposite response and is shown to be the most sensitive to the barrel friction coefficient (Figure 8.1b). At the lower end of the experimental mass flow rate range, the Hyun model feeder outlet stress predictions vary by an order of magnitude for a 10% variation in the barrel friction coefficient. The Tadmor and Campbell models' outlet stress predictions vary by less than a factor of two over the entire experimental mass flow rate range. In all cases, the Solid Plug models under-predict the experimental results by orders of magnitude when varying the barrel friction coefficient by 10%. However, the sensitivity of the Solid Plug models to the barrel friction coefficients is affected by the stress-density relationship and will be discussed in Chapter 9.

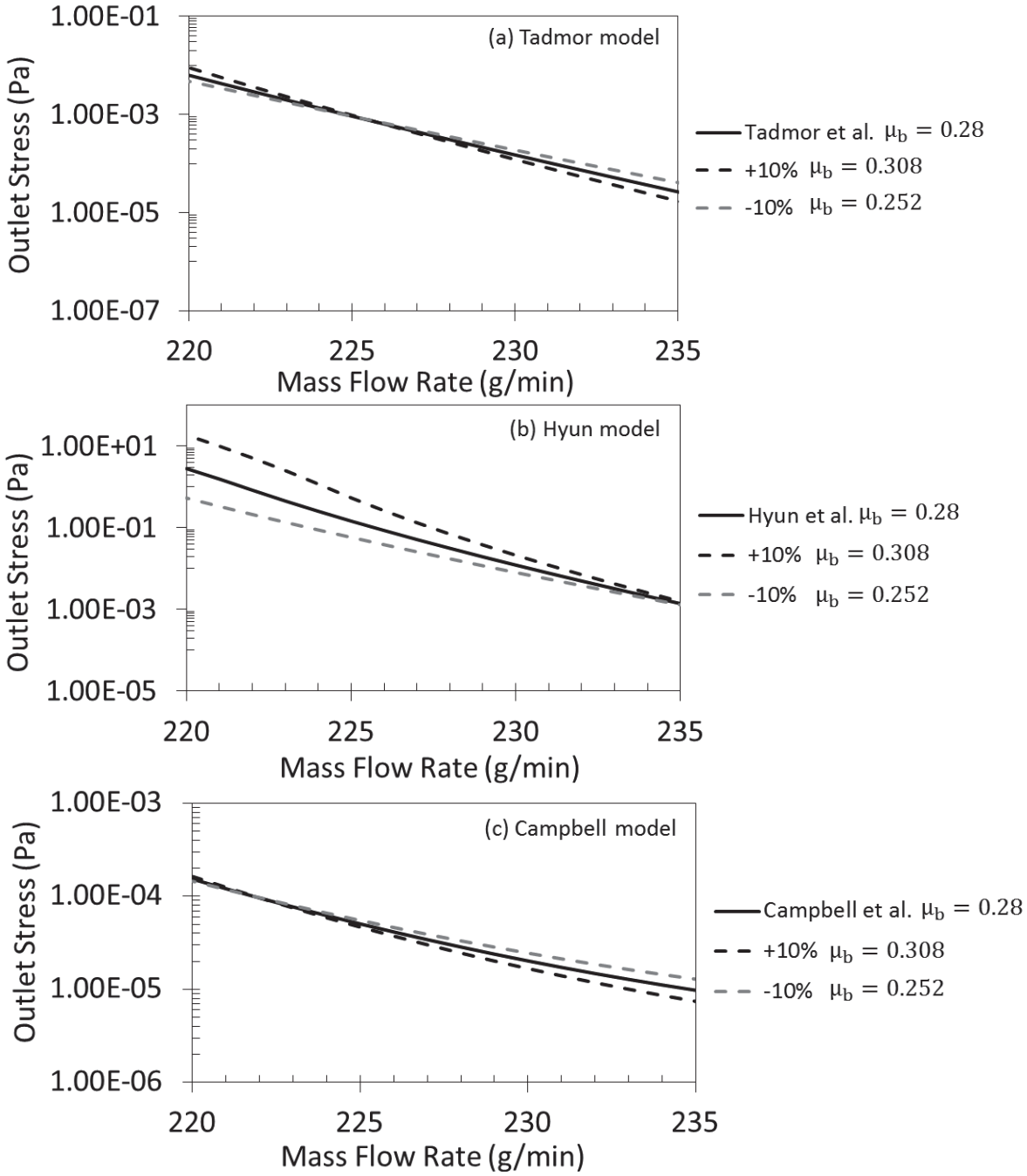

Figure 8.1. The sensitivity of the Solid Plug models to the barrel friction coefficient (μ_b) are shown by varying the barrel friction coefficients by 10%. The Solid Plug models are given the input parameters in Table 5.1 and the following values of the barrel friction coefficients $\mu_b = 0.28, \mu_b = 0.308,$ and $\mu_b = 0.252$.

8.1.2 Screw Friction Coefficient

Varying the screw friction coefficient is shown to result in a shift of the feeder outlet stress predictions (Figure 8.2). The Solid Plug models follow the expected trend that a decrease in the screw friction coefficient results in an increase in the feeder outlet stress while an increase in the screw friction coefficient results in a decrease in the feeder outlet stress, independent of the mass flow rate. The Solid Plug models are shown to be much more sensitive to the screw friction coefficient than the barrel friction coefficient. The sensitivity of each of the models is almost the same: a 10% change in the screw friction coefficient resulted in approximately an order of magnitude difference in the predicted feeder outlet stress.

The effects of the lower density limit applied to the stress-density relationship (Chapter 9) are observed in Figure 8.2b. At the lower end of the experimental mass flow rate range, a slight inflection in the feeder outlet stress predictions of the Hyun model occurs when the screw friction coefficient is decreased by 10% due to the lower density limit no longer affecting the Solid Plug model. The effects of the lower density limit on the Solid Plug models will be discussed further in Chapter 9. Although the Solid Plug models are sensitive to the screw friction coefficients, a 10% variation in the screw friction coefficient still leaves the Solid Plug models' feeder outlet stress predictions orders of magnitude below the experimental results.

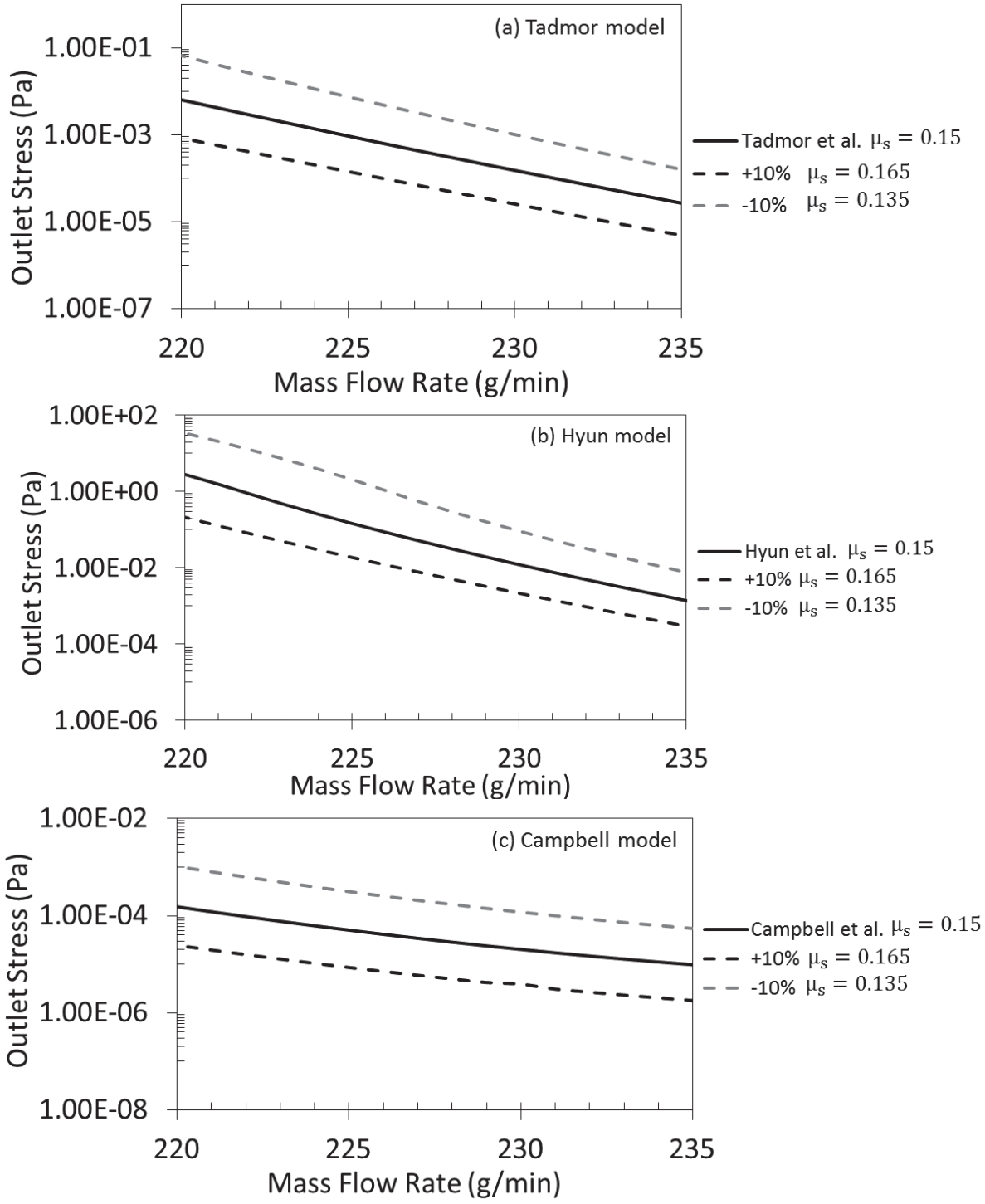

Figure 8.2. The sensitivity of the Solid Plug models to the screw friction coefficient (μ_s) are shown by varying the screw friction coefficient by 10%. The Solid Plug models are given the input parameters in Table 5.1 and the following values of the screw friction coefficient $\mu_s = 0.15, \mu_s = 0.165,$ and $\mu_s = 0.135$.

To conclude, the Solid Plug models developed by Tadmor et al. (1972), Campbell et al. (1995), and Hyun et al. (1997a) demonstrate similar trends due to changes in the barrel and screw friction coefficients, and are more sensitive to a variation in the screw friction coefficient than the barrel friction coefficient. In Figure 8.4 the barrel and screw friction coefficient values were each varied by 10% such that the changes in both friction coefficients contributed to the Solid Plug models, which results in better predicting the experimental results ($\mu_b = 0.308, \mu_s = 0.135$). While the feeder outlet stress predicted by each Solid Plug model increased by over an order of magnitude, there is still a difference of several orders of magnitude between the Solid Plug models and experimental results. Since the Solid Plug models are shown to be sensitive to the friction coefficients, the applied friction coefficients may not need to be varied by a significant amount in order for the Solid Plug models to predict the experimental results. The work of Darnell et al. (1956) discusses how surface finishes can cause drastic differences in friction coefficients. After discussing how varying the friction coefficients affects the stress-density relationship and how the stress-density relationship then affects the Solid Plug model predictions (Chapter 9), the Solid Plug models will be fitted to the experimental results to determine the necessary friction coefficients for the Solid Plug models to predict the experimental results.

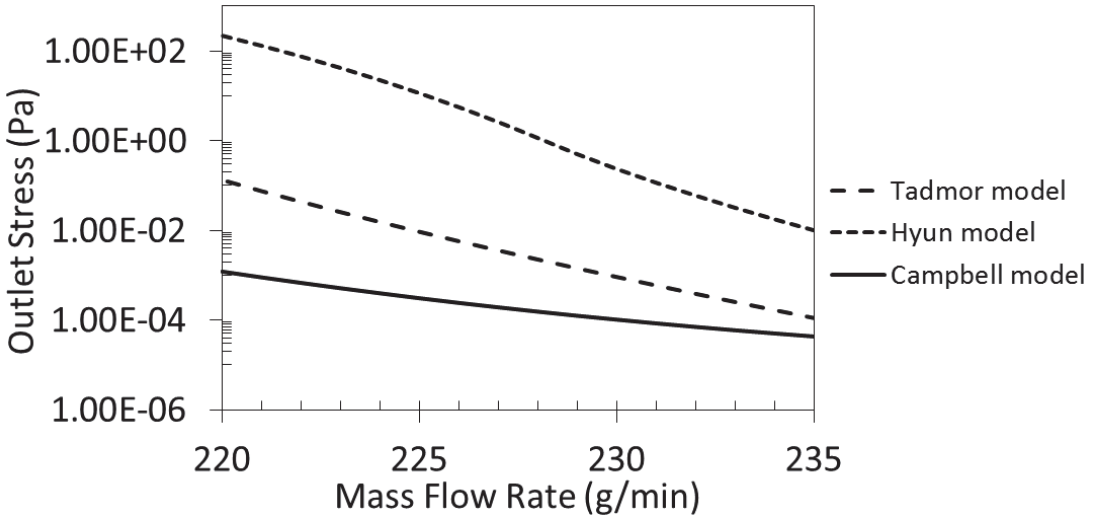

Figure 8.3. The Solid Plug models' feeder outlet stress predictions given the input parameters in Table 5.1 and varying the friction coefficients by 10%, so that $\mu_b = 0.308$ and $\mu_s = 0.135$.

8.2 Stress Ratios

Previously, the effects of applying the experimentally measured static stress ratio ($k_r = k_t = 0.22$) instead of the assumed stress ratio of one were shown ($k_r = k_t = 1$) (Chapter 7). This section looks at the assumption of equivalent stress ratios at the screw flights (k_t) and at the barrel and screw core surfaces (k_r). While the stresses have been assumed equivalent at the screw flights, barrel, and screw core by Darnell et al. (1956), Tadmor et al. (1972), Campbell et al. (1995), and Hyun et al. (1997a), the more recent DEM simulations performed by Moysey et al. (2004) have shown the stresses at the boundary surfaces to vary. The Solid Plug models' assumption that there is no variability in properties along the screw channel height or width leads to the assumption that the stresses at the boundary surfaces are equivalent. The feed screw DEM models (Moysey et al. 2004), on the other hand, do not assume the properties to be constant along the

screw channel height or width, and therefore were able to measure different stress values at each of the boundary surfaces (barrel, screw core, leading screw flight, and trailing screw flight). The ratio of stresses measured in the DEM simulations are different from the stress ratios given by a Mohr's circle. The stress ratios given by a Mohr's circle only apply for point loads and with only three principal stresses there can only be two stress ratios as defined by Mohr circle analysis.

Similar to the Solid Plug models sensitivity to the barrel friction coefficient, the stress ratio applied at the barrel and screw core surfaces is expected to affect the slope of the feeder outlet stress curve because the stress at the barrel acts at the conveying angle (Chapter 4). A decrease in the stress ratio at the screw core and barrel surfaces is expected to decrease the slope of the feeder outlet stress curve while an increase in the stress ratio is expected to increase the slope. From the Solid Plug model derivations, increasing the stress ratio at the screw flights will increase the retarding force and decrease the predicted feeder outlet stress, while the opposite is true if the stress ratio at the screw flights is decreased. The sensitivity of the Solid Plug models to the stress ratios, $k_r$and k_t, are shown below by varying the stress ratios, independently, by 10% from the assumed stress ratio of one (Figure 8.4). The sensitivity of the Solid Plug models to the stress ratios will determine the effect of the work by Moysey et al. (2004) on the Solid Plug model literature, and the need to define the stress ratios uniquely.

8.2.1 Stress Ratio Applied at the Screw Core and Barrel Surfaces (k_r)

As expected, the Solid Plug models' sensitivities to the stress ratio applied at the barrel and screw core surfaces (Figure 8.4) were similar to the Solid Plug models'

sensitivities to the barrel friction coefficient (Section 9.1.1). The sensitivity of the Solid Plug models to the stress ratio does differ, however, from the Solid Plug models sensitivity to the barrel friction coefficient because the stress ratio also affects the stress at the screw core. The variation in the stress ratio at the screw core surface causes a shift in the feeder outlet stress predictions, where a decrease in the stress ratio decreases the retarding forces and shifts the feeder outlet stress predictions up. The opposite is true for an increase in the stress ratio. This trend causes the Solid Plug models to be less sensitive to the stress ratio applied at the barrel and screw core surfaces than the barrel friction coefficient (Figure 8.4).

Over the experimental mass flow rate range each of the Solid Plug models shows a different sensitivity to the stress ratio applied at the barrel and screw core surfaces (Figure 8.4). While the Tadmor and Campbell models sensitivity to the stress ratio decreases as the mass flow rate decreases (Figure 8.4a and 8.4c), the Hyun model's sensitivity decreases to a minimum (231 g/min) and then begins to increase (Figure 8.4b). Looking at a wider mass flow rate range, all of the Solid Plug models' sensitivities to the stress ratio decrease to a point and then increase due to the change in slope caused by varying the terms which incorporate the conveying angle (Chapter 4). Over the experimental mass flow rate range, a 10% variation in the stress ratio at the barrel and screw core surfaces varied each of the models by at most a factor of three.

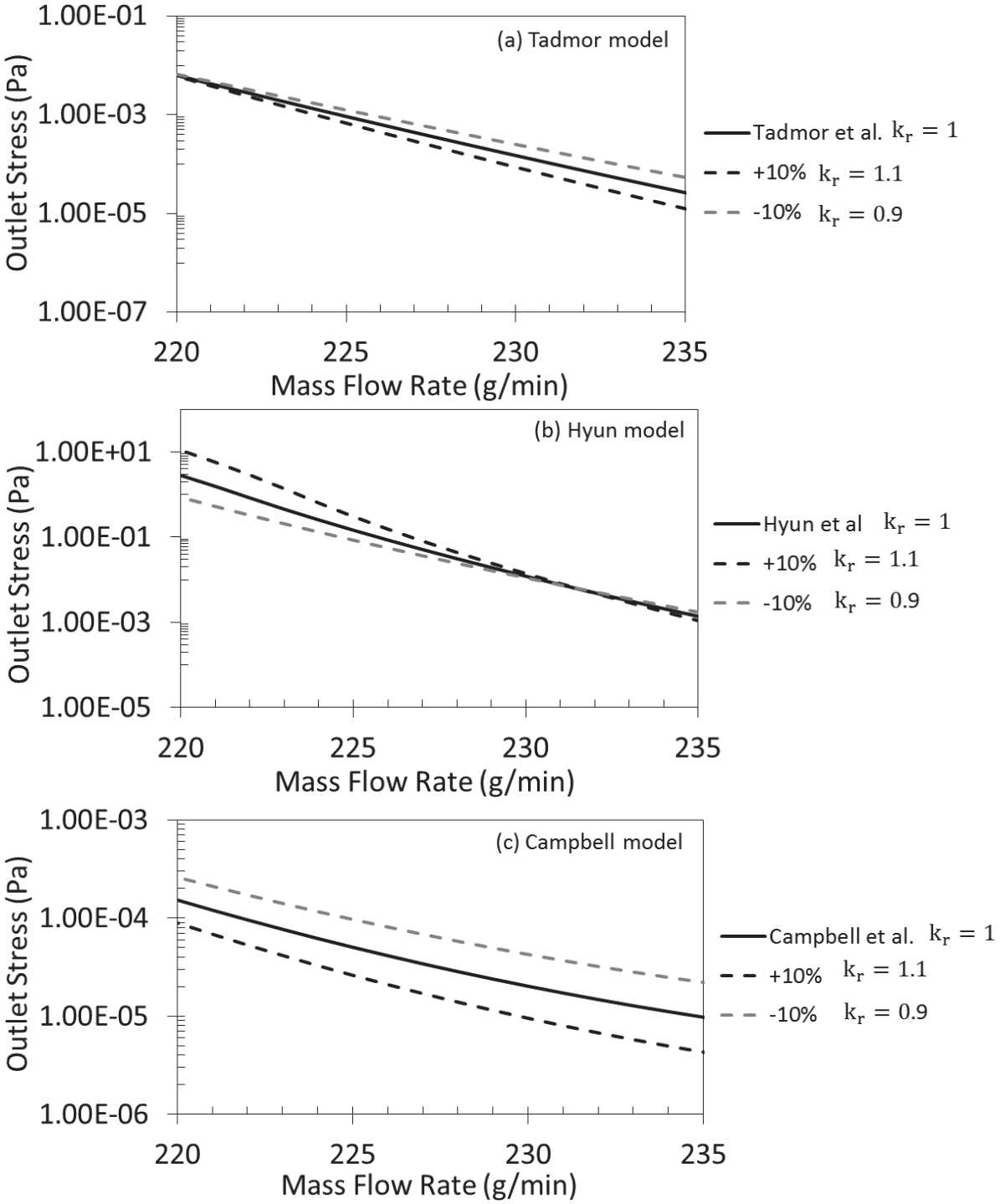

Figure 8.4. The sensitivity of the Solid Plug models to the stress ratio applied at the screw core and barrel surfaces (k_r) are shown by varying the stress ratio by 10%. The Solid Plug models are given the input parameters in Table 5.1 and the following values of the stress ratio $k_r = 1.0, k_r = 1.1, \text{and } k_r = 0.9$.

8.2.2 Stress Ratio Applied at the Screw Flights (k_t)

The last material parameter investigated was the stress ratio applied at the screw flights. Since the stress ratio at the screw flights did not affect any forces which acted at the conveying angle, a variation in the stress ratio at the screw flights only shifted the feeder outlet stress predictions (Figure 8.5) and did not affect the slope of the feeder outlet stress curve. An increase in the screw flight stress ratio decreased the feeder outlet stress predictions, while a decrease in the screw flight stress ratio increased the outlet stress predictions. While each of the Solid Plug models demonstrated a shift in feeder outlet stress predictions with a variation in the screw flight stress ratio, the magnitudes of the shifts varied. A 10% variation in the screw flight stress ratio caused the feeder outlet stress predictions of the Hyun, Tadmor, and Campbell models to vary by a factor of eight, three, and two, respectively. The sensitivity of the Solid Plug models to the stress ratio applied at the screw flights is expected to vary because one of the main differences between the Solid Plug models is the assumptions and applications applied to the force at the leading screw flight (Chapter 4).

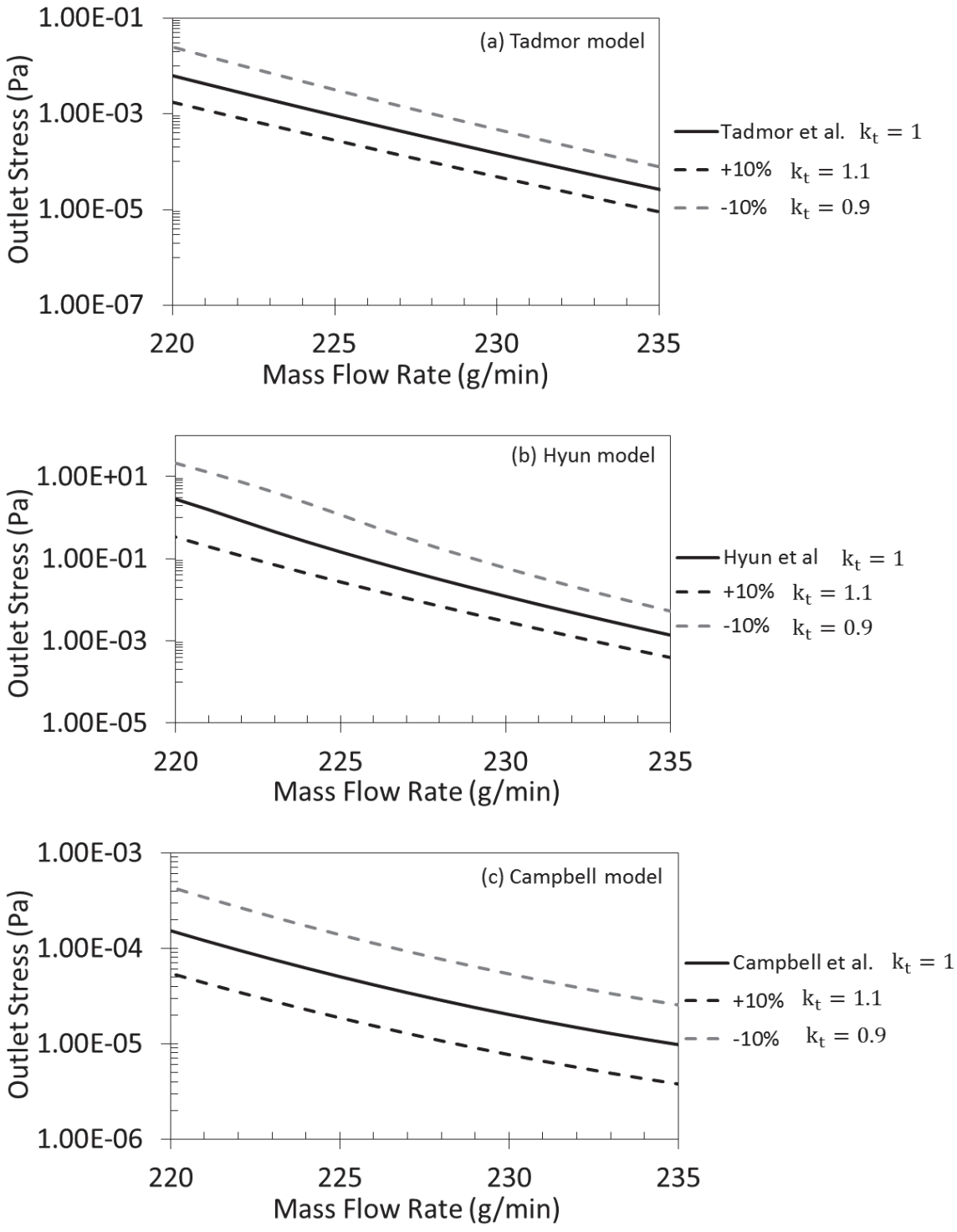

Figure 8.5. The sensitivity of the Solid Plug models to the stress ratio applied at the screw flights (k_t) are shown by varying the stress ratio by 10%. The Solid Plug models are given the input parameters in Table 5.1 and the following values of the stress ratio $k_t = 1.0, k_t = 1.1, \text{and } k_t = 0.9$.

8.3 Conclusion

In this chapter it was shown that although the Solid Plug models are sensitive to the material input parameters, 10% variations in the parameters still result in the under-estimation of the experimental results by orders of magnitude because the Solid Plug models' predictions of the feeder outlet stress, given the initial input parameters in Chapter 5, are so far from the experimental results. Greater variations in the initial material input parameters are necessary for the Solid Plug models to approach the experimental results. Variations in either the barrel friction coefficient or the stress ratio applied at the barrel and screw core surfaces were shown to affect the slope of the feeder outlet stress curve, and varying the screw friction coefficient or stress ratio at the screw flights were shown to shift the feeder outlet stress predictions. Which Solid Plug model is most applicable to the current work for predicting the outlet stress of a powder feed screw becomes apparent when fitting the Solid Plug models to the experimental results in Chapter 10. The sensitivity of the models to the various parameters is obviously a major part of fitting the Solid Plug models to the experimental results, but so too is the stress-density relationship, which is discussed in the next chapter.

CHAPTER 9. STRESS-DENSITY RELATIONSHIP

The stress-density relationship applied to the Solid Plug models was experimentally measured using an FT4 rheometer and the results were shown in Chapter 5. The method of applying the stress-density relationship to the Solid Plug models is shown in a flow chart in Figure 4.5. First, the feeder inlet stress is applied to the stress-density relationship to determine the inlet density and the calculated inlet density is then input into the mass flow rate-conveying angle relationship (Equation (4.27)) to determine the conveying angle. Next, the conveying angle is input into the Solid Plug model (Equation (4.20)) to predict the feeder stress an axial distance ($\mathrm{dL} = \mathrm{Lp}/1000$) downstream. Lastly, the calculated stress is input back into the stress-density relationship and the process continues until the feeder outlet is reached.

In addition to applying the stress-density relationship, a lower density limit was set within the stress-density relationship. A lower density limit resembles real powder behavior, where at some point decreasing the stress acting on the powder has no effect on the powder's density, but instead the powder's density is determined by the apparent density and other characteristics of the powder (i.e., uncompacted density of the material). The lower density limit was set equal to the poured bulk density of the material (0.32 $\mathrm{g/cm^3}$) and prevented unrealistic densities from being predicted. If the Solid Plug models predicted a stress along the feeder length that when input into the stress-density

relationship resulted in a density lower than the lower density limit, the density would be overridden and set as the lower density limit (Figure 4.5). The lower density limit is not necessary in instances where the Solid Plug model predicts an increase in stress from the feeder inlet to the feeder outlet. However, in the current work (Chapter 8), the Solid Plug model predicts a decrease in stress from the feeder inlet to the feeder outlet.

If the lower density limit was reached, the iterative process to determine the feeder outlet conditions would continue. Yet, once the lower density limit was reached, the Solid Plug models would not predict a stress increase such that the density would increase above the lower density limit. Therefore, once the lower density limit was reached, the density along the rest of the feeder length remained constant. This chapter discusses how the stress-density relationship, in particular the lower density limit, affects the feeder outlet stress predictions of the Solid Plug models and how the stress-density relationship is affected by the input parameters of the Solid Plug models.

In Figure 9.1 the Solid Plug models' predictions of the stress and material density at the feeder outlet, given the input parameters in Table 5.1, are shown. The predicted material densities at the feeder outlet equal the lower density limit over the entire experimental mass flow rate range. Without the lower density limit, the material density would decrease and the predicted feeder outlet stresses would be further from the experimental results. The predicted stress becomes so low that the stress-density relationship would predict negative densities, which was the reason for implementing the lower density limit. The inability of the Solid Plug models to predict the material density increase at the feeder outlet goes hand in hand with their failure to predict the feeder outlet stress.

One thing to note about Figure 9.1 is that although the predicted material density at the feeder outlet is constant, the feeder outlet stress decreases with increasing mass flow rate. This behavior is due to the change in mass flow rate and the stress-density relationship. As the mass flow rate is decreased, the feeder outlet stress increases and the point at which the lower density limit is reached shifts further downstream along the feeder (Figure 9.2). Due to the iterative method in which the Solid Plug models are solved, the point at which the lower density limit is reached affects the stress-density relationship. The further from the feeder inlet the lower density limit is reached, the greater the predicted feeder outlet stress, because a greater portion of the density along the feed screw is higher than the lower density limit. Also note that although the feeder outlet stress is increasing, it is still below the feeder inlet stress (200 Pa), which is why the lower density limit is reached (Figure 9.1). This result shows how the stress-density relationship plays a role when input parameters of the Solid Plug models are changed.

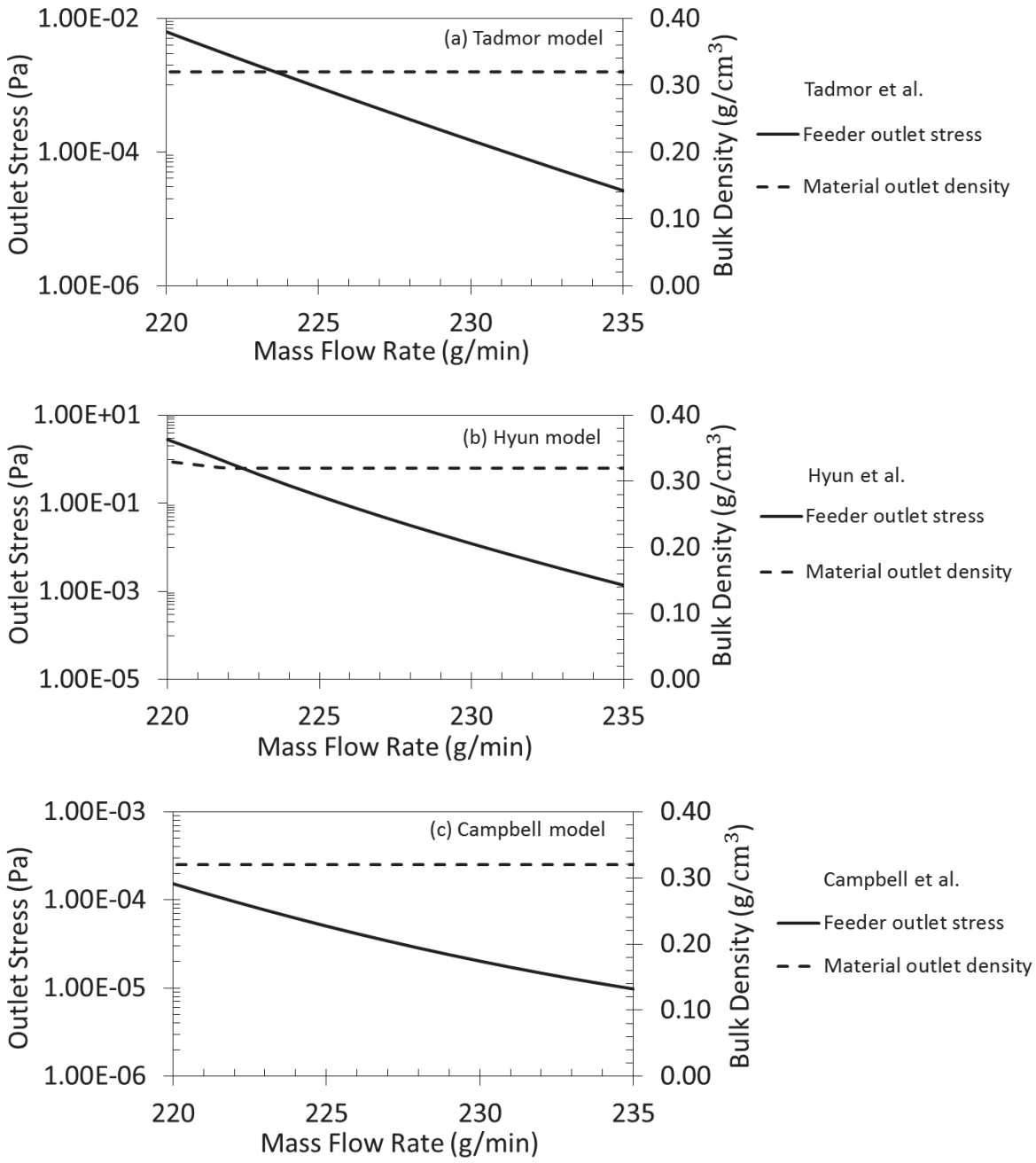

Figure 9.1. Feeder outlet stress and material outlet density predictions made by the Solid Plug models given the input parameters in Table 5.1.

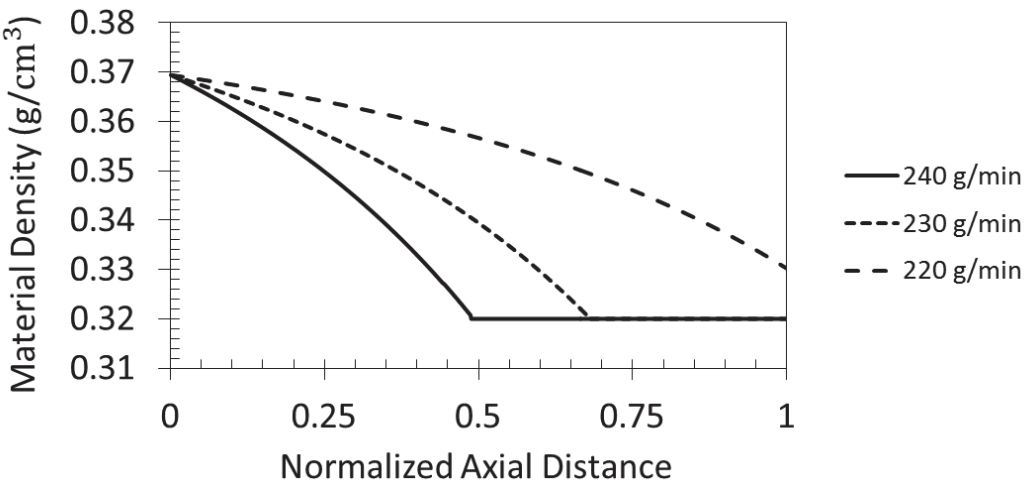

Figure 9.2. The predicted material density along the length of the feed screw for different mass flow rates, 240, 230, and 220 g/min, given the input parameters in Table 5.1. The figure shows that the lower density limit (0.32 g/cm^3) is reached at different locations along the feed screw for different mass flow rates.

If the friction coefficients or stress ratios are adjusted from those initially given (Table 5.1) such that the Solid Plug model predicts an increase in stress from the feeder inlet to the feeder outlet, the lower density limit is no longer reached and the effects of the stress-density relationship on the Solid Plug model can be observed. By varying the barrel friction coefficient, the effects of the stress-density relationship on the Solid Plug model are demonstrated in Figure 9.3. As the material density initially increases above the lower density limit (Figure 9.3a), the feeder outlet stress predictions are shown to rapidly increase causing the Solid Plug model to exhibit even greater sensitivity to the mass flow rate (Figure 9.3b). Additionally, due to the logarithmic trend fitted to the stress-density relationship ($\rho(\sigma)/\rho_b = 0.029 * \log(\sigma/\sigma_0) + 1.154$), the trend of the Solid Plug model changes and no longer follows an exponential trend once the density becomes greater than the lower density limit (Figure 9.3). Finally, the point at which the predicted density becomes greater than the lower density limit shifts to a higher mass

flow rate as the increase in barrel friction coefficient causes the feeder outlet stress predictions to increase (Figure 9.3a). A variation to any of the friction coefficients or stress ratios will cause a shift in the point where the predicted density becomes greater than the lower density limit.

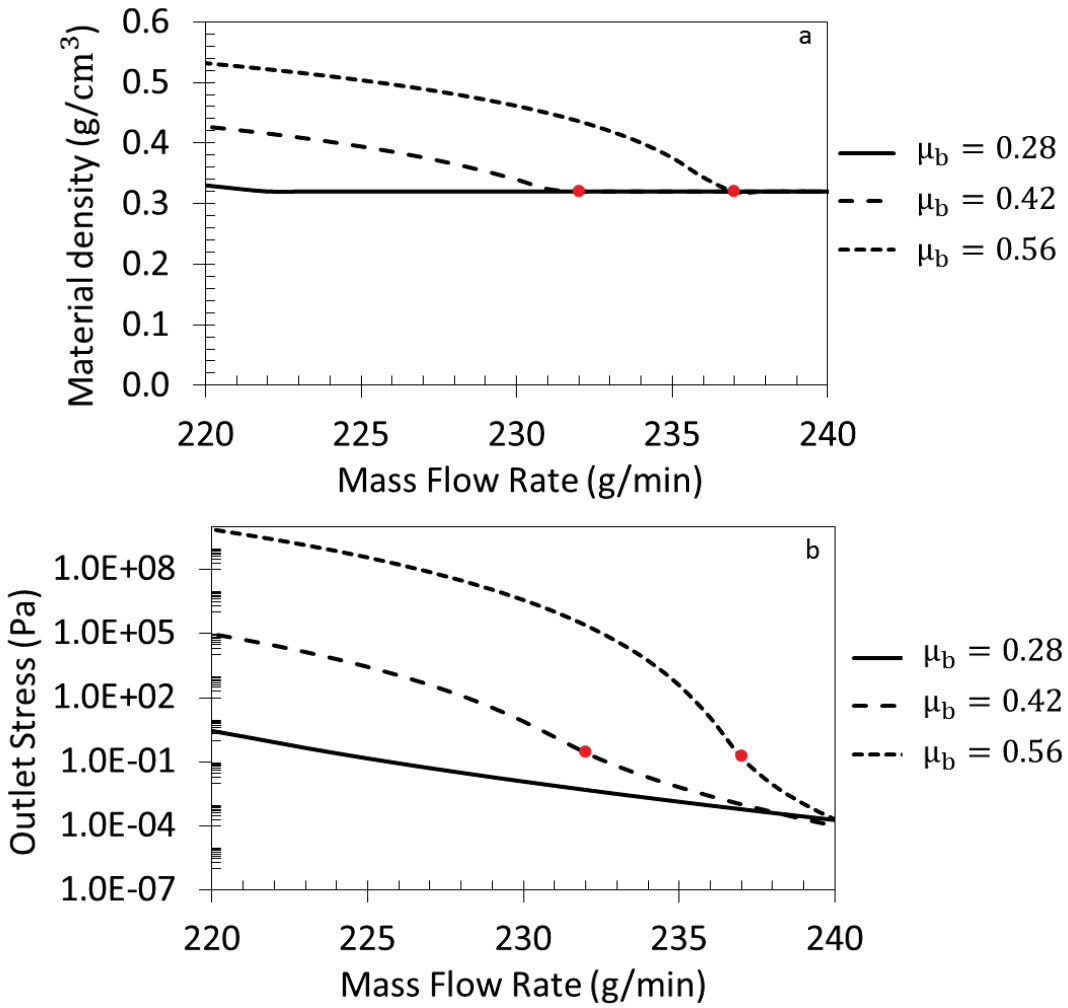

Figure 9.3. The Solid Plug model material density (a) and stress (b) predictions at the feeder outlet given the input parameters in Table 5.1 and the specified barrel friction coefficients. Highlighted are the points where the Solid Plug model no longer predicts the lower density limit.

In conclusion, the Solid Plug models' poor predictions of the feeder outlet stress, given the input parameters in Table 5.1, result in predictions of the density at the feeder outlet equaling the lower density limit. Without the application of the lower density limit, the feeder outlet stress predictions would decrease further and the density predictions would be non-sense. However, varying the friction coefficients or stress ratios such that they increase the predicted feeder outlet stress (Chapter 8) causes the stress-density relationship to effect the Solid Plug model predictions. Varying the material input parameters and the stress-density relationship, therefore, will both play a role in fitting the Solid Plug models' predictions to the experimental results (Chapter 10).

CHAPTER 10. FITTING THE SOLID PLUG MODELS TO EXPERIMENTAL RESULTS

The Solid Plug models have been shown to poorly predict the experimental results given the input parameters in Table 5.1 (Chapter 7), but both the experimental results and the Solid Plug models showed an exponential relationship between the feeder outlet stress and the mass flow rate. Additionally, the feeder outlet stress was shown to be highly dependent on the mass flow rate in both the experimental and Solid Plug model results. This chapter uses the friction coefficients (Section 10.1) and stress ratios (Section 10.2), independently, to fit the Solid Plug models to the experimental results.

The reason the friction coefficients and stress ratios are used as fitting parameters is because the friction coefficients could not be completely defined due to the surface finish of the feed screw and barrel being unknown, and the stress ratios were assumed to equal one (Darnell et al., 1956; Tadmor et al., 1972; Lun, 1991) and to be equal at all surfaces (barrel, screw core, and screw flights) (Darnell et al., 1956; Tadmor et al., 1972; Hyun et al., 1997a). The work of Darnell et al. (1956) showed that the surface finish of a material can vary the friction coefficient value by one third to one half, and the feed screw DEM simulations performed by Moysey et al. (2004) showed the stress ratios at each surface to vary. For these reasons the sensitivity of the Solid Plug models to the friction coefficients and stress ratios was discussed in Chapter 8. The analysis of the Solid Plug models sensitivity to the friction coefficients and stress ratios demonstrated

that in order for the Solid Plug models to fit the experimental results, the parameters would need to be significantly varied from those initially input (Table 5.1). The potential differences in the friction coefficients and stress ratios demonstrated by Darnell et al. (1956) and Moysey et al. (2004) are, however, great.

Below, the Solid Plug models are fitted to the experimental results using the friction coefficients (Section 10.1) and stress ratios (Section 10.2) by finding the least-squares fit. The least-squares fit is found by applying the FindFit function, which is built into Mathematica. The FindFit function requires as inputs the experimental results, the Solid Plug model equation, the Solid Plug model input parameters, and the variables which will be used as fitting parameters.

10.1 Fitting the Solid Plug Models to Experimental Results using the Friction Coefficients

This section gives the feed screw and barrel friction coefficients necessary to fit the Solid Plug models developed by Tadmor et al. (1972), Campbell et al. (1995), and Hyun et al. (1997a) to the experimental results (Figure 10.1). Apart from varying the friction coefficients, all other input parameters remained unchanged from those given in Table 5.1. As expected, the fitted friction coefficients varied significantly from the friction coefficients calculated based on the feed screw and barrel surface roughness values (Table 10.1). The differences between the measured and fitted friction coefficients are smallest for the Hyun model and largest for the Campbell model.

From the sensitivity analysis in Chapter 8, in order for the Solid Plug models to fit the experimental results, varying the barrel friction coefficient achieved the proper slope while varying the feed screw friction coefficient shifted the feeder outlet stress predictions to the correct magnitude. The fitted barrel friction coefficients for the Hyun, Tadmor, and Campbell models are similar whereas the feed screw friction coefficients vary to a greater extent between the models (Table 10.1), meaning that the models' predicted feeder outlet stress curves have similar slopes but differ in the magnitude of the feeder outlet stress predictions (Chapter 7).

All of the fitted friction coefficients of the Solid Plug models, except for the fitted feed screw friction coefficient of the Campbell model, varied by less than 50% from the measured friction coefficients (Table 10.1). Darnell et al. (1956) has shown that the surface finish of a material can affect the friction coefficient value by up to 50%. However, for the Solid Plug models to predict the experimental results the surface finish would need to affect both the feed screw and barrel friction coefficients such that they improve the Solid Plug models' predictions. A surface finish which produces a rougher barrel and a smoother feed screw are necessary to predict the experimental results. The feed screw friction coefficients required by the Tadmor and Campbell models to fit the experimental results are lower than the friction coefficient measured using the 0.05 μm wall friction sample (Chapter 5). Based on observations of the feed screw surface, it did not appear to be as smooth as the 0.05 μm wall friction sample. Overall, only the friction coefficients necessary to fit the Solid Plug model developed by Hyun et al. (1997a) to the experimental results are reasonable.

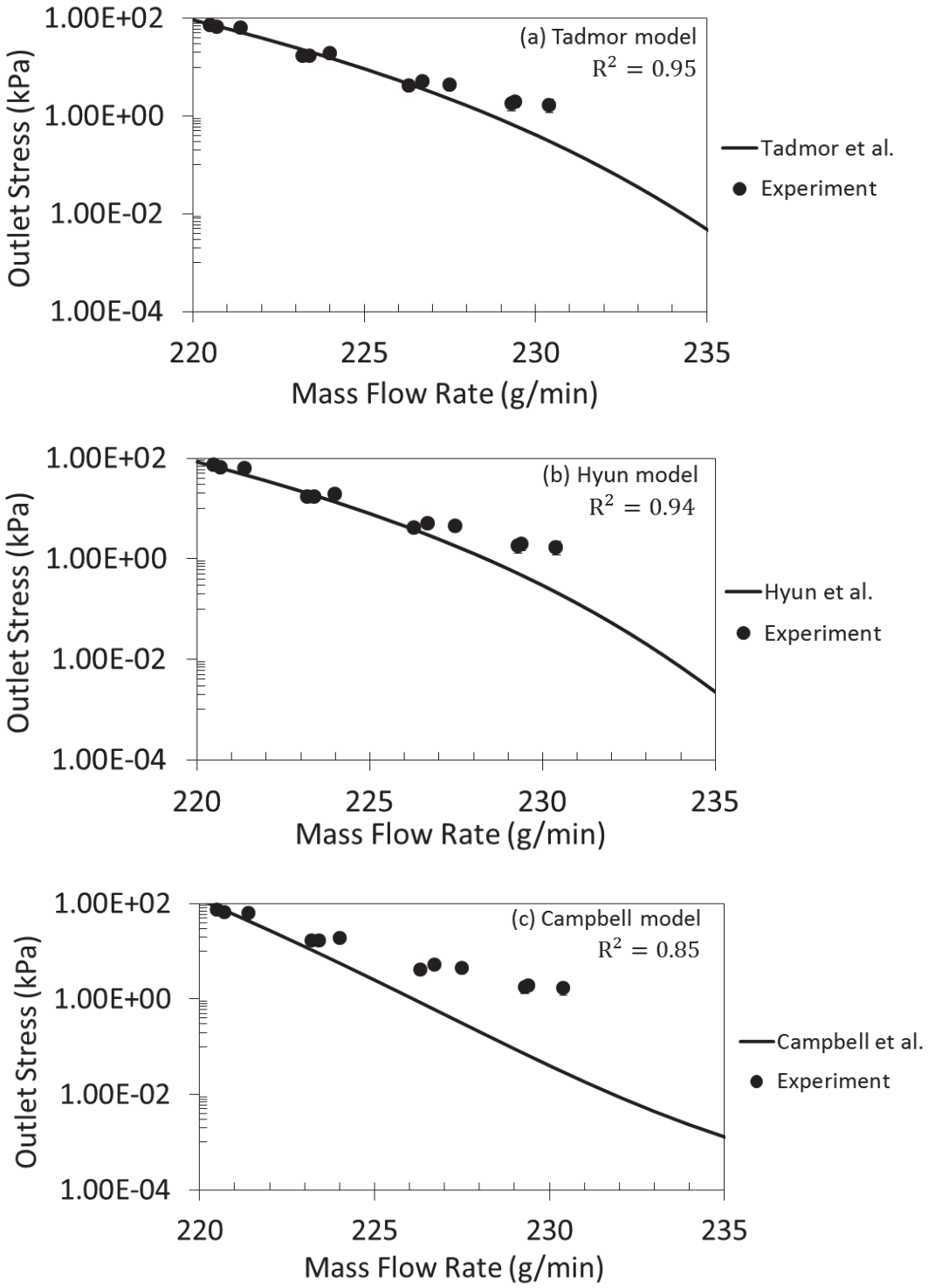

Figure 10.1. The Solid Plug models fitted to the experimental results using the friction coefficients as fitting parameters. The applied friction coefficients are listed in Table 10.1 while all other parameters are given in Table 5.1.

Table 10.1. Feed screw and barrel friction coefficient values applied to fit the Solid Plug models to the experimental results.

Solid Plug Model	Friction Coefficient	Fitted Friction Coefficient Value	Difference between the Fitted and Experimental Friction Coefficients
Tadmor et al.	μ_b	0.34	20.0%
	μ_s	0.08	46.7%
Hyun et al.	μ_b	0.35	24.0%
	μ_s	0.11	25.0%
Campbell et al.	μ_b	0.36	28.6%
	μ_s	0.06	57.7%

10.2 Fitting the Solid Plug Models to Experimental Results using the Stress Ratios

In this section the stress ratios applied at the screw flights (k_t) and at the barrel and screw core surfaces (k_r) are used as fitting parameters while all other input parameters remain unchanged from those given in Table 5.1. The results of fitting the Solid Plug models to the experimental results using the stress ratios are shown in Figure 10.2 and the applied stress ratios are listed in Table 10.2.

Although the stress ratios are used as fitting parameters, they are bounded from zero to one. The upper bound was set to one because the assumption that the down-channel stress is a major principal stress implies that the stress ratios will be less than one. The upper bound on the stress ratio was reached by the stress ratio applied at the screw core and barrel surfaces ($k_r = 1$) for each of the Solid Plug models (Table 10.2). Since the stress ratio applied at the screw core and barrel surfaces was set by the upper bound, essentially only the stress ratio applied at the screw flights was used as a fitting parameter.

Bounding the stress ratio applied at the screw core and barrel surfaces affects the slopes of the feeder outlet stress prediction curves (Chapter 8).

With only varying the stress ratio at the screw flights, the Solid Plug model developed by Campbell et al. (1995) was unable to fit the experimental results (Figure 10.2). The best fit the Campbell model could give ($R^2 = 0.03$) resulted when the stress ratio at the screw flights equaled zero ($k_t = 0$). Similarly, in order to fit the experimental results, the stress ratio applied at the screw flights in the Tadmor model approached zero ($k_t = 0.03$). As was shown when applying the friction coefficients as fitting parameters, both the Campbell and Tadmor models require unreasonable input parameters in order to fit the experimental results.

The model developed by Hyun et al. (1997a) once again is the only model which is able to predict the experimental results given reasonable input parameters. The stress ratio applied at the screw flights in order to fit the Hyun model to the experimental results was $k_t = 0.39$. This applied stress ratio falls between the stress ratio predicted by the kinetic theory of granular material (Lun, 1991) and the experimentally measured static stress ratio (k = 0.22). It is also worth noting that the stress ratio measured at the trailing screw flight in the DEM simulations of Moysey et al. (2004) was 0.36; however, the stress ratio measured at the leading screw flight was one. The assumptions made in this work that the material is a continuum and that the stresses at the leading and trailing screw flights both act perpendicular to the down channel stress, which is the major principal stress, forces the stresses at the screw flights to be equivalent.

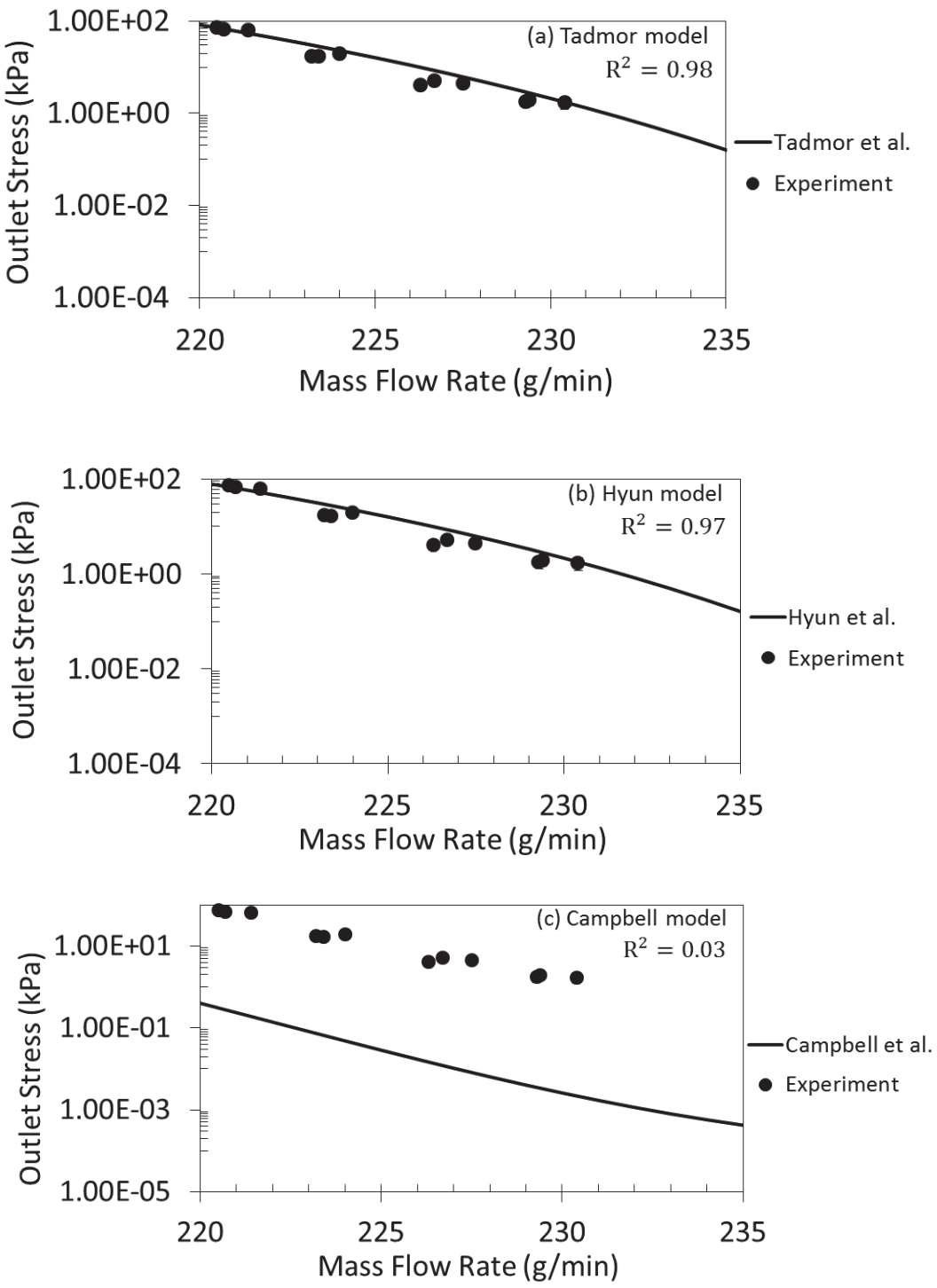

Figure 10.2. The Solid Plug models fitted to the experimental results using the stress ratios as fitting parameters. The applied stress ratios are listed in Table 10.2, while all other input parameters are given in Table 5.1.

Table 10.2. Stress ratio values applied to fit the Solid Plug models to the experimental results.

Solid Plug Model	Stress Ratio	Fitted Stress Ratio	Difference between the Fitted Stress Ratio and the Applied Stress Ratio (k = 1)
Hyun et al.	k_r	1.0	0%
	k_t	0.39	61%
Tadmor et al.	k_r	1.0	0%
	k_t	0.03	97%
Campbell et al.	k_r	1.0	0%
	k_t	0	100%

Lastly, shown in Figure 10.3 is the predicted material density at the feeder outlet for the Solid Plug model developed by Hyun et al. (1997a) fitted to the experimental results. The material density is shown to increase from the poured bulk density (0.32 g/cm^3) to almost the tapped bulk density of the material (0.42 g/cm^3). This shows that the combination of adjusting the material input parameters (friction coefficients or stress ratios) such that they cause the Solid Plug models to predict an increase in stress from the feeder inlet to the feeder outlet and the increase in the density given by the stress-density relationship both play a role in fitting the Solid Plug models to the experimental results. The increase in the material density at the feeder outlet was shown in Chapter 9 to increase the feeder outlet stress predictions and sensitivity of the Solid Plug models to the mass flow rate.

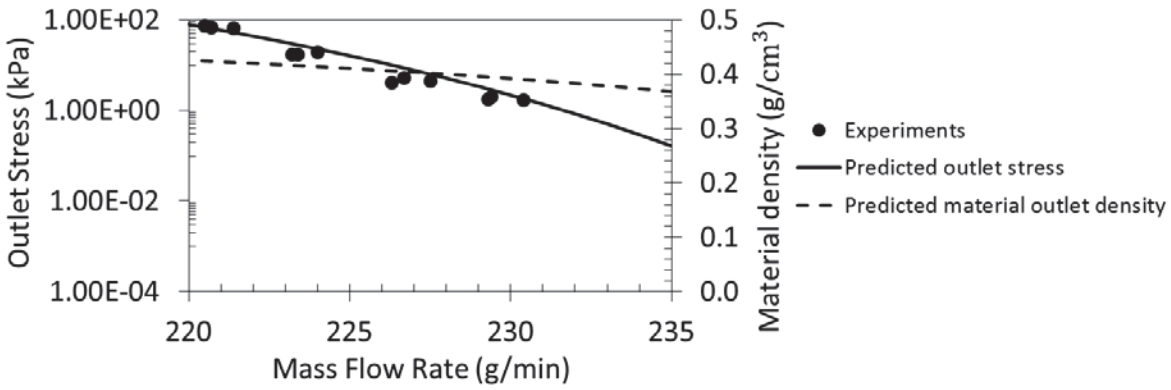

Figure 10.3. The Solid Plug model developed by Hyun et al. (1997a) fitted to the experimental results given the stress ratios in Table 10.2 and the parameters in Table 5.1. The plot also shows the predicted material density at the feeder outlet.

10.3 Conclusion

In this chapter the Solid Plug model developed by Hyun et al. (1997a) showed the best ability to fit the experimental results given reasonable friction coefficients and stress ratios. The fitted barrel and screw friction coefficient values varied from the initial input friction coefficients (Table 5.1) by 25% and -24%, respectively. When using the stress ratios as fitting parameters, the stress ratio applied at the barrel and screw core did not change from the initially assumed stress ratio of one, while the stress ratio applied at the screw flights decreased by 61%. These variations from the initial input parameters (Table 5.1) represent the best case scenarios.

The Solid Plug models in this chapter all applied stress ratios where either $k_r = k_t = 1$, when applying the friction coefficients as fitting parameters, or both k_r and k_t were applied as fitting parameters. The only difference in the models then was the assumptions of the force at the leading screw flight (dF^*) (Chapter 4). The differences in the applied force at the leading screw flight resulted in significant differences in the

models' predictions and behaviors, which showed that the Solid Plug model developed by Hyun et al. (1997a) best models the feed screw. Overall, since the friction coefficients could not be directly measured, due to the unknown surface finish of the materials, and the stress ratios are not well known (likely being between a value of one, predicted by the kinetic theory of granular material, and 0.22, the experimentally measured static stress ratio) it is possible that the Solid Plug models are capable of predicting the feeder outlet stress. The need for better defining these material parameters is highlighted in Chapter 12.

CHAPTER 11. SUMMARY AND CONCLUSIONS

The objective of this thesis was to predict the stress at the inlet of the nip region in a roll compactor. The roll inlet stress is a necessary input parameter for existing powder roll compaction models (Johanson, 1965; Katashinskii, 1986; Dec et al., 2003; Zavaliangos et al., 2003; Michrafy et al., 2011; Muliadi et al., 2012), and is difficult to directly measure on a roll compactor. Therefore, typically the roll inlet stress is applied as a fitting parameter to the powder roll compaction models. Additionally, most of parameters predicted by the powder roll compaction models have been shown to depend on the roll inlet stress. For these reasons it is desired to have a model which predicts the roll inlet stress. The ability to predict the roll inlet stress will allow for direct comparison between the powder roll compaction models and experimental results.

In order to predict the nip region inlet stress in a roll compactor, the Solid Plug model (Darnell et al., 1956; Tadmor et al., 1972; Campbell et al., 1995; Hyun et al., 1997a) was applied to a powder feed screw of a roll compactor. The Solid Plug model has been applied in the literature to feed screws in plastic screw extrusion processes. Additionally, the Solid Plug model derivation was extended to relate the feeder outlet stress to the feeder torque. The feeder torque is an output given by certain roll compactors and more easily measured than the roll inlet stress. With a feeder torque-outlet stress relationship, measuring the torque allows for the feeder outlet stress to be

predicted. The Solid Plug model was applied to a powder feed screw of a roll compactor for the following reasons:

1. The Solid Plug model predicts feeder outlet stress (roll inlet stress).
2. Fundamental in the Solid Plug model is a torque balance, which made it easy to relate the feeder outlet stress and the feeder torque.
3. The Solid Plug model is a simplistic 1-D model which would allow for real time process control when evaluated along with the 1-D Johanson model.

When the Solid Plug model was applied, using experimentally measured input parameters, to a powder feed screw of a roll compactor, the current work showed that:

1. The Solid Plug models of Tadmor et al. (1972), Campbell et al. (1995), and Hyun et al. (1997a) under-predicted the experimentally measured feeder outlet stress by several orders of magnitude.
2. The Solid Plug models were able to predict the exponential relationship between the mass flow rate and feeder outlet stress, and capture the sensitivity of the feeder outlet stress to the mass flow rate.
3. The Solid Plug models were able to fit the experimental results using the friction coefficients and stress ratios as fitting parameters. For the best case scenario, fitting the Solid Plug model developed by Hyun et al. (1997a) to the experimental results, the differences between the fitted parameters and the initial input parameters (Table 5.1) are given in Table 11.1.

Table 11.1. The percent differences between the initial input parameters (Table 5.1) and the fitted parameter values given by the Hyun et al. model (1997a) (Table 10.1 and 10.2).

Fitting the Experimental Results Using the Friction Coefficients	Percent Variation from the Initial Input Parameters
μ_b	25%
μ_b	-24%
Fitting the Experimental Results Using the Friction Coefficients	**Percent Variation from the Initial Input Parameters**
μ_b	0%
μ_b	61

4. The Solid Plug models were sensitive to the material friction coefficients and stress ratios. Specifically, the assumption of constant stress ratios at the barrel, screw core, and screw flights can greatly affect the Solid Plug models' predictions.
5. The Solid Plug models were dependent on the stress-density relationship applied to the Solid Plug models. If the Solid Plug models predicted an increase in the stress from the feeder inlet to the feeder outlet, then the increase in material density, which went along with the increase in stress, caused a rapid increase in the feeder outlet stress due to the iterative nature in which the Solid Plug model was solved.
6. The derivation of the feeder torque-outlet stress relationship was able to predict the linear relationship between the feeder torque and feeder outlet stress observed by the experimental measurements.
7. The mass flow rate-conveying angle relationship applied within the Solid Plug models was able to predict the mass flow rate of a feed screw for an open outlet condition (i.e., no applied outlet stress).

Although the Solid Plug models' feeder outlet stress predictions, given the input parameters in Table 5.1, were orders of magnitude below the experimental measurements (Chapter 7), the Solid Plug models were able to be fitted to the experimental results using either the stress ratios or friction coefficients as fitting parameters. Better measurements and stress dependent friction coefficients and stress ratios are expected to get the predicted feeder outlet stresses closer to the experimental results. Again, the stress ratio was assumed equal to one, based on the kinetic theory of granular materials, and the friction coefficient values were interpolated (Figure 5.13) because the surface finish of the feed screw and barrel were unknown.

In addition to the friction coefficient applied at the barrel (μ_b) being affected by the unknown surface finish of the barrel, the friction coefficient applied at the barrel would also be affected by the layer of material which formed along the bottom of the barrel during experiments (Chapter 7). With the bottom of the barrel being covered by a layer of material, the affective barrel friction coefficient on the bottom half of the barrel would be equal to the internal friction coefficient of the material, $\mu_b = \mu_{material}$. The friction coefficients applied at the top and bottom halves of the barrel would be different because the material being conveyed is sheared along the layer of material at the bottom half and the barrel surface at the top half. The internal friction coefficient of Avicel PH 102 is 0.94, whereas the applied barrel friction coefficient was 0.28 (Table 5.1). Based on the sensitivity of the Solid Plug models to the barrel friction coefficient (Chapter 8) and the fitted barrel friction coefficient values (Chapter 10), setting the affective barrel friction coefficient on the lower half of the barrel equal to the internal friction coefficient of the material is expected to greatly increase the feeder outlet stress predictions.

Accounting for the layer of material which formed along the bottom of the barrel would also reduce the affective barrel diameter. Decreasing the barrel diameter would decrease the feeder outlet stress predictions, however altering the applied friction coefficient on the bottom half of the barrel is expected to have a greater effect on the feeder outlet stress predictions. Therefore, overall the feeder outlet stress predictions would be expected to increase.

The Solid Plug models were also shown to be highly sensitive to the material input parameters and mass flow rate. Small variations in the material parameters or mass flow rate vary the feeder outlet stress significantly due to the exponential trend of the Solid Plug model and the iterative method in which the Solid Plug model was calculated. The sensitivity of the Solid Plug models is important if it is to be applied to the powder roll compaction models because the powder roll compaction models are sensitive to the roll inlet stress. Most of the roll compactor parameters predicted by the 1-D Johanson model have been shown to be proportional to the roll inlet stress. While further investigation of the material input parameters is necessary to validate the Solid Plug model, this thesis proposes, as an alternative to applying the Solid Plug model, applying the feeder torque-outlet stress relationship measured in the current work to predict the roll inlet stress.

The current thesis also contributes:

1. The extension of the Solid Plug model to relate the feeder outlet stress to the feeder torque resulting in a linear relationship between the feeder outlet stress and feeder torque.

2. The application of the Solid Plug model to a powder feed screw of a roll compactor.
3. Comparisons between the Solid Plug model predictions and experimental results, which is limited in the literature to the work of Hyun et al. (1997), Lovegrove et al. (1974), and Fang et al. (1991) due to the difficulty in measuring the feeder outlet stress.
4. The sensitivity analysis of the stress ratios at each feeder boundary (barrel, screw core, and screw flights) and relaxing the assumption of a uniform stress ratio. Demonstrating that the stress ratios need to be uniquely determined.
5. The experimentally measured stress ratio of microcrystalline cellulose (Avicel PH 102), $k = 0.22$ which was validated by the Mohr's circle analysis equation provided by Yu et al. (1997) and differs from the stress ratio applied in literature of $k = 0.4$ (Michrafy et al., 2004).

CHAPTER 12. FUTURE WORK

Once again, the objective of this thesis was to predict the feeder outlet stress. In the current work, when the stress ratios or friction coefficients were applied as fitting parameters, the Solid Plug models developed by Tadmor et al. (1972) and Hyun et al. (1997a) were shown to be able to fit the experimental feeder outlet stress measurements well (Chapter 10). Again, the stress ratios and friction coefficients were used as fitting parameters because the stress ratios were assumed to equal one, based on the kinetic theory of granular materials, and the friction coefficient values were interpolated (Figure 5.13), due to the surface finish of the feed screw and barrel being unknown.

For future work the Solid Plug models should be fitted to the experimental results using the stress ratios and friction coefficients, simultaneously, as fitting parameters. Based on the discussion of the Solid Plug models' sensitivity to the stress ratios and friction coefficients (Chapter 8), applying all four parameters ($k_t, k_r, \mu_b,$ and μ_s) as fitting parameters should decrease the difference between the fitted parameters and applied parameters given when the stress ratios or friction coefficients were applied as fitting parameters (Chapter 10). Again, it was shown in Chapter 8 that varying either the stress ratio applied at the barrel and screw core or the barrel friction coefficient changed the slope of the Solid Plug models' feeder outlet stress prediction curve, while varying either

the stress ratio applied at the screw flights or the screw friction coefficient was shown to shift the feeder outlet stress prediction curve up or down.

In addition to applying the stress ratios and friction coefficients as fitting parameters, the future work should focus on adding material property models to the Solid Plug model. The sensitivity of the Solid Plug model to material input parameters has shown that assuming constant material property values can greatly affect the Solid Plug model's predictions. One such assumption made in the current work that should be replaced by a stress dependent property in future work was the stress ratio. While the stress ratio is assumed constant in the Solid Plug model literature (Tadmor et al., 1972; Lovegrove et al., 1974; Campbell et al., 1995; Hyun et al., 1997a), the kinetic theory of granular material has shown the stress ratio to depend on the material solid fraction (Walton et al., 1986). It is more likely that the stress ratio varies along the length of the feed screw as the stress, and consequently solid fraction, increases toward the feeder outlet. In the current work the stress ratio is thought to change in the last few screw flights due to the degree of material compaction observed (Figure 7.1). The stress ratio at the feeder outlet may more closely resemble the stress ratio measured experimentally in a quasi-static regime ($k = 0.22$) (punch and die), as opposed to the stress ratio predicted by the kinetic theory for granular material ($k = 1$) (Lun, 1991).

Another material parameter that was assumed constant in the current work and should be made stress dependent in future work was the friction coefficient. Although the friction coefficients measured were shown to be relatively constant over an applied stress range of 5-20 kPa (Figure 5.12), the sensitivity of the Solid Plug models to the

material parameters necessitates stress dependent parameters. Implementation of more material parameter models, such as the friction coefficient and stress ratio, into the Solid Plug model allow for the most ideal comparison between the Solid Plug model and experimental results. Consequently, future work requires further investigation into the applied stress ratios and friction coefficients before linking the Solid Plug model with the powder roll compaction models, in order to predict roll compactor properties (roll force, roll torque and ribbon density).

While further validation of the Solid Plug model is necessary before linking it with the powder roll compaction models to predict the roll compactor parameters, the experimental results demonstrated a linear relationship between the feeder torque and feeder outlet stress which can be applied to predict the feeder outlet stress. The feeder torque-outlet stress relationship, along with the powder roll compaction models, can then be applied in future work for process control feedback.

For future work then, the feeder torque-outlet stress relationship should be experimentally determined by directly measuring the feeder torque on a roll compactor and using the 1-D Johanson model to back-calculate the feeder outlet stress. The feeder torque can be measured on a roll compactor by either implementing a torque sensor on the roll compactor, using a dynamometer to calibrate the torque of the roll compactor motor with the current output load, or certain roll compactors give as an output the feeder torque. In order to back calculate the feeder outlet stress, the roll force predicted by the 1-D Johanson model should be fitted to the experimentally measured roll force using the feeder outlet stress. Then to measure several points of the feeder torque-outlet stress relationship, the roll compactor parameters (screw speed, roll speed, or roll gap) can be

varied. Once the feeder torque-outlet stress relationship has been fully developed, this relationship, along with the 1-D Johanson model, can be used for real time process control. The real time process control will measure the feeder torque and then apply the torque-outlet stress relationship to determine the feeder outlet stress. The 1-D Johanson model can then be applied, using the determined feeder outlet stress as an input, to give real time feedback of the roll compactor properties (roll force, roll torque and ribbon density). The real time process control is useful for controlling ribbon properties which affect granule size, and consequently compaction properties. Real time feedback is useful in determining how fluctuations in the roll compactor parameters affect the ribbon properties, and for determining which roll compactor parameters have the greatest effect on the ribbon properties.

The future work aims to improve the stress dependent material property relationships of the Solid Plug model. Adding more stress dependent material property relationships to the Solid Plug model should allow for the Solid Plug model to better predict experimental results. The future work also includes real time process control of roll compactor output properties, by applying the feeder torque-outlet stress relationship to the 1-D Johanson model.

LIST OF REFERENCES

LIST OF REFERENCES

G. Bindhumadhavan, J.P.K Seville, M.J. Adams, R.W. Greenwood, and S. Fitzpatrick, Roll compaction of a pharmaceutical excipient: experimental validation of rolling theory for granular solids, Chemical Engineering Science, 60 (2005) 3891-3897.

B.J. Briscoe, and S.L. Rough, The effects of wall friction in powder compaction, Physicochemical and Engineering Aspects, 137 (1998) 103-116.

E. Broyer, and Z. Tadmor, Solids conveying in screw extruders part I: a modified isothermal model, Polymer Engineering and Science, 12 (1972) 12-24.

C.S. Campbell, The stress tensor for simple shear flows of a granular material, Journal of Fluid Mechanics, 203 (1989) 449-473.

G.A. Campbell, and N. Dontula, Solids transport in extruders, Intern. Polymer Processing, 10 (1995) 30-35.

F. da Cruz, S. Emam, M. Prochnow, J Roux, and F. Chevoir, Rheophysics of dense granular materials: Discrete simulation of plane shear flows, Physical Review, 72 (2005).

J.C. Cunningham, Experimental studies and modeling of the roller compaction of pharmaceutical powders, PhD Thesis, Drexel University, 2005.

J.C. Cunningham, D. Winstead, and A. Zavaliangos, Understanding variation in roller compaction through finite element-based process modeling, Computers and Chemical Engineering, 34 (2010) 1058-1071.

J. Dai, and J.R. Grace, A model for biomass screw feeding. Powder Technology, 186 (2008) 40-55.

J. Dai, and J.R. Grace, Biomass granular screw feeding: An experimental investigation. Biomass and Bioenergy, 35 (2011) 942-955.

W.H. Darnell, and E.A.J. Mol, Solids conveying in extruders, SPE Journal, 12 (1956) 20.

R.T. Dec, Study of compaction process in roll press, in: proceedings of the Institute for briquetting and agglomeration, 22, 1991, 207-218.

R.T. Dec, A. Zavaliangos, and J.C. Cunningham, Comparison of various modeling methods for analysis of powder compaction in roller press, Powder Technology, 130 (2003) 265-271.

H. Decker, Die Spritzmaschine (The Extruder), P. Troester, Hanover, Germany (1941).

M.H. Es-Saheb, Uniaxial strain rate effects in pharmaceutical powders during cold compaction, Journal of Materials Science, 27 (1992) 4151-4159.

S. Fang, L. Chen, and F. Zhu, Studies on the theory of single screw plasticating extrusion part II: non-plug flow solid conveying, Polymer Engineering and Science, 31 (1991) 1117-1122.

R.T. Fenner, Developments in the analysis of steady screw extrusion of polymers, Polymer, 18 (1977) 617-635.

C.G. Gogos, M. Esseghir, D.B. Todd, D.W. Yu, and J.E. Curry. SPE Antec Tech. Papers 40 (1994) 270.

P. Guigon, and O. Simon, Roll press design—influence of force feed systems on compaction, Powder Technology, 130 (2003) 41-48.

B.C. Hancock, J.T. Colvin, M.P. Mullarney, and A.V. Zinchuk, The relative density of pharmaceutical powders, blends, dry granulations and immediate release tablets, Pharmaceutical Technology, (2003) 64-80.

M.G. Herting, and P. Kleinebudde, Roll compaction/dry granulation: effect of raw material particle size on granule and tablet properties, International Journal of Pharmaceutics, 338 (2007) 110-118.

H. Hong, J.A Covas, and A. Gaspar-Cunha, The use of DEM to capture the dynamics of the flow of solid pellets in a single screw extruder, AIP Conference Proceedings, 908 (2007) 1537-1542.

K.S. Hyun, and M.A. Spalding, Bulk density of solid polymer resins as a function of temperature and pressure, Polymer Engineering and Science, 30 (1990) 571-576.

K.S. Hyun, and M.A. Spalding, A new model for solids conveying in single screw plasticating extruders, SPE ANTEC Tech. Papers, 1 (1997) 211-218.

K.S. Hyun, M.A. Spalding, and C.E Hinton, Theoretical and experimental analysis of solids conveying in single-screw extruders, Journal of Reinforced Plastics and Composites, 16 (1997) 1210-1219.

H.A. Janssen, Versuche uber Getreidedtruck in Silozellen, Zeitschr. d. Vereines deutscher Ingenieure, 39 (1895) 1045.

A.W. Jenike, and R.T. Shiel, On the plastic flow of Coulomb solids beyond original failure, ASME Journal of Applied Mechanics, E26 (81) (1959) 599-602.

J.R. Johanson, A rolling theory for granular solids, ASME Journal of Applied Mechanics, E32 (4) (1965) 842-848.

V.P. Katashinskii, Analytical determination of specific pressure during the rolling of metal powder, Powder Metallurgy and Metal Ceramics, 5 (1986) 765-772.

V.P. Katashinskii, and M.B. Shtern, Stress-strain state of powder being rolled in the densification zone-I. mathematical model of rolling in the densification zone, Powder Metallurgy and Metal Ceramics, 22 (1983a) 882-885.

V.P. Katashinskii, and M.B. Shtern, Stress-strain state of powder being rolled in the densification zone-II. distribution of density, longitudinal strain, and contact stress in the densification zone, Powder Metallurgy and Metal Ceramics, 22 (1983b) 972-976.

J.G.A Lovegrove, and J.G. Williams, Solids conveying in a single screw extruder; a comparison of theory and experiment, Journal Mechanical Engineering Science, 15 (1973a) 195-199.

J.G.A Lovegrove, and J.G. Williams, Solids conveying in a single screw extruder; the role of gravity forces, Journal Mechanical Engineering Science, 15 (1973b) 114-122.

J.G.A Lovegrove, and J.G. Williams, Pressure generation mechanisms in the feed section of screw extruders, Polymer Engineering and Science, 14 (1974) 589-594.

C.K.K. Lun, Kinetic theory for granular flow of dense, slightly inelastic, slightly rough spheres, Journal of Fluid Mechanics, 223 (1991) 539-559.

C.K.K. Lun, and S.B Savage, A simple kinetic theory for granular flow of rough, inelastic spherical particles, Journal of Applied Mechanics, 54 (1987) 47-53.

O.P. Michelangelli, M. Yamanoi, A. Gaspar-Cunha, and J.A. Covas, Modelling pellet flow in single extrusion with DEM, Journal of Process Mechanical Engineering, 225 (2011) 255-268.

A. Michrafy, H. Diarra, J.A. Dobbs, and M. Michrafy, Experimental and numerical analyses of homogeneity over strip width in roll compaction, Powder Technology, 206 (2011) 154-160.

A. Michrafy, J.A. Dodds, and M.S. Kadiri, Wall friction in the compaction of pharmaceutical powders: measurement and effect on density distribution, Powder Technology, 148 (2004) 53-55.

A.M. Miguelez-Moran, C.Y. Wu, H. Dong, and J.P.K. Seville, Characterisation of density distributions in roller-compacted ribbons using micro-indentation and X-ray micro-computed tomography, European Journal of Pharmaceutics and Biopharmaceutics, 72 (2009) 173-182.

P.A. Moysey, and M.R. Thompson, Investigation of solids transport in a single-screw extruder using a 3-D discrete particle simulation, Polymer Engineering and Science, 44 (2004) 2203-2215.

P.A. Moysey, and M.R. Thompson, Modelling the solids inflow and solids conveying of single-screw extruders using the discrete element method, Powder Technology, 153 (2005) 95-107.

P.A. Moysey, and M.R. Thompson, Discrete particle simulations of solids compaction and conveying in a single-screw extruder, Polymer Engineering and Science, (2008) 62-73.

A.R. Muliadi, J.D. Litster, and C.R. Wassgren, Modeling the powder roll compaction process: comparison of 2-D finite element method and the rolling theory for granular solids (Johanson's model), Powder Technology, 221 (2012) 90-100.

A.R. Muliadi, J.D. Litster, and C.R. Wassgren, Validation of 3-D finite element analysis for predicting the density distribution of roll compacted pharmaceutical powder, Powder Technology 237 (2013) 386-399.

V.V. Nesarikar, C. Patel, W. Early, N. Vatsaraj, O. Sprockel, and R. Jerzweski, Roller compaction process development and scale up using Johanson model calibrated with instrumented roll data, International Journal of Pharmaceutics, 436 (2012a) 486-507.

V.V. Nesarikar, N. Vatsaraj, C. Patel, W. Early, P. Pandey, O. Sprockel, Z. Gao, R. Jerzewski, R. Miller, and M. Levin, Instrumented roll technology for the design space development of roller compaction process, International Journal of Pharmaceutics, 426 (2012b) 116-131.

H. Pontente, and T.C Pohl, Polymer Pellet Flow out of the Hopper into the First Section of a Single Screw. International Polymer Processing, 7 (2002) 11-21.

G. Reynolds, R. Ingale, R. Roberts, S. Kothari, and B. Gururajan, Practical application of roller compaction process modeling, Computers and Chemical Engineering, 34 (2010) 1049-1057.

S.B.Savage, and D.J. Jeffrey, The stress tensor in a granular flow at high shear rates, Journal of Fluid Mechanics, 110 (1981) 255-272.

G.P.M. Schenkel, Effects of recent fundamental investigations on extruder design, International Plastic Engineering, 6 (1961) 315-323.

I.C. Sinka, J.C. Cunningham, and A. Zavaliangos, The effect of wall friction in the compaction of pharmaceutical tables with curved faces: a validation study of the Drucker-Prager Cap model, Powder Technology, 133 (2003) 33-43.

M.A. Spalding, K.S. Hyun, and K.R. Hughes, Stress distribution in solid polymer compacts, Journal of Reinforced Plastics and Composites, 16 (1997) 1231-1241.

M.A. Spalding, D.E. Kirkpatrick, and K.S. Hyun, Coefficients of dynamic friction for low density polyethylene, Polymer Engineering and Science, 33 (1993) 423-430.

Z. Tadmor, and E. Broyer, Solids conveying in screw extruders part II: non isothermal model, Polymer Engineering and Science, 12 (1972) 378-386.

Z. Tadmor, and I. Klein, “Engineering Principles of Plasticating Extrusion,” Van Nostrand Reinhold Co., New York, 1970.

D.M. Walker, An approximate theory for pressures and arching in hopper, Chemical Engineering Science, 21 (1966) 975-997.

O.R. Walton, and R.L. Braun, Stress calculations for assemblies of inelastic spheres in uniform shear, Acta Mechanica, 63 (1986) 73-86.

J.L White, and U. Berghaus, "Screw Extrusion," Hanser, Munich Germany, 2003.

Y. Yu, and P.C Arnold, Theoretical modeling of torque requirements for single screw feeders. Powder Technology, 93 (1997) 151-162.

Y.A. Yusof, A.C Smith, and B.J. Briscoe, Roll compaction of maize powder, Chemical Engineering Science, 60 (2005) 3919-3931.

A. Zavaliangos, R.T. Dec, and R.K. Komarek, Analyses of powder processing in the roller press using finite element modeling, in: XXII Internation Mineral Processing Congress, Cape Town, South Africa, 2003.

F. Zhu, and L. Chen, Studies on the theory of single screw plasticating extrusion part I: a new experimental method for extrusion, Polymer Engineering and Science, 31 (1991) 1113-1116.

A.V. Zinchuk, M.P. Mullarney, and B.C. Hancock, Simulation of roller compaction using a laboratory scale compaction simulator, International Journal of Pharmaceutics, 269 (2004) 403-415.

APPENDICES

Appendix A. Derivation of the Mass Flow Rate-Conveying Angle Relationship

In this appendix the mass flow rate-conveying angle relationship will be derived. The mass flow rate is given by,

$$\dot{M} = \rho V_a A, \tag{A.1}$$

where ρ is the material density, V_a is the axial velocity of the material, and A is the cross-sectional area of the screw channel. The cross-sectional area of the screw channel is given by,

$$A = \int_{R_{sc}}^{R_b} \left(2\pi r - \frac{pe}{\sin(\bar{\phi})} \right) dr, \tag{A.2}$$

where R_b is the barrel radius, R_{sc} is the screw core radius, p is the number of parallel screw flights, e is the screw flight thickness, and $\bar{\phi}$ is the average helical angle. The first term in Equation (A.2) gives the cross-sectional area of the annulus made up of the barrel and screw core (Figure A.1) while the second term subtracts the screw flight thickness (Figure A.2). The cross-sectional area calculated by Equation (A.2) is shown in Figure A.3.

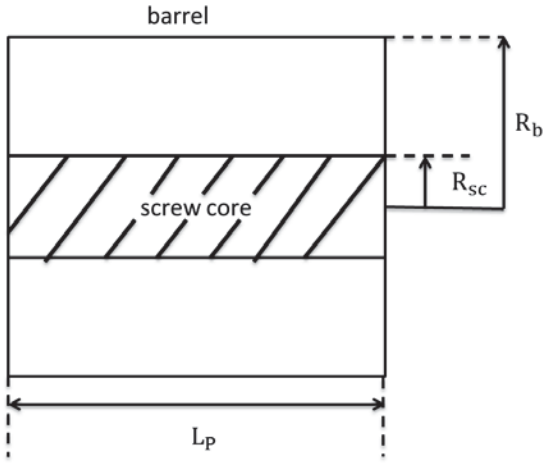

Figure A.1. Schematic showing the cross-sectional area of the annulus made up of the barrel and screw core.

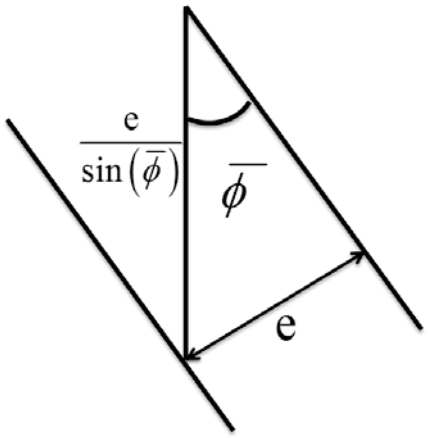

Figure A.2. Schematic showing the screw flight geometry.

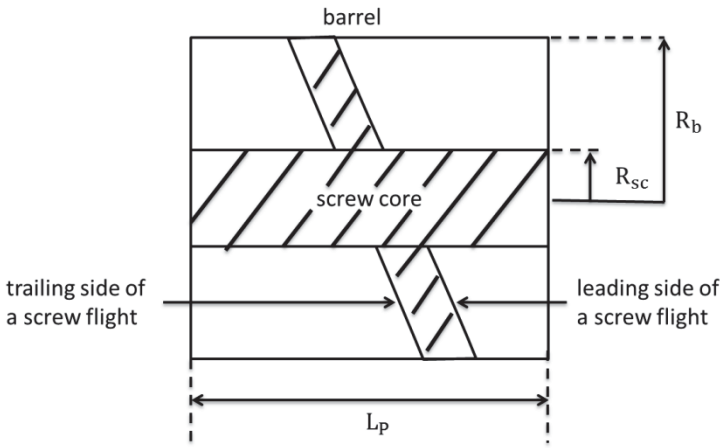

Figure A.3. Schematic showing the cross-sectional area of a screw channel given by Equation (A.2).

Integrating Equation (A.2) gives,

$$A = \pi(R^2_b - R^2_{sc}) - \frac{pe(R_b - R_{sc})}{\sin(\bar{\phi})} \tag{A.3}$$

To get the mass flow rate-conveying angle relationship derived by Tadmor et al. (1972), the barrel and screw core diameters are substituted in place of the barrel and screw core radii,

$$A = \frac{\pi}{4}(D^2_b - D^2_{sc}) - \frac{pe(D_b - D_{sc})}{2\sin(\bar{\phi})} \tag{A.4}$$

Assuming that the gap between the screw flights and barrel is negligible, the barrel diameter can be related to the screw core diameter and the height of the screw channel by,

$$D_b = D_{sc} + 2H\,, \tag{A.5}$$

where H is the screw channel height. Substituting Equation (A.5) into Equation (A.4) gives,

$$A = \pi H(H + D_{sc}) - \frac{peH}{\sin(\bar{\phi})} \tag{A.6}$$

Now that the cross-sectional area of the screw channel has been specified in terms of the feeder geometry, the axial velocity of the material will be determined in terms of the conveying angle, feeder geometry, and screw speed. Recall that in the Solid Plug model derivation the screw is held stationary and the barrel is rotated. Shown in Figure A.4 is the barrel velocity (V_b), barrel velocity relative to the material (V_{bm}), velocity of the material in the down channel direction (V_z), and velocity of the material in the axial direction (V_a).

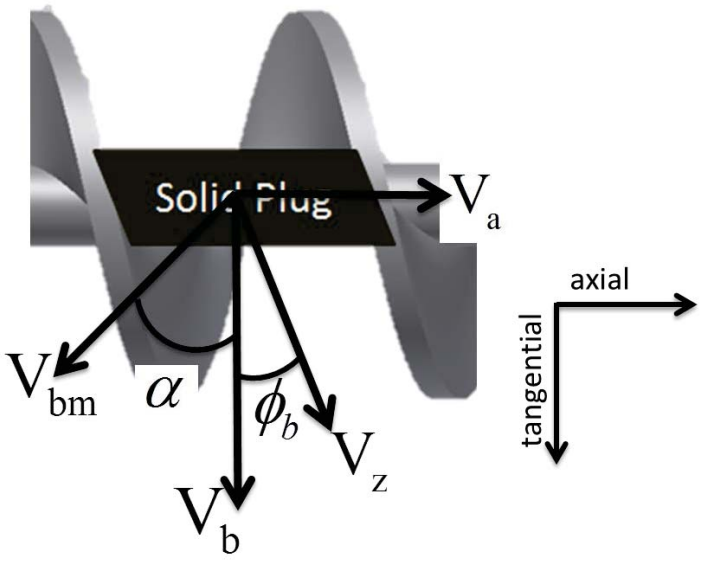

Figure A.4. Schematic showing the barrel velocity (V_b), barrel velocity relative to the material (V_{bm}), velocity of the material in the down channel direction (V_z), and velocity of the material in the axial direction (V_a).

The barrel velocity relative to the material and the velocity of the material in the down channel direction given in terms of the axial velocity of the material are,

$$V_{bm} = \frac{|V_a|}{\sin(\alpha)}, \tag{A.7}$$

and,

$$V_z = \frac{V_a}{\sin(\phi_b)}, \tag{A.8}$$

where α is the conveying angle and ϕ_b is the helical angle at the barrel surface (Figure A.5).

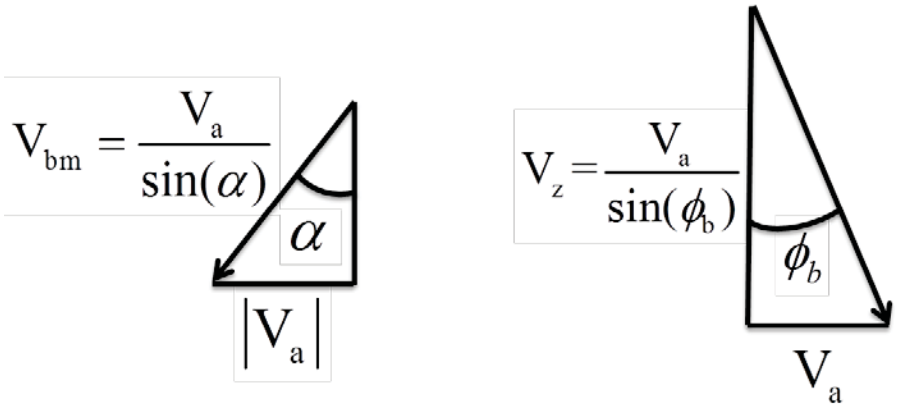

Figure A.5. Schematic showing the relationships of the barrel velocity relative to the material (V_{bm}) (left) and the velocity of the material in the down channel direction (V_z) (right) to the axial velocity of the material (V_a).

The barrel velocity given in terms of the velocity of the material in the down channel direction and the barrel velocity relative to the material is (Figure A.6),

$$V_b = V_{bm}\cos(\alpha) + V_z\cos(\phi_b) \tag{A.9}$$

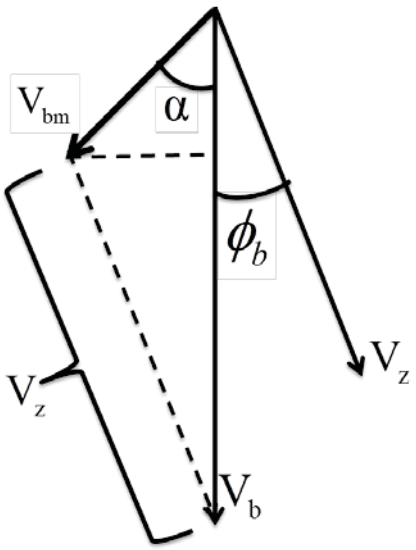

Figure A.6. Schematic showing the relationship of the barrel velocity (V_b) to the velocity of the material in the down channel direction (V_z) and the barrel velocity relative to the material (V_{bm}).

Substituting Equations (A.7) and (A.8) into Equation (A.9),

$$V_b = V_a\left(\frac{\cos(\alpha)}{\sin(\alpha)} + \frac{\cos(\phi_b)}{\sin(\phi_b)}\right), \tag{A.10}$$

then solving Equation (A.10) for the axial velocity of the material,

$$V_a = V_b\left(\frac{\tan(\alpha)\tan(\phi_b)}{\tan(\alpha)+\tan(\phi_b)}\right) \tag{A.11}$$

Lastly, the barrel velocity can be related to the screw velocity by,

$$V_b = \pi D_b V_s, \tag{A.12}$$

where V_s is the screw velocity. Substituting Equation (A.12) into (A.11) gives,

$$V_a = \pi D_b V_s\left(\frac{\tan(\alpha)\tan(\phi_b)}{\tan(\alpha)+\tan(\phi_b)}\right) \tag{A.13}$$

Finally substituting Equations (A.6) and (A.13) into Equation (A.1),

$$\dot{M} = \rho\pi D_b V_s \left(\frac{\tan(\alpha)\tan(\phi_b)}{\tan(\alpha)+\tan(\phi_b)} \right) \left(\pi H(H + D_{sc}) - \frac{peH}{\sin(\bar{\phi})} \right), \tag{A.14}$$

and solving for the conveying angle gives,

$$\alpha = \arctan\left(\frac{\dot{M}\tan(\phi_b)}{\rho\pi V_s D_b \tan(\phi_b)\left(\pi H(D_s + H) - \frac{peH}{\sin(\bar{\phi})} \right) - \dot{M}} \right) \tag{A.15}$$

Appendix B. Uncertainty Calculations

In this appendix the uncertainty of the experimental measurements, material property measurements, as well as the derived uncertainty of the Solid Plug models are calculated. First, how the uncertainty is calculated will be outlined and then the uncertainty of each parameter will be discussed.

Let Y be a result that depends on several parameters, $x_1, x_2, \ldots, x_n$. The variation in Y due to the i^{th} parameter (δY_{x_i}) is given by,

$$\delta Y_{x_i} = \frac{\partial Y}{\partial x_i}\delta x_i, \tag{B.1}$$

where δx_i is the uncertainty in the parameter x_i. The total uncertainty of Y, δ_Y, is given by,

$$\delta Y = \sqrt{\sum_{i=1}^{n}\left(\frac{\partial Y}{\partial x_i}\delta x_i\right)^2}, \tag{B.2}$$

and the relative uncertainty, u_Y, is,

$$u_Y = \frac{\delta Y}{Y} \tag{B.3}$$

Equations (B.1-B.3) will be used in the following sections to calculate the uncertainty of various parameters.

Mass Flow Rate Uncertainty

The uncertainty of the mass flow rate measurements depends on the uncertainty of the mass measured by the balance and the uncertainty of the time measured by the CPU. The relative uncertainty of the mass flow rate is given by,

$$u_{\dot{M}} = \frac{\delta \dot{M}}{\dot{M}} = \frac{1}{\dot{M}} \sqrt{\left(\frac{\partial \dot{M}}{\partial m} \delta m \right)^2 + \left(\frac{\partial \dot{M}}{\partial t} \delta t \right)^2}, \tag{B.4}$$

where the uncertainty of the mass measured by the balance (δm) is +/- 0.1 g and the uncertainty of the time measured by the CPU (δt) is +/- 0.001 sec. The relative uncertainty and the total uncertainty remained relatively constant over the experimentally measured mass flow rate range (220-245 g/min). The relative uncertainty ($u_{\dot{M}}$) was 0.04% and the total uncertainty ($\delta \dot{M}$) was +/- 0.1 g/min. The relative uncertainties in the mass and time were,

$$u_m = \frac{\delta m}{m} = \frac{0.1}{220} = 0.04\%, \tag{B.5}$$

and,

$$u_t = \frac{\delta t}{t} = \frac{0.001}{60} = 0.001\% \tag{B.6}$$

Feeder Outlet Stress Uncertainty

The relative uncertainty of the feeder outlet stress measurements (u_σ),

$$u_\sigma = \frac{\delta \sigma}{\sigma} = \frac{1}{\sigma} \sqrt{\left(\frac{\partial \sigma}{\partial f} \delta f \right)^2 + \left(\frac{\partial \sigma}{\partial A} \delta A \right)^2}, \tag{B.7}$$

depends on the relative uncertainty of the force measured by the load cell (f) at the outlet of the feeder and the relative uncertainty of the plug area (A). Again, the feeder outlet stress was calculated as the force applied to the load cell at the base of the plug divided by the cross-sectional area of the plug (Figure 6.2). The uncertainty of the force (δ_f) measured by the load cell, or the least count of the load cell, was +/- 0.004 N. The relative uncertainty of the plug area,

$$u_A = \frac{\delta A}{A} = \frac{1}{A}\left(\frac{\partial A}{\partial D}\delta D\right), \tag{B.8}$$

was due to the uncertainty of the plug diameter (δ_d), which was +/- 0.01 cm. Substituting Equation (B.8) into Equation (B.7) gives,

$$u_\sigma = \frac{\delta\sigma}{\sigma} = \frac{1}{\sigma}\sqrt{\left(\frac{\partial\sigma}{\partial f}\delta f\right)^2 + \left(\frac{\partial\sigma}{\partial D}\delta D\right)^2} \tag{B.9}$$

For the range of plug diameters applied in the experimental measurements (Table 6.1) and the forces measured for each applied plug diameter, the relative uncertainty of the feeder outlet stress measurements ranged from 0.7% - 1.3%, where the relative uncertainty decreased as the plug diameter increased. The total uncertainty of the feeder outlet stress measurements ($\delta\sigma$) ranged from 0.02 kPa - 0.5 kPa, where the greater uncertainty corresponds to the larger plug diameter. The relative uncertainties in the force and area measurements for the smallest plug size were,

$$u_f = \frac{\delta f}{f} = \frac{0.004}{0.4513} = 0.88\%, \tag{B.10}$$

and,

$$u_A = \frac{\delta A}{A} = \frac{1}{A}\left(\frac{\partial A}{\partial D}\delta D\right) = \frac{1}{A}\left(\frac{\pi D}{2}\delta D\right) = \frac{1}{A}\left(\frac{\pi * 2.09}{2} * 0.01\right) = 0.95\%, \tag{B.11}$$

whereas the relative uncertainties for the largest plug size were,

$$u_f = \frac{0.004}{47.25} = 8.47 * 10^{-3}\%, \tag{B.12}$$

and,

$$u_A = \frac{1}{A}\left(\frac{\pi * 2.85}{2} * 0.01\right) = 0.7\% \tag{B.13}$$

Feeder Torque Uncertainty

Since the only calculation necessary to determine the feeder torque was multiplying the torque sensor output by the ratio of the gear box (10:1), the uncertainty of the feeder torque measurements equals +/- 0.001 N.m. Again, the uncertainty of the torque sensor, or the least count, is +/- 0.0001 N.m.

Derived Uncertainty

Finally, this section calculates the derived uncertainty of the parameters input into the Solid Plug model. The derived uncertainties calculated below are for the parameters which were not directly measured but instead, were calculated. These parameters consist of the helical angles (Equation (5.3)), channel width at the screw core (Equation (5.2)), average channel width (Equation (5.1)), and conveying angle (Equation (A.15)).

The relative uncertainty of the average helical angel ($\overline{\emptyset}$) and the helical angles at the screw core ($\emptyset_{sc}$), and barrel ($\emptyset_b$), $u_\emptyset$,

$$u_\phi = \frac{\delta \phi}{\phi} = \frac{1}{\phi}\sqrt{\left(\frac{\partial \phi}{\partial L_P}\delta L_P\right)^2 + \left(\frac{\partial \phi}{\partial D}\delta D\right)^2}, \tag{B.14}$$

is due to the uncertainty in the pitch length (L_P), and corresponding diameter (D) (Chapter 5). The measurements and uncertainties of the pitch length and diameters are given in Table 5.1. The partial derivatives of the helical angle with respect to the pitch length and diameter are given by,

$$\frac{\partial \phi}{\partial Lp} = \frac{p}{D\left(1+\frac{L_P{}^2 p^2}{D^2\pi^2}\right)\pi}, \tag{B.15}$$

and,

$$\frac{\partial \phi}{\partial D} = -\frac{L_p p}{D\left(1+\frac{L_p{}^2 p^2}{D^2\pi^2}\right)\pi}, \tag{B.16}$$

respectively. The relative and total uncertainties of the helical angles as well as the relative uncertainties of the pitch length and diameters are given in Table B.1.

Table B.1. The relative and total uncertainty of the conveying angles as well as the relative uncertainty of each parameter that the conveying angle depends on.

Parameters	Calculated Uncertainty
$\delta\emptyset_{sc}$	0.25 deg
$u_{\emptyset_{sc}}$	0.56%
$\delta\emptyset_b$	0.10 deg
$u_{\emptyset_b}$	0.51%
$\delta\overline{\emptyset}$	0.21 deg
$u_{\overline{\emptyset}}$	0.77%
u_{L_p}	0.48%
u_{D_b}	0.26%
$u_{D_{sc}}$	0.71%
$u_{\overline{D}}$	0.77%

The uncertainty of the average screw channel width ($\overline{W}$), and the screw channel width at the screw core (W_{sc}) are given by,

$$u_w = \frac{\delta W}{W} = \frac{1}{W}\left[\sqrt{\left(\frac{\partial W}{\partial L_p}\delta L_p\right)^2 + \left(\frac{\partial W}{\partial \phi}\delta\phi\right)^2 + \left(\frac{\partial W}{\partial e}\delta e\right)^2}\right], \tag{B.17}$$

where to determine the uncertainty of the average screw channel width or the screw channel width at the screw core, the appropriate helical angle is applied to Equation (B.17) (Chapter 5). The uncertainty of the channel width depends on the uncertainty of the pitch length, helical angle, and screw flight thickness (δe). The partial derivatives of the screw

channel width with respect to the pitch length, helical angle, and screw flight thickness are given by,

$$\frac{\partial W}{\partial Lp} = \cos(\phi), \tag{B.18}$$

$$\frac{\partial W}{\partial \phi} = -Lp\sin(\phi), \tag{B.19}$$

and,

$$\frac{\partial W}{\partial e} = -1, \tag{B.20}$$

respectively. The calculated relative and total uncertainties are given in Table B.2.

Table B.2. The relative and total uncertainty of the average channel width and channel width at the screw core as well as the relative uncertainty of each parameter that the channel widths depend on.

Parameters	Calculated Uncertainty
δW_{sc}	0.014 cm
$u_{W_{sc}}$	1.16%
$\delta \bar{\bar{W}}$	0.014 cm
$u_{\bar{W}}$	0.9%
u_{L_p}	0.48%
$u_{\bar{\phi}}$	0.77%
$u_{\phi_{sc}}$	0.56%
u_e	3.13%

Lastly, the relative uncertainty of the conveying angle,

$$u_\alpha = \frac{\delta\alpha}{\alpha} = \frac{1}{\alpha}\left[\sqrt{\left(\frac{\partial\alpha}{\partial\dot{M}}\delta\dot{M}\right)^2 + \left(\frac{\partial\alpha}{\partial\phi_b}\delta\phi_b\right)^2 + \left(\frac{\partial\alpha}{\partial V_s}\delta V_s\right)^2 + \left(\frac{\partial\alpha}{\partial D_b}\delta D_b\right)^2 + \left(\frac{\partial\alpha}{\partial H}\delta H\right)^2 + \left(\frac{\partial\alpha}{\partial D_{sc}}\delta D_{sc}\right)^2 + \left(\frac{\partial\alpha}{\partial e}\delta e\right)^2 + \left(\frac{\partial\alpha}{\partial\bar{\phi}}\delta\bar{\phi}\right)^2}\right], \tag{B.21}$$

depends on the mass flow rate ($\dot{M}$), helical angle at the barrel ($\emptyset_b$), screw speed (V_s), barrel diameter (D_b), channel height (H), screw core diameter (D_{sc}), screw flight thickness (e), and average helical angle ($\bar{\emptyset}$) uncertainties. The uncertainties and measurements of the various parameters which the conveying angle depends on are given in Table 5.1. The relative uncertainties and total uncertainty of the helical angle are given in Table B.3.

Table B.3. The relative and total uncertainty of the conveying angle as well as the relative uncertainty of each parameter that the conveying angle depends on.

Parameters	Calculated Uncertainty
$\Delta\alpha$	0.06 deg
u_α	0.10 %
$u_{\dot{M}}$	0.04%
$u_{\emptyset_b}$	0.51%
$u_{\bar{\emptyset}}$	0.77%
u_{D_b}	0.26%
u_e	3.12%
u_H	0.95%
u_{V_s}	1.00%